IN SITU CHARACTERIZATION OF ELECTROCHEMICAL PROCESSES OF SOLID OXIDE FUEL CELLS

A Dissertation
Presented to
The Academic Faculty

by

Xiaxi Li

In Partial Fulfillment
of the Requirements for the Degree
Doctor of Philosophy in the
School of Materials Science and Engineering

Georgia Institute of Technology
December 2014

IN SITU CHARACTERIZATION OF ELECTROCHEMICAL PROCESSES OF SOLID OXIDE FUEL CELLS

Approved by:

Dr. Meilin Liu, Advisor
School of Materials Science and Engineering
Georgia Institute of Technology

Dr. Brent Carter
School of Materials Science and Engineering
Georgia Institute of Technology

Dr. Lawrence A. Bottomley, Co-advisor
School of Chemistry and Biochemistry
Georgia Institute of Technology

Dr. Phillip First
School of Physics
Georgia Institute of Technology

Dr. Faisal Alamgir
School of Materials Science and Engineering
Georgia Institute of Technology

Dr. Gleb Yushin
School of Materials Science and Engineering
Georgia Institute of Technology

Date Approved: Aug. 18th. 2014

Every man is a valuable member of society who by his observations, researches and experiments procures knowledge for men.

— James Smithson

ACKNOWLEDGEMENTS

Foremost, my deepest gratitude goes to my advisor, Dr. Meilin Liu, a true scientist who ceaselessly pursues to understand the mechanisms of energy conversion and storage. I benefitted tremendously in my past six years working with him, not only for his guidance academically, but also for the example he set for his group members as a researcher who aims to make long-lasting impact in the field. He gave me freedom in choosing the research topics and directions, while providing me critical opinions in my research plans and abundant resources to carry them out, which I appreciate very much.

I am also privileged to be co-advised by Dr. Lawrence Bottomley. He guided me in the subjects of scanning probe microscopy, electrochemistry and surface enhanced Raman spectroscopy, which constitute the foundation of this thesis. I enjoyed many of the thought-provoking discussions with him, and I am very much impressed by his passion and expertise in analytical chemistry. I would also like to give thanks to the rest of my Ph.D thesis committee, Dr. Faisal Alamgir, Dr. Brent Carter, Dr. Phillip First, and Dr. Gleb Yushin for their guidance and suggestions.

Dr. Mingfei Liu and Dr. Dong Ding are both great mentors for me. They guided me in the understanding of the electrochemical processes on the solid oxide fuel cells, and helped me tremendously in the electrode material design and fuel cell testing. Many of the research topics presented in this thesis are founded on the discoveries they made during the fuel cell testing.

Appreciation is due to Dr. Kevin Blinn, Dr. Jun-Pil Lee, and Dongchang Chen in the development of *in situ* Raman spectroscopy and SERS. The mechanism study with these new

techniques would not be successful without their efforts. Dr. Mostafa El-Sayed also kindly helped me in the development of SERS by giving me free access to his lab equipments and collaboration with his group members: Dr. Mahmood and Daniel O'Neal.

I am also in debt to other colleagues that contributed to this work. Samson Lai provided me insight of electrode surface through the synchrotron-based X-ray analysis; Dr. Xiaoyuan Lou guided me to work on the micro-probe impedance spectroscopy; Dr. Matt Lynch and Lei Zhang, both experts in modeling, helped to develop in-depth understanding of oxygen reduction on cathode materials; Dr. Wentao Qin trained me in TEM cross-section sample preparation; Dr. Dongbo Zhang and Dr. Yingcui Fang helped me in sputtering deposition of thin films; Hyungmin Park introduced me to the block-copolymer patterning technique; Kelsey Beaver (Bottomley group) instructed me on the operation of scanning probe systems; Liyi Li (C.P Wong group) worked with me to develop patterned electrodes through photo-lithography.

In my professional development, I received valuable advices from Dr. Zhe Cheng, Dr. Min-Kyu Song, Dr. Wei Lin (C.P Wong group), Dr. Fei Peng (Speyer group), and Dr. Bin Kang (El-Sayed group). Their insightful suggestions helped me to establish a correct mindset and find efficient routes to accomplish my Ph.D. study.

Memory goes to Dr. Lei Yang, a former Liu group member who unfortunately passed away in 2012. He laid a sound foundation in the study of barium containing catalysts and inspired many of my present works.

This work was supported in part by the HeteroFoaM Center, an Energy Frontier Research Center funded by the U.S. Department of Energy Office of Basic Energy Sciences, under Award Number DE-SC00001061.

TABLE OF CONTENTS

Page

LIST OF TABLES

Page

LIST OF FIGURES

Page

LIST OF ABBREVIATIONS

AFM	Atomic force microscopy
BCP	Block copolymer patterning
BZCYYb	$BaZr_{0.1}Ce_{0.7}Y_{0.1}Yb_{0.1}O_{3-d}$
BZY	$BaZr_{1-x}Y_xO_{3-d}$
EIS	Electrochemical impedance spectroscopy
EF	Enhancement factor of SERS
EFM	Electrostatic force microscopy
GDC	$Ce_{1-x}Gd_xO_{2-\delta}$ (Gadolinium doped ceria)
OCV	Open circuit voltage
ORR	Oxygen reduction reaction
LSCF	$La_{1-x}Sr_xCo_{1-y}Fe_yO_{3-\delta}$
LSM	$La_{1-x}Sr_xMnO_{3-\delta}$
R6G	Rhodamine-6G
SDC	$Ce_{1-x}Sm_xO_{2-\delta}$ (Samarium dope ceria)
SEM	Scanning electron microscopy
SERS	Surface enhanced Raman spectroscopy
SOFC	Solid oxide fuel cell
SSC	$Sm_{1-x}Sr_xCoO_{3-\delta}$
TEM	Transmission electron microscopy
TPB	Triple phase boundary
XAS	X-ray absorption spectroscopy
XPS	X-ray photoemission spectroscopy

XRD	X-ray diffraction
YSZ	$Zr_{1-x}Y_xO_{2-\delta}$ (Yttrium stabilized zirconia)

SUMMARY

Solid oxide fuel cells (SOFCs) represent a next generation energy source with high energy conversion efficiency, low pollutant emission, good flexibility with a wide variety of fuels, and excellent modularity suitable for distributed power generation. As an electrochemical energy conversion device, SOFC's performance and reliability depend sensitively on the catalytic activity and stability of the electrode materials. To date, however, the development of electrode materials and microstructures is still based largely on trial-and-error methods because of inadequate understanding of the mechanisms of the electrode processes. Identifying key descriptors/properties of electrode materials or functional heterogeneous interfaces, especially under *in situ* conditions, may provide guidance to the design of electrode materials and microstructures. This thesis aims to gain insight into the electrochemical and catalytic processes occurring on the electrode surfaces using unique characterization tools with superior sensitivity, high spatial resolution, and excellent surface specificity applicable under *in situ/operando* conditions.

For example, Raman spectroscopy is used for probing and mapping chemical species present on SOFC electrodes under *in situ* conditions. To increase the sensitivity towards species on electrode surfaces, surface enhanced Raman spectroscopy (SERS) technique is employed. To probe SOFC electrode surfaces at high temperatures, thermally robust and chemically inert SERS probes (e.g., Ag nanoparticles coated with SiO_2 shell) are fabricated; they exhibit excellent SERS activity and superior robustness at high temperatures (up to 450°C). Model cells with patterned electrodes are fabricated to create electrodes and electrochemical interfaces of well-defined geometry, facilitating the isolation of surface electrochemical processes under

investigation. Block-copolymer nano patterning technique, in combination with electrostatic force microscopy (EFM), a tool capable of phase identification on nanoscale, is utilized to determine the distribution of contamination species and surface modifiers.

Carbon deposition on nickel-based anodes is investigated with *in situ* Raman spectroscopy and SERS. Analysis shows a rapid nucleation of carbon deposition upon exposure to small amount of propane. Such nucleation process is sensitive to the presence of surface coating (e.g., GDC) and the concentration of steam. In particular, *operando* analysis of the Ni-YSZ boundary indicates special function of the interface for coking initiation and reformation.

The coking-resistant catalysts (BaO, BZY, and BZCYYb) are systematically studied using *in situ* Raman spectroscopy, SERS, and EFM. In particular, time-resolved Raman analysis of the surface functional groups (-OH, -CO_3, and adsorbed carbon) upon exposure to different gas atmospheres provides insight into the mechanisms related to carbon removal. The morphology and distribution of early stage carbon deposition are investigated with EFM, and the impact of BaO surface modification is evaluated.

The surface species formed as a result of sulfur poisoning on nickel-based anode are examined with SERS. To identify the key factors responsible for sulfur tolerance, model cells with welldefined electrode-electrolyte interfaces are systematically studied. The Ni-BZCYYb interface exhibits superior sulfur tolerance.

The oxygen reduction kinetics on LSCF, a typical cathode material of SOFC, is studied using model cells with patterned electrodes. The polarization behaviors of these micro-electrodes, as probed using a micro-probe impedance spectroscopy system, were correlated with the systematically varied geometries of the electrodes to identify the dominant paths for oxygen

reduction under different electrode configurations. Effects of different catalyst modifications are also evaluated to gain insight into the mechanisms that enhance oxygen reduction activity.

The causes of performance degradation of LSCF cathodes over long term operation are investigated using SERS. Spectral features are correlated with the formation of surface contamination upon the exposure to air containing Cr vapor, H_2O, and CO_2. Degradation in cathode performance occurs under normal operating conditions due to the poisoning effect of Cr from the interconnect between cells and the high operating temperature. The surface-modified LSCF cathode resists surface reactions with Cr vapor that impairs electrode performance, suggesting promising ways to mitigate performance degradation.

This thesis applies new characterization methods with high sensitivity, fine spatial resolution, and *in situ* capability to the study of SOFC electrodes. These methods provide key information of the identity, distribution, and evolution of surface species, which is vital to gaining insight into the mechanisms of electrochemical processes. The fundamental understandings obtained in this study will be useful in the design of SOFC electrode materials and structures. In addition, the methodology developed herein is applicable to the study of a wide variety of electrochemical interfaces and high-temperature catalytic systems.

CHAPTER 1: **INTRODUCTION**

Fossil fuels power up the industrial age. Conversion of heat energy released during the combustion of carbon-based fuels into electricity is the main process used in electric power generation. While the energy generated from fossil fuels empowered human society to make achievements unforeseeable before industrialization, a major crisis is looming for the fossil fuel based industry. One aspect of the crisis lies on the accessibility of the fossil fuels, including crude oil, natural gas, and coals. According to International Energy Agency (IEA) and U.S. Energy Information Administration (EIA), although the supply of fossil fuels is expected to be ample for the next 50 years, the cost to extract these resources will keep increasing with the depletion of easy-to-access reserves.[1, 2] Another challenge faced by the fossil fuel economy is the devastating environmental impact. According to the assessment report released by the Intergovernmental Panel on Climate Change (IPCC) in 2013, emission of greenhouse gases induced by human society (mainly CO_2), has significantly influenced the CO_2 concentration in the atmosphere, leading to a series of climate change phenomena referred as "global warming".[3]

The studies of solid oxide fuel cells (SOFCs) are stimulated by these upcoming challenges. Fuel cells convert chemical energy directly into electricity through electrochemical reactions rather than the typical Carnot cycles of the combustion engines. This is a much more efficient and environmental benign technology for energy conversion. Solid oxide fuel cells utilize an ion conducting ceramic membrane, e.g., yttrium stabilized zirconia (YSZ) or scandium doped ceria (SDC), and two ceramic or ceramic-metal electrodes, one exposed to air and the other to fuel to facilitate the electrochemical reactions.[4] SOFCs are operated at elevated temperatures (~800^0C), and do not require noble metals such as Pt to activate the fuel or oxygen

for electrochemical reactions, making this technology economically promising for large scale application.[5] Rather, less expensive materials such as nickel is utilized as the anode material for fuel oxidation, and perovskite materials such as $La_{1-x}Sr_xMnO_{3-\delta}$ (LSM) and $La_{1-x}Sr_xCo_{1-y}Fe_yO_{3-\delta}$ (LSCF) are used as cathode materials for oxygen reduction.

SOFCs can utilize not only pure hydrogen but also a wide variety of carbon-based fuels such as coal gas, [6] methane, [7] propane,[8, 9] methanol [10] and even octane.[11, 12] The fuel flexibility of SOFCs facilitates its immediate inclusion into our electricity generation infrastructure and will be applicable in the future when hydrogen becomes the fuel of choice for zero-emission power generation.[13] The pilot models of SOFCs reported power efficiency of 60%, almost double the figure of the conventional coal fired power plant (~35%),[13] and superior to the state-of-the-art integrated gasification combined cycle (IGCC) plants (~45%).[14] In addition, a sub-MW SOFC stack is capable of power generation at its optimal fuel efficiency, while a conventional heat-based power plant requires at least GW scale to reach reasonable efficiency.[5, 15-17] The high efficiency of small stacks of SOFCs, often referred to as superior modularity, makes this technology an ideal solution for distributed power generation. [18, 19]

1.1. Challenges of the Solid Oxide Fuel Cells

To make SOFC technology more commercially competitive, two technical challenges need to be addressed: lowering operating temperature and enhancing performance stability. State-of-the-art SOFCs are operated at ~800°C. This elevated temperature results in degradation of key components over long term operation. While reducing SOFC operation temperatures to intermediate range (500-750^{0}C) can provide considerable economic advantage on the SOFC

technology,[20] SOFC performance decreases at intermediate temperatures, due to the increase of electrochemical polarization on both anode and cathode and the decrease of ionic conductivity of the electrolyte materials.

Electrode materials of the SOFCs are also susceptible to the formation of undesired phases and species on the surfaces and interfaces, which degrades the performance by blocking the active sites for electrochemical reactions. The nickel-based anode, for example, is vulnerable to carbon deposition when hydrocarbon is used as fuel.[21-24] When fuels containing ppm level of H_2S are fed to the anode, the nickel-based anode also suffers significant performance loss.[25-27] Cathode materials are also susceptible to contaminations and material degradation over the long term operation. For example, using Cr-containing alloys as interconnect material leads to Cr poisoning that degrades cathode performance. [28-30] In addition, cathode materials such as LSCF degrade due to element leaching and surface segregation, and the presence of CO_2 and water vapor in the air could accelerate this process. [31, 32]

Optimization of the electrode materials is imperative to improve the low temperature performance and long term stability of SOFCs. Finding new materials applicable for SOFCs, however, remains a difficult and time-consuming task, due to the multifold requirements by electrochemical processes. To be suitable as a cathode, the material must exhibit superior mixed ionic and electronic conductivity, have a thermal expansion coefficient that matches with the electrolyte material, be chemical compatible with both the electrolyte and the interconnect materials, and exhibit phase stability over long term operation. While many cathode materials has been explored and showed promising performance at lowered operation temperature,[33, 34 35] the long term stability is either poor or undocumented. Until now, the most reliable cathode materials are still LSM and LSCF, which have been used as SOFC cathode materials since 1970s.

Similar situations are encountered in the development of novel anode materials. Since nickel is susceptible to degradation due to carbon deposition and sulfur poisoning, Cu, $La_{0.75}Sr_{0.25}Cr_{0.5}Mn_{0.5}O_{3-\delta}$, $Sr_2Mg_{1-x}Mn_xMoO_{6-\delta}$ ($0 \leqslant x \leqslant 1$) and (La, Sr)(Ti)$O_3$ were proposed to replace nickel for direct hydrocarbon SOFC.[36-38] However, these alternative anode materials usually have poor chemical compatibility or high thermal expansion mismatch with the YSZ electrolyte, and reduced catalytic activity towards hydrocarbon reforming.

Due to the complexity of the operating environment, traditional trial-and-error methods have been proven unproductive in the discovery of new materials or material combinations for SOFCs. Rational design of SOFC electrode materials could provide critical guidance to the experimental exploration.[39] The key to rational design of SOFC materials is to understand mechanisms of electrode functioning and degradation, and to identify the important factors required for high performance and long-term durability. With this information, the search of novel electrode materials can be narrowed down to the candidates with the desired descriptors/properties.

1.2. Research Objectives

Understanding the mechanisms of electrode processes relies on the characterization of SOFC electrode materials. Conventional characterization of SOFC electrodes involves electrochemical testing methods, such as the electrochemical impedance spectroscopy (EIS) and voltammetry, and postmortem analysis such as scanning electron microscopy (SEM) and X-ray photoemission spectroscopy (XPS).

Due to the complexity of reactions on the SOFC electrode surfaces, conventional characterization tools cannot always identify the factors responsible for electrode functioning

and degradation. For example, the electrochemical testing of full fuel cell or symmetric cell provides the overall performance evaluation of an electrode material, but the function nature of the electrode surface is often entangled with other factors such as microstructure, electrode thickness, ohmic resistance of the electrolyte materials, and the polarization resistances of other interfaces. Therefore, the first step in the mechanistic investigation is to identify characterization methods capable of isolating key factors that influence the electrode performance, revealing the intrinsic reactivity of the electrode surface.

Ex situ characterization tools such as SEM and XPS enable analysis of the microstructure and elemental composition on the electrode surface. However, the morphology and composition of the surface found from postmortem analysis may not be the same as that occurring during fuel cell operation. A key objective of this thesis was to develop characterization methods for *in situ* analysis of SOFC electrode surfaces under conditions approaching operation. Specifically, the following characterization/fabrication methods were used for mechanism understanding of the electrocatalytic interfaces.

- *In situ* probing and mapping of the evolution of surface species and incipient phases on the electrochemical interfaces with Raman spectroscopy.
- Detection of surface species or reaction intermediates present in trace amount using surface enhanced Raman spectroscopy (SERS).
- Nanoscale phase identification across heterogeneous interfaces using electrostatic force microscopy (EFM)
- Fabrication of patterned electrodes with well-defined geometries and interfaces for mechanistic investigation.

By correlating the identity, distribution, and evolution of the surface species with the electrochemical behavior of the electrode materials, critical surface properties related to electrocatalytic reactions and surface degradations can be unraveled. Emphasis is placed on the following subjects:

- Early stage carbon deposition on nickel-based SOFC anodes and the factors that influences its initiation
- Ba-containing coking resistant catalysts
- Sulfur poisoning on nickel-based anode and the sulfur tolerant interfaces
- Oxygen reduction pathways on cathode materials and the catalysts that enhances such process
- Material degradation of LSCF cathodes over long term operation

1.3. Structure of the Thesis

This thesis focuses on studying surface processes on the SOFC electrodes utilizing advanced characterization methods, including *in situ* Raman, SERS, and electrostatic force microscopy performed on model cells with patterned electrodes, to gain insight into the material properties critical to cell performance and long term stability.

Chapter 2 provides the background of this thesis: electrochemical reactions on the surface of SOFC electrodes, including the interaction between gas species, surface catalyst materials, electrodes and electrical biases. Fundamentals of Raman spectroscopy, surface enhanced Raman scattering (SERS), and scanning probe techniques are also presented in this chapter to introduce their strengths for mechanism study.

Chapter 3 details the technical approaches for the mechanism study of SOFC electrodes. In particular, the chapter introduces the optimization of Ag nano probes for optimal SERS effect, the design of Ag nanoparticles coated with SiO_2 shell for thermally robust SERS, the capability of electrostatic force microscopy to distinguish different surface phases, and the fabrication of patterned electrodes and surface catalysts.

Chapter 4 presents the study of early stage carbon deposition on nickel-based SOFC anodes. *Ex situ* and *in situ* SERS are utilized to detect carbon deposition in trace amount, revealing the influence of propane exposure, gas composition, and surface coatings on the initiation of coking. *Operando* SERS analysis in combination with the patterned electrodes is utilized to map the distribution of surface species across the anode triple phase boundaries.

In Chapter 5, the mechanisms for coking tolerance of Ba-containing catalysts are investigated, including BaO, BZY, and BZCYYb. The time-resolved analysis under near operating conditions allows for identification of surface species active for the catalytic processes that resist carbon deposition. In addition, Electrostatic force microscopy study reveals the distribution of early stage carbon deposition on the nickel surface with and without BaO surface catalyst.

In Chapter 6 model cells with patterned electrodes are used to gain insight into the key factors influencing sulfur poisoning. By changing the electrolyte materials of the patterned electrodes, sulfur tolerances are correlated to the nature of triple phase boundary. The adsorption of sulfur on nickel surface is also studied using SERS analysis.

Chapter 7 focuses on the ORR processes of LSCF cathode. Model cells with micro patterned electrodes, in combination with a micro-probe EIS station, are used to identify the

dominant oxygen reduction paths. Effects of different modification catalysts are evaluated, and the factors responsible for ORR enhancement are discussed.

In Chapter 8, the operation conditions related to the material degradation of LSCF electrodes are studied with SERS. Contamination species and element segregation are identified after long term operation. The spatial distribution of degradation-related species provides detailed information of cathode deactivation and the approaches that minimize such process.

Chapter 9 summarizes the mechanisms unraveled with the unique surface characterization tools. In addition, limitation and challenges of these characterization methods are discussed. Further, recommendations are made for development of *in situ* characterization of SOFC electrodes.

CHAPTER 2: **BACKGROUND**

2.1. Probing Surface Electrocatalytic Reactions

The performance and stability of the SOFC electrodes are determined by the surface electrocatalytic reactions. To facilitate the energy transformation processes and avoid reactions that cause electrode degradation, it is critical to understand their sequence, pathways and rate limiting steps. Figure 1 illustrates the main components of an SOFC and the key reaction sequences for oxygen reduction reaction on the cathode side and the transformation of hydrocarbon fuels on the nickel-based anode. Phenomenologically, cathodic interfacial polarization involves the reduction of an oxygen molecule to the oxygen anion (O_2^-) and its incorporation into the electrolyte (an oxygen ion conductor). Piecewise, the mechanism requires, in some order, the following processes: adsorption, reduction, dissociation, and incorporation.[40] Detection of the surface intermediates on the SOFC cathode will help identifying the bottleneck in oxygen reduction, and degradation that blocks efficient ORR processes. The utilization of hydrocarbon fuels on the nickel based anode also involves a series of elemental steps. As the hydrocarbon molecules are fed into the anode, they undergo dehydrogenation and C-C bond cleavage,[41, 42] which activates the hydrocarbons for energy transformation.

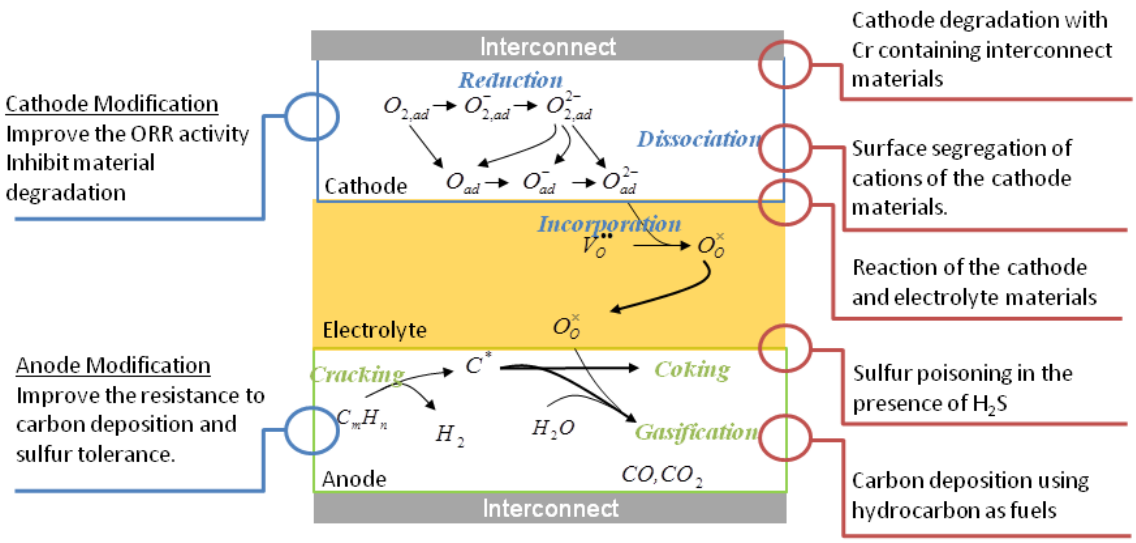

Figure 1: Main components of SOFC and possible reaction sequences on electrodes.
Call-outs illustrate the effective electrode modifications and possible degradations of the fuel cell components.

Contamination and change of surface composition may decrease the electrode performance. For example, cathode materials such as LSM and LSCF are susceptible to Cr poisoning when Fe-Cr alloys (e.g., Crofer 22 APU) were used as interconnect. In addition, the cathode materials themselves may degrade over long term operation, due to the segregation of metal oxides such as SrO from the perovskite lattice. On nickel-based anode, accompanying the hydrocarbon activation, monoatomic carbon deposits on the nickel surface. The surface carbon atoms diffuse across the surface to annex with each other, forming clusters, encapsulation, wiskers, and filaments that reduce the active electrode area and breakdown of anode structure.[43] Nickel is also susceptible to sulfur poisoning when H_2S containing gases are used as fuel. A few ppm of H_2S can drastically decrease cell performance instantaneously and lead to non-recoverable performance degradation if exposure prolongs. [44-47]

Surface modification can significantly improve the performance and stability of the electrodes. Decorating an $La_{1-x}Sr_xCo_{1-y}Fe_yO_{3-\delta}$ (LSCF) porous electrode with certain nanoparticles such as $Sm_{1-x}Sr_xCoO_{3-\delta}$ (SSC) and $Ce_{1-x}Sm_xO_{2-\delta}$ (SDC) reduces the polarization resistance[48, 49]; while coating the LSCF surface with $La_{1-x}Sr_xMnO_{3-\delta}$ (LSM) improves the long term stability[50]. The carbon deposition on nickel-based anode can also be alleviated through modifications such as BaO, BZCYYb or BZY, catalysts that facilitate the gasification of deposited carbon atoms. [6, 12, 51, 52]

The surface of electrode represents a complicated system where different factors influence the electrochemical behaviors simultaneously. Figure 2 illustrates the main factors that influence the electrode activity and stability. Foremost, the electrode performance is determined by the bulk property of the materials, such as the crystal structure, stoichiometry and concentration of charge carriers (bulk property). Second overpotential that develops on the electrode surface and interfaces results in variation of composition on the material surface (polarization). Third, the activity of the electrode material to catalyze certain reactions depends on the composition of the gas atmospheres and the presence of surface modifications (heterogeneous catalysis). In addition, the accessibility to the reactants and product dissipation paths render different catalytic activity and selectivity to different regions (electrochemical interfaces). To understand the overall mechanisms of electrochemical reactions and the material degradation of the electrode, it is necessary to take account of the influence of all these factors, and to identify the important ones. Probing and mapping of surface species *in situ* is the key to obtain such knowledge.

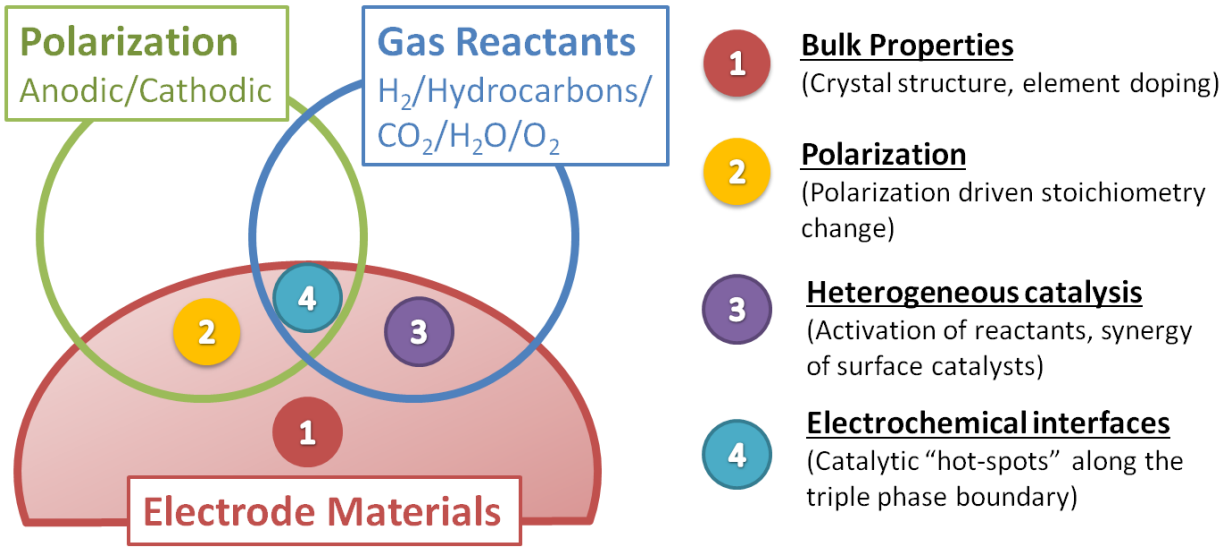

Figure 2: Factors influncing the electrochemical performances and material degradation processes.

2.1.1. Bulk Properties

The electrical property of the electrode materials are governed by the concentration of charge carriers (e.g., oxygen vacancies, protons, electron, and electron holes) and their diffusivity, which are determined by the crystal structure, concentration of doping elements and the stoichiometry of the materials. Developing materials with desired electrical properties has been the focal point of most studies of SOFC electrodes.

A typical example is the development of mixed ionic and electronic conductor for the SOFC cathode. Starting with a perovskite structure (e.g., $LaMnO_{3-d}$ or $LaCoO_{3-d}$), different doping elements were introduced to substitute the host elements in cation sites (A/B sites). Doping elements of lower valence state (e.g., Sr or Ca into the A site) can introduce imbalanced charge neutrality, resulting in increase of positive charge carriers such as oxygen vacancies or electron holes. The substitution by elements of the same valence states (e.g., Fe into the B site) has been studied to enhance the activity of material to catalyze oxygen reduction.

The crystal structure and defect chemistry of the electrode materials has been studied using X-ray diffraction and neutron diffraction. The electronic structure of the materials, which is related to the catalytic activity of the electrode, can be examined with XPS, XAS and DFT simulation. While the crystallography information of the bulk material forms a basis for the study of electrode material, it does not fully explain the catalytic processes and material degradation occurring mainly on the electrode surface.

2.1.2. Polarization

The polarization of the electrochemical interface during the long term operation results in changes of material composition on the electrode surface. Electrochemical polarization imposes two effects on electrode materials: the electrical potential built in the electrode material results in diffusion of cations, leading to change of stoichiometry of the electrode surface; the polarized electrode develops equivalent partial pressure of oxygen (or hydrogen) different from its environment, leading to material decomposition.

Cathode materials of perovskite structure often develop stoichiometry change on the surface under the influence of polarization. When LSM cathode is operated with current output, meaning the electrode is polarized with a cathodic overpotential, the electrode performance improves gradually. Such polarization activation behavior is accounted for by the redoping of surface enriched Sr into the lattice. [53, 54] In contrast, LSCF shows performance loss during the long term testing with current output, which is explained by the Sr surface segregation driven by cathodic polarization.[55] While the crystal structure of bulk materials remained intact under

electrochemical polarization, the surface components changes, resulting in loss in electrochemical performances.

2.1.3. Heterogeneous Catalysis

The electrode materials is responsible for the activation of gas molecules for the electrochemical reactions. The capability of the electrode materials to dissociate/adsorb gas molecules is critically related to the electrode performance. For instance, when hydrocarbon fuels such as methane and propane were fed to the SOFC anode, nickel is the key catalyst to break the first C-H bond, and thus activate the hydrocarbon to reform and eventually convert into H_2O and CO_2 and release electrical energy. [42]

More importantly, when the surface catalysts are made up of multiple phases, they can each catalyze different elemental steps and accomplish the conversion process synergetically. This concept helped to develop coking-resistant anode. Ni anode alone is susceptible to coking degradation, a process the carbon deposit on the Ni surface and degrades the performance of the anode. When Ni was modified with BZCYYb, BZY or BaO, however, such degradation could be largely alleviated. [6, 12, 52] It is hypothesized that these surface species adsorbed water, forming –OH moities that react with monotonic carbon radicals to prevent coking.

2.1.4. Electrochemical Interfaces

The charge transfer processes are essential steps to convert chemical energy into electricity. To make possible of such processes, the media carrying the reactants, products and electrons (or electron holes) must be present in adjacency to each other. The regions satisfying such requirement are the “hot-spots” of charge transfer processes. The triple phase boundary

where ionic conducting phase, electronic conducting phase and gas atmosphere converge is a typical reaction hotspot. [56]

The relative location to the electrochemical interfaces influences the local catalytic activity. For example, the triple phase boundaries in a Ni-YSZ anode are the regions where reforming of hydrocarbon fuels is most facile, and least susceptible to carbon deposition under current output. While the hydrocarbon fuels initiate carbon deposition on the nickel electrode surfaces the oxygen ions from the lattice of electrolyte readily spread to the anode surfaces and oxidize the deposited carbon. [57]

2.2. Raman Scattering and Spectroscopy

The energy of a molecule can be separated into three additive parts: motion of electrons, vibration of the atoms and rotation of the molecules. [58]

$$E_{total} = E_{el} + E_{vib} + E_{rot}$$

These three parts of the molecular energy are quantized into different energy levels. As schematically shown in Figure 3, the energy gaps of electronic excitation are much larger than those of molecular vibration, which are in turn larger than those of the molecular rotation.

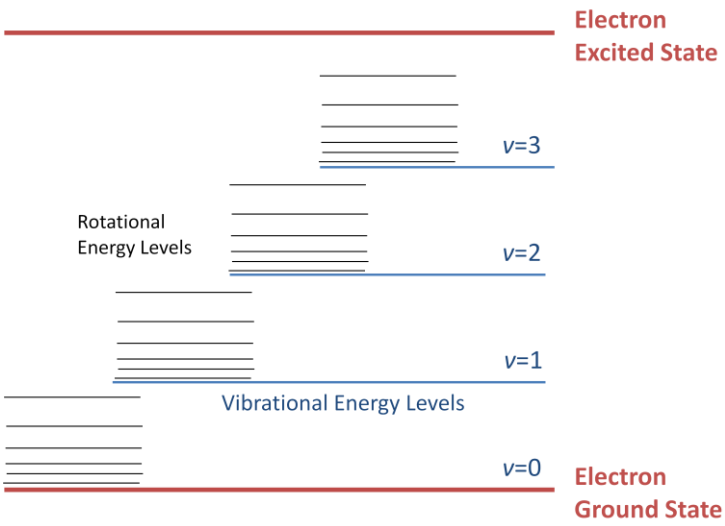

Figure 3: Schematic of the energy levels of a diatomic molecule.
Recreated from a schematic presented in ref[58].

Raman spectroscopy detects the vibration modes of the molecules, as shown in Figure 4. The Raman scattering is an inelastic scattering process when the incident photon, usually by a single wavelength laser, interact with the molecules and lose/gain energy. The scattering process in which the scattered photo loses energy is named Stokes mode, while the one in which the scattered photon gains energy is named Anti-Stokes mode. The energy gained or lost during the Raman scattering process is characteristic of the energy gaps between vibration states. In a Raman spectrometer, the elastic scattered photons (Rayleigh line) are blocked by edge filter designed specifically for different excitation lasers. The Raman scattered photons of different wavelength are selected by positioning a diffraction grating at different angles, directing the photons to the CCD camera to register its intensity. . A Raman spectrum was generated by plotting the intensities of scattered light as a function of the change of photon energy, represented by a shift of frequency (ν), according to

$$\Delta E = hc\Delta\nu$$

in which

$$\nu = \frac{1}{\lambda}$$

where h is the plank constant and c is the speed of light, ν is the wavenumber of the light represented with a unit of cm^{-1}. The wavelength of the scattered light of a specific Raman mode (λ_{sc}) depends on the wavelength of the incident laser (λ_{inc}), however, the shift of wavenumber ($\Delta\lambda$) does not.

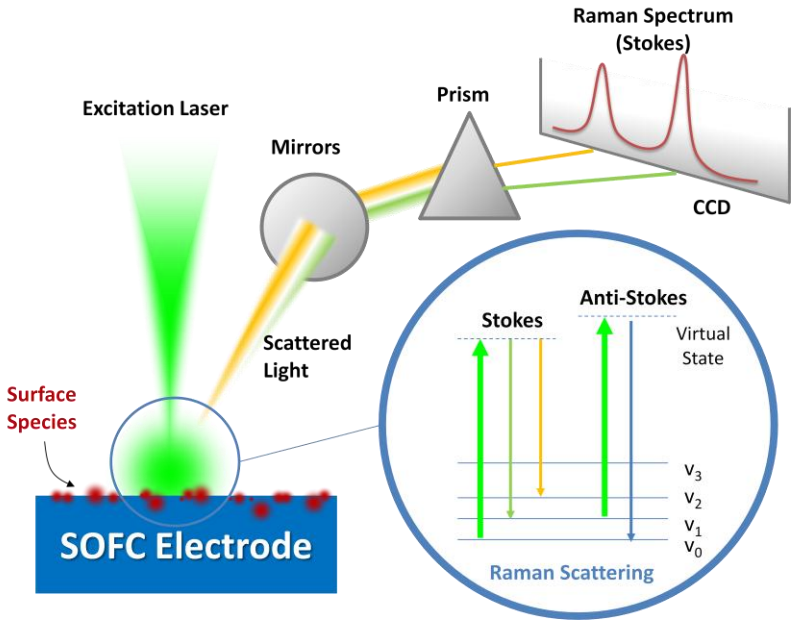

Figure 4: Schematic of using Raman spectroscopy to study the surface of SOFC electrodes.

Raman spectroscopy can be used to detect both bulk phases and surface species through fingerprinting the vibration modes, which is governed by the bonding between the atoms. The vibration modes of the crystal lattice are determined by the space group a material belongs to; they are influenced by the elements of the host lattice and the presence of lattice defects. For example, CeO_2, which has a space group of $Fm\bar{3}m$, shows one Raman active phonon of F_{2g}

symmetry at 465cm^{-1}.[59] Since the energy gap between the vibration levels are determined by the mass of the atoms and the bond strength, the peak position and intensity of the Raman band changes when the cations or anions are replaced by other elements.[59] When cations with valence state of +3 (e.g., Sm, La, Pr, etc.) were introduced to the CeO_2 lattice, a peak between 500 cm^{-1} and 600 cm^{-1} usually increases. The change in intensity was attributed to the presence of oxygen vacancies, which reduced the crystal symmetry. [60-63] The same spectral feature also appears when CeO_2 is exposed to the reducing atmospheres.[64] Therefore, Raman spectroscopy can be utilized to evaluate changes in lattice symmetry as a result of doping, element segregation, contamination, and redox reactions.

Detection of adsorbed surface species relies on the characteristic vibration modes of the functional group, such as OH^- (~3500 cm^{-1}), CO_3^{2-} (1059 cm^{-1}) and SO_4^{2-} (980 cm^{-1}), rather than the phonon modes in the crystal lattice. The *in situ* Raman detection of surface functional groups has been demonstrated for the oxygen adsorption on CeO_2 surfaces. The peak position distinguished peroxide and superoxide adsorption.[65] *In situ* Raman also detected water adsorption on BaO and BZCYYb surface, which indicated water mediated carbon removal through surface modification.[6, 52]

A unique advantage of Raman spectroscopy lies in its capability of *in situ* study of electrochemical interfaces. Unlike electron-based characterization tools such as XPS and EDX, vibration spectroscopy techniques such as IR and Raman do not require vacuum, making them ideally suited for in-situ study of SOFC electrodes. While *in situ* Raman spectroscopy has not been systematically employed to study the electrode processes, several studies have reported its applicability to identify species related to electrode functioning and degradation , including Cr

poisoning of the cathode materials, [66] the adsorption of oxygen species on CeO_2 surface, [65] and the carbon deposition on nickel-based anodes,[67]

The confocal Raman spectrometer, when combined with a motorized stage, is capable of mapping the distribution of surface species. Previously, we have identified the distribution of surface carbon deposition on a patterned Ni electrode after exposure to CH_4 or C_3H_8 containing fuels at elevated temperatures. [67] As presented in an early study, [67] the carbon preferentially deposited on the nickel surface, while the YSZ surface remained clean. The importance of surface mapping is beyond the identification of surface contaminant distribution. In an electrocatalytic system where the boundary between the electrode and electrolyte and the interface of surface modifier and the bulk material play critical roles, such capability can provide imperative information about the "hot-spots" of catalytic reactions.

2.3. Surface Enhanced Raman Scattering (SERS)

2.3.1. Electromagnetic Enhancement Mechanism

Raman scattering has low cross section (probability) compared to elastic scattering (Rayleigh) and characteristic adsorption (IR), resulting in low yield of Raman signal. The low intensity issue is particularly severe in the study of solid oxide fuel cell related materials. While Raman is capable of identifying adsorbed species, many key reactions intermediates on the SOFC electrodes cannot be detected by normal Raman. The surface species that play critical roles in the electrocatalytic processes may have short lifetimes and elusive under normal Raman. For instance, sulfur contamination cannot be detected at high temperature.[45, 68] While carbon-carbon bond has high Raman activity and is relatively easy to detect, the Raman signal is not always available especially during the initial stage of carbon deposition.[69] Although the oxygen

adsorption on reduced CeO_2 can be detected through special heat treatment, oxygen species on other materials such as LSM are not observable, because the equilibrium concentration of adsorption/desorption is below the detection limit.[65]

Some electrode materials exhibit weak Raman modes. For instance, the cubic perovskite structure has no active Raman signal due to its central symmetry. The widely used LSM and LSCF electrodes have perovskite structures with slight orthorhombic or rhombohedral distortion, generating only weak Raman modes. The high temperature *in situ* analysis itself poses challenge to the detection sensitivity, since all Raman modes are weakened at high temperature due to the broadening of vibration bands.

Surface enhanced Raman spectroscopy (SERS), a technique that amplifies the yield of Raman signal, could provide higher sensitivity of the surface species on the SOFC electrodes. First discovered on molecules adsorbed on electrochemically roughened silver substrates,[70, 71] SERS effect amplifies the Raman signal of the adsorbed molecules by a factor of 10^4-10^6. Such enhancement was also observed on Au, Ag or Cu nanoparticles with a variety of geometries.[72-74] SERS enhancement is attributed to the coupling between the excitation laser and the localized surface plasmon (LSP) of Ag or Au nanoparticles, in which the electron clouds of metal particles oscillate with the excitation laser.[75, 76]

Kerker derived the contribution of LSPR to the SERS effect through Mie solution to Maxwell equation.[77] As illustrated in Figure 5, when incident laser resonates with the local surface plasmons, the strength of the electromagnetic field in the vicinity of a Ag nanoparticle is greatly enhanced. The molecule in the vicinity of the Ag nanoparticle experiences the enhanced EM field, and is polarized to a greater magnitude. Due to the inelastic energy transfer, the

molecule polarization has frequencies different from the incident laser. Before the molecular polarization field generates the scattered light, it again resonates with the LSP of Ag nanoparticles, and the effective dipole moment is enhanced. The observed Raman scattering signal, in the presence of Ag nanoparticles, results from two rounds of enhancement. The overall enhancement factor (EF) can be represented by: [78]

$$EF = 5|1 + 2g_0 + 2g + 4gg_0|^2 \approx 20g^2 g_0^2$$

In which, $g_0 = \frac{\varepsilon(\omega_0) - 1}{\varepsilon(\omega_0) + 2}$ denotes the enhancement of incident EM field, and $g = \frac{\varepsilon(\omega') - 1}{\varepsilon(\omega') + 2}$ represents the enhancement of the Raman scattered light. ω_0 is the angular wavenumber of the incident laser (ω=2$\pi\nu$), and ω' represents the angular wavenumber of the scattered light.

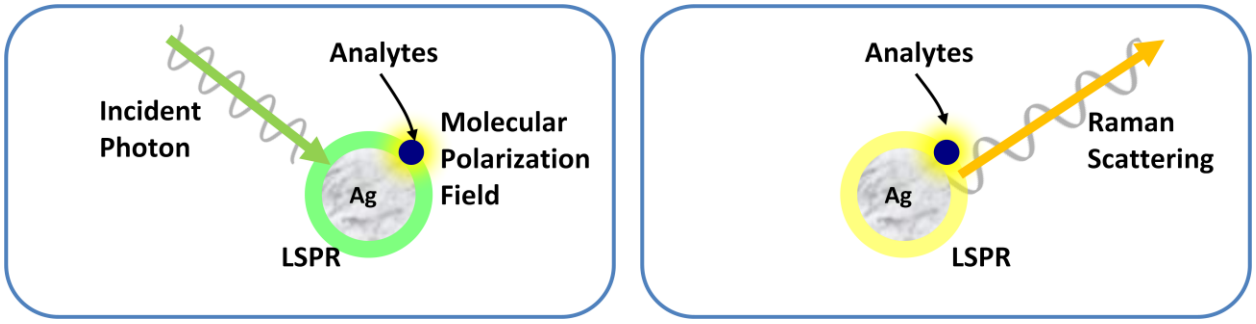

Figure 5: Schematics illustrating the electromagnetic mechanism of SERS.
(A) Resonance between the incident laser (frequency ω_0) and the LSP of Ag nanoparticle, yielding a much stronger EM field to polarize the adjacent molecule. (B) The molecular polarization (frequency ω') resonates with the LSP of Ag, and resulting in enhancement to the Raman scattered light.

Studies validated the double enhancement process and found that the incident laser slightly blue-shifted from the LSPR peak provides the optimal Raman yield,[79] because the LSP with such frequency can effectively resonate with both the incident laser and the Raman scattered light, yielding maximum enhancement. The fundamental of SERS is out of the scope of

this thesis, a detailed derivation of electromagnetic mechanism is presented by Kerker et al.[77] Comprehensive accounts of the LSPR effect and its impact on SERS are provided by different research groups. [78, 80, 81]

2.3.2. Fabrication of SERS Probes

While SERS has been used in many biomedical applications, it has not been used to study ceramic-based electrocatalytic systems. In most SERS applications, the molecules of interest adsorb on the SERS activated substrates, such as roughened Au or Ag substrates or deposited films. To examine the surface species built on the electrode surface, Ag or Au nanoparticles must be introduced to the surface. This approach has been systematically explored by Tian et al. [82] Two approaches are available: to load the Ag or Au nanoparticles on the electrode surfaces (external probe) or to coat the Ag or Au nanoparticles with materials of interest (embedded probe), as illustrated in Figure 6. The external probes can be used to study a wide variety of substrates and surface species. Its applications in graphene and carbon nanotubes are similar in concept to SOFC electrodes.[83-85] The embedded probe architecture that requires coating of materials of interest onto the Au or Ag nanoparticles is especially suitable for the study of surface adsorption onto non-SERS active materials, such as Pt or Pd, [82] while its application to SOFC requires developing protocols to coat electrode materials onto the SERS patterns.

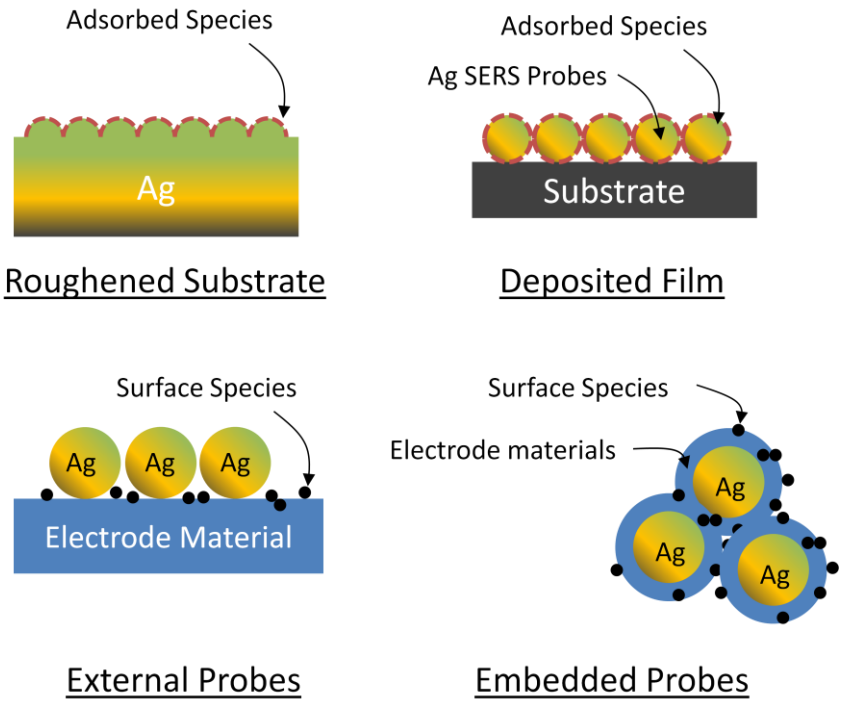

Figure 6: Strategies for fabricating SERS probes.
Roughened substrate and deposited films are suitable for the study of adsorbing molecules. "Borrowed" SERS, including external probes and embedded probes, are suitable for the study of general electrode materials.

Different routes were explored to apply SERS on SOFC materials; each has its own advantages and disadvantages. To detect surface species *ex situ*, the SERS agent must be free of contamination. If not, the spectrum may contain peaks due to contamination, which may obscure peaks from species of. Three ways to introduce SERS agent on SOFC electrodes materials were examined *ex situ*: sputter deposition, colloidal dispersion and chemical vapor deposition. [86] Among them, the sputter deposition was found most reliable, since the geometry and distribution of Ag nanoparticles can be precisely controlled by tuning the deposition conditions. [87]

A potential impediment to the application of SERS to *in situ* characterization of electrode surfaces is the thermal stability of the Au, Ag or Cu nanoparticles. Bare metal nanoparticlestend to ripen and lose SERS activity at high temperatures employed in SOFCs.[88] To make *in situ*

SERS possible, robust Au or Ag nanoparticles must be employed. Recently, van Duyne group found that nanoscale Ag particle with a thin layer of Al_2O_3 retain their shapes and localized surface plamons after annealing at high temperatures.[78, 89] The "shell-isolated nanoparticle enhanced Raman spectroscopy" (SHINERS) technique developed by Tian et al. utilized Ag and Au nanoparticles with a few nanometers of Al_2O_3 or SiO_2 coating that provide enhancement of Raman signal of the underlying materials without interfering with the original surface properties.[90] In this study, Ag nanoparticles coated with SiO_2 shell were used for the *in situ* SERS analysis of SOFC electrode materials at near operating conditions.

2.3.3. Enhancement Factor

Enhancement factor (EF) is a critical parameter to evaluate the SERS probes/substrates. The enhancement factor relates the observed signal intensity in the presence of SERS probes to the intensity observed in normal Raman, i.e, in the absence of Au or Ag nanoparticles. The enhancement factor depends on many factors, e.g., the property of the probed molecules, the population density of the SERS probes, the excitation wavelength, etc, and therefore lacks consistent definition among literature. In this study, two types of EF are defined as EF_0 and EF_{net}, respectively. EF_0, is defined as the intrinsic enhancement factor of the SERS probes towards molecules bound to the surface of the SERS probes. In this study, EF_0 was obtained with Rhodamine-6G (R6G) as the SERS reporter, which was drop coated onto the substrate after SERS treatment. The calculation method developed by Le Ru[91] and Van Duyne[92] is written as follows:

$$EF_0 = \frac{I_{SERS}}{I_{Bulk}} \times \frac{\sigma_{Bulk}}{\sigma_{SERS}}$$

I_{SERS} is the peak value of the characteristic Raman band of R6G collected from the SERS enabled sample, while I_{bulk} represents the same peak value collected from pure R6G molecules without SERS probes. The signals were normalized by the surface concentrations of R6G molecules in each sample: σ_{bulk} and σ_{SERS}. If the change of effective surface area due to the introduction of Ag particles is neglected, , the value of surface concentration can be readily calculated by the volume of R6G solutions, concentration of the solution and the nominal sample area.

EF_{net} is defined as the actual enhancement of Raman signals of an underlying substrate, such as the GDC thin film or evaporated carbon film. This figure of merit represents the practical enhancement of signal intensity from non-adsorbing species, such as the surface phases develop on SOFC electrodes. EF_{net} can be calculated by taking ratio of the intensities of the characteristic peak of the underlying substrate after SERS treatment to that before SERS treatment, written as

$$EF_{net} = \frac{I_{SERS}}{I_{Blank}}$$

I_{SERS} denotes the peak intensity after loading the SERS probes, while I_{bulk} represents the intensity of the same Raman band collected from the blank substrate.

2.4. Probing Surface Potential with AFM

Mapping and probing of surface species at nanometer scale remains a challenge for the study of SOFC electrode surface. In particular, distinguishing the secondary chemical species and phases from the substrate is critical for the study of electrode functioning and degradation. Atomic force microscopy is commonly used for morphological analysis. One property can be

mapped along with the surface morphology of the electrode surface is the contact potential difference (CPD) between the AFM tip and the sample substrate. When the metal-coated AFM tip (typically Pt) and the surface of a conductive or semiconductive sample, which have different work functions, are brought into proximity while connected through external circuit, a potential difference between the two surfaces , will be established across the gap. As is shown in Figure 7, the tip and a local region on the sample surface form a virtual capacitor, which stores capacitive energy, with the potential across the gap equals to CPD [93]. The CPD is directly related to the work function of the surface and is sensitive to adsorbates on the sample surface. Then, it and can be used as an effective factor to distinguish different surface species. Detailed explanations of the origin of difference in surface potentials are presented elsewhere.[94-96]

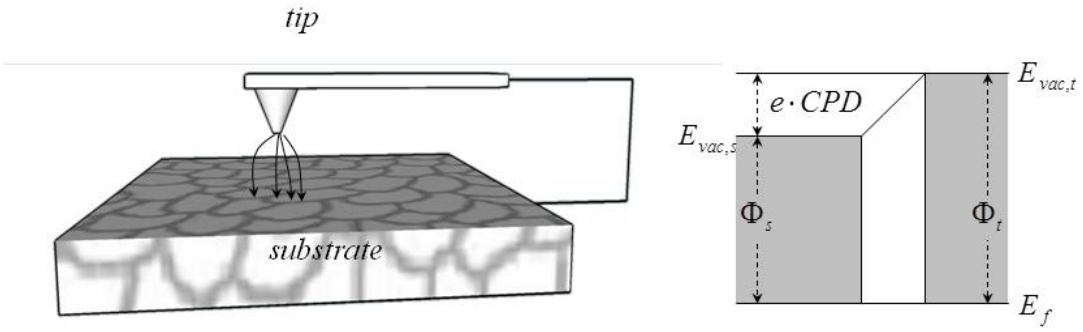

Figure 7: Diagram of the built up of contact potential difference (CPD).
Φ_s is the WF of the sample, Φ_t is the WF of the tip, E_{vac} is the potential of vacuum near the surface of sample or tip.

Non-contact mode imaging is required for the analysis of electrostatic force between the AFM tip and the sample. Compared with the contact forces, the electrostatic interaction is usually very weak and direct sensing the cantilever deflection is ineffective. A common practice is to oscillate the AFM tip, detecting the phase lag between the driving signal and response

signal. Another is to record the amplitude change when the tip is brought near the sample. There are mainly two methods to oscillate the AFM tips that enables detection of electrostatic forces, as listed in Table 1. The first method applies a voltage with a DC component and an AC component between the AFM tip and the sample. The DC component adjusts the contact potential difference between the tip and substrate, while the AC component vibrates the tip to detect the capacitive force between the tip and substrate. The second method does not use the AC signal to detect the electrostatic interaction. Instead, the tip is dithered at its natural vibration frequency. Due to the tip-substrate interaction, the vibration frequency of the AFM cantilever changes. Since the driving frequency keeps the same, the system senses the external force gradient. This will result in a decrease in amplitude or a change in the phase lag, either of which can be detected by the AFM instrument.

Table 1: AFM detection modes for probing surface potentials

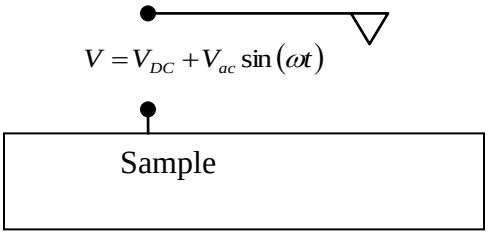	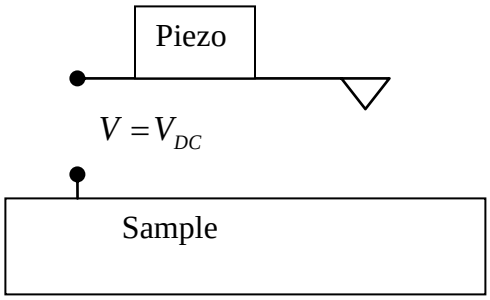
Oscillation: Driven by AC potential, frequency independent of tip resonance	**Oscillation:** Driven by piezoelectric component, working near the resonance frequency of the tip
Detection (ref): Force amplitude $F_{1\omega}$ [96]	**Detection (ref):** Amplitude Change ΔA [97] Phase Shift $\Delta\phi$ [97] Frequency Shift Δf [98, 99]

CHAPTER 3: **TECHNICAL APPROACH**

3.1. Raman Spectroscopy

Raman spectra were obtained using a Renishaw RM 1000 spectromicroscopy system (~2 μm spot size). An air-cooled Ar laser (CVI Melles Griot) emitted at 488 nm and 514 nm and a solid state diode laser (Thorlabs) with 633nm emission line were used for excitation of Raman signal with a total power of 30mW, 5mW, and 10mW, respectively. Appropriate clean-up filters and edge filters (Renishaw and Samrock) were installed for different excitation wavelengths. A Prior motorized stage with 1um spatial resolution was used to inspect different regions of samples. The motion of the stage was programmed in the control interface of the Raman spectrometer (WIRE 2.0), allowing for line scanning and mapping.

For *in situ* Raman analysis, a customized Harrick environmental chamber (Figure 8) was used to control the temperature, gas atmosphere, and apply electrical biases on model fuel cells with patterned electrodes. A quartz window sealed with BUNA O-ring allows the passage of excitation laser and Raman scattered photons. Lens with focal lengths >8mm were used to allow sufficient distance between the lens and the sample surface. The stainless steel jacket of the chamber was cooled with running water.

The surface temperature of the electrode deviates from the nominal temperature of the environmental chamber. To correct this systematic error, the surface temperature was measured with a thermo-couple pressed into contact with the samplemounted on the hot zone of the chamber. All temperatures reported in this work reflect surface temperatures.

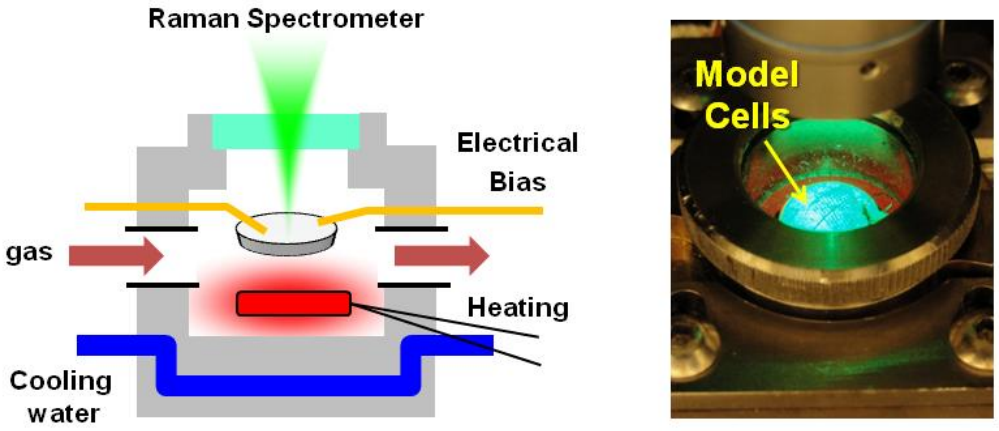

Figure 8: Schematic and picture of the environmental chamber used for *in situ* Raman spectroscopy.

3.2. Sputtered Ag for *ex situ* SERS Analysis

Loading Ag nanoparticles with appropriate geometry and spatial distribution onto the SOFC electrode surface is key to the SERS analysis. Three methods of Ag nanoparticle deposition has been explored by the Liu group: co-deposition of silver with the material of interest by chemical vapor deposition, spray coating solutions of metal colloids, and sputtering deposition of silver[86]. The co-deposition method cannot be used to study a real SOFC electrode, because the silver is introduced in the fabrication stage and may disturb the electrochemical reaction of the electrode materials. Introduction by spray coating metal particle colloids is also unsatisfactory as the stabilizing agents in the colloids generate artifacts in the Raman spectra. The physical vapor deposition method (sputtering or evaporation) is the optimal choice since it provides the least disturbance to the surface of the electrodes.

In this study, magnetron sputtering of Ag was used to deposit SERS probe particles for *ex situ* examination of SOFC electrode materials. Sputtering duration and working pressure were systematically varied and their effect on the morphology and localized surface plasmon

resonance of the Ag nanoprobes was determined. Figure 9 shows that the enhancement factor is tunable by adjustment of the sputtering duration. Optimal sputtering durations were found to be 180 s and 240 s, respectively, for excitation wavelength of 514 nm and 633 nm. The details of parameter optimization are provided elsewhere. [100]

Rhodamine-6G (R6G), a commonly used SERS reporter, was employed to compare the SERS enhancement of the silver nanoprobes created in this study with the values reported in literature. Equal amounts of R6G solution (10 μL) were loaded into areas on the silicon substrates with areas (0.3 cm^2) determined by BUNA O-rings clamped on with a metal washer and a pair of binder clips. Raman spectra were collected after the evaporation of all the liquids; nominal surface concentration were calculated by dividing the total loading amount by the loading area. As shown in Figure 10, the characteristic Raman peaks of $7x10^{-12}$ Mol/cm^2 R6G loaded on the SERS substrate can be distinctively observed; while for the blank substrate, despite the nominal surface concentration being three orders of magnitude higher ($7x10^{-9}$ Mol/cm^2), the R6G peaks are barely distinguishable.

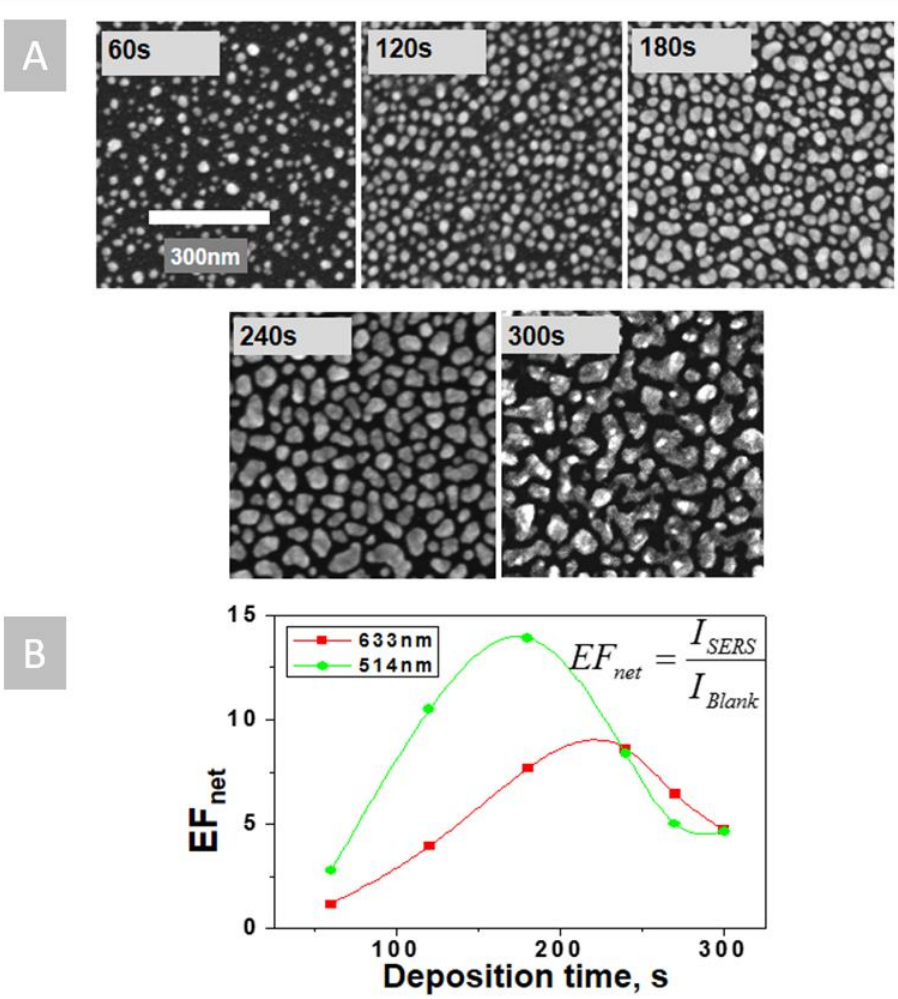

Figure 9: Optimization of net enhancement factors (EF_{net}) of sputtered Ag.
(A) SEM images of sputtered Ag nanoparticles with systematically varied duration under working pressure of $2.5x10^{-2}$ mBar and (B) their corresponding enhancement factors evaluated with a standard carbon films with lasers emitted at 514nm and 633nm. Carbon films were fabricated by evaporation of a 5mm long carbon cord with a Quorum coater.

The intrinsic enhancement factor, as defined in Section 2.3.3, is calculated by taking the ratio of the intensities of main R6G peaks (1390 cm^{-1}), and then normalized by the surface concentration of R6G molecules. EF_0 of the optimal SERS probe (240s sputtering duration) was reported to be $4x10^5$, matching the figures reported by similar studies.[101] It can be noticed that the EF_0 obtained for R6G molecules is several orders of magnitude higher than the EF_{net} obtained on standard carbon films. It is postulated that the bulk of the carbon films contributed a strong

Raman signal under the ordinary Raman mode and a less significant SERS enhancement since carbon lies underneath Ag nanoparticles.

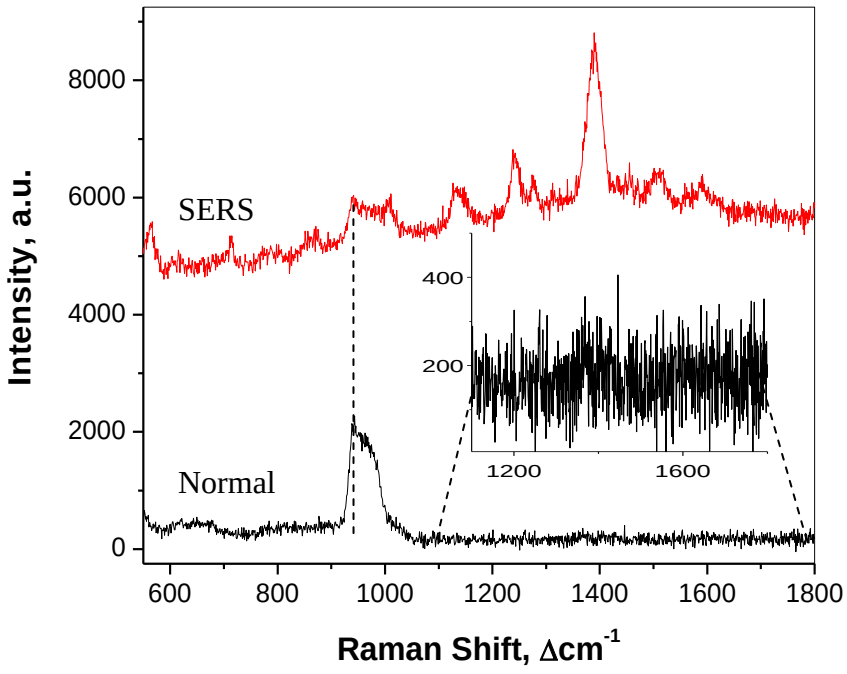

Figure 10: Intrinsic enhancement factor (EF_0) of sputtered Ag nanoprobes.
The Raman spectrum collected from R6G loaded onto SERS substrate (240 s silver loading) with a nominal surface concentration of $7x10^{-12}$ Mol/cm^2 along with the control spectrum obtained from R6G loaded onto blank silicon with nominal surface concentration of $7x10^{-9}$ Mol/cm^2. Inset is a magnification of control spectrum, showing a weak R6G main peak at 1390 cm^{-1}, which is labeled by (*). The broad hump between 900 cm^{-1} and 1000 cm^{-1} is associated with the silicon substrate.

Sputtered Ag nanoparticles showed excellent uniformity across the interface, allowing for semi-quantitative analysis. The quantitation capability of SERS was evaluated by assessing the enhancement factors of sputtered Ag on different locations of the sample. A uniform GDC thin film with thickness of 85 nm was prepared through RF sputtering as the standard. After

annealing the thin film at 800^0C for 1hr, Ag nanoparticles were sputtered on top of it. Figure 11 presents the SERS spectra acquired at different locations, Signal intensities of the F_{2g} mode showed a statistical variance of 3%.

When using the thin film as a standard SERS evaluation, the enhancement factor changes with film thickness, since the chemicals closer to the SERS nanoprobes experience higher plamon field and generates higher Raman yield. Shown in Figure 12 is the intensity of carbon signal collected from the SERS activated carbon films with different thicknesses. The thicknesses gradient was controlled by placing the silicon substrates at different radius from the center of evaporation source. The thicknesses of carbon films were measured by AFM step height profiling after removal of Kaptone tapes that covered part of the sample surfaces. Initially, the SERS intensity of carbon increases with carbon film thickness. generated linear increment of SERS signal. However, as the thickness of carbon film goes over 10nm, linearity of the SERS intensity is lost. Therefore, the SERS signal is dominated by the topmost layer in contact with the SERS nanoprobes.

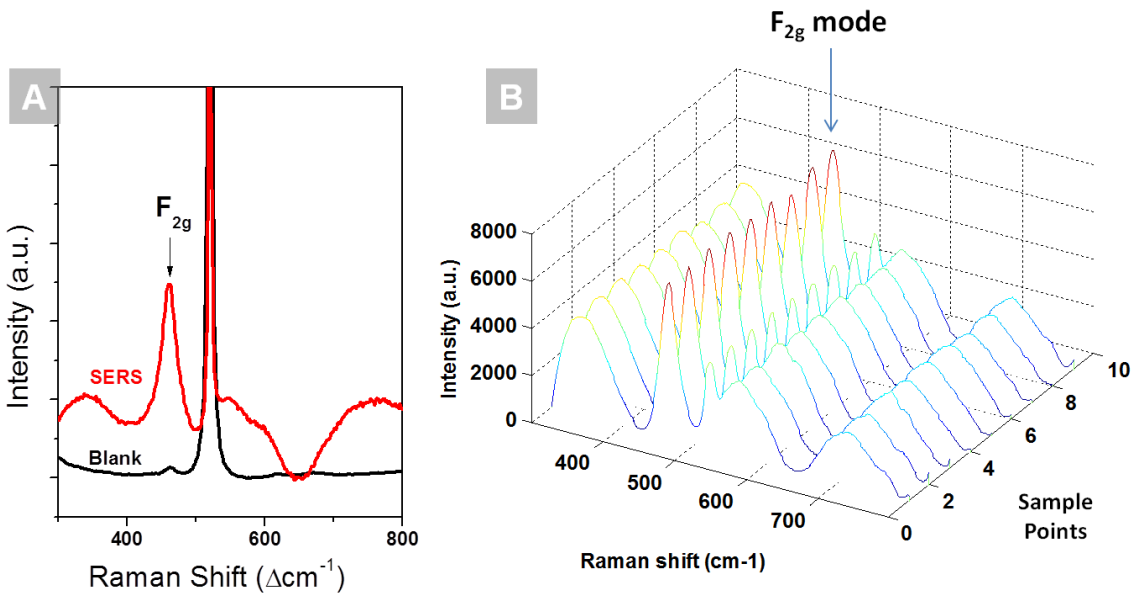

Figure 11: Surface uniformity of sputtered Ag as SERS probes on GDC thin film.
(A) The ordinary Raman SERS spectra of GDC thin film. (B) SERS spectra of the GDC thin film collected from 9 different points.

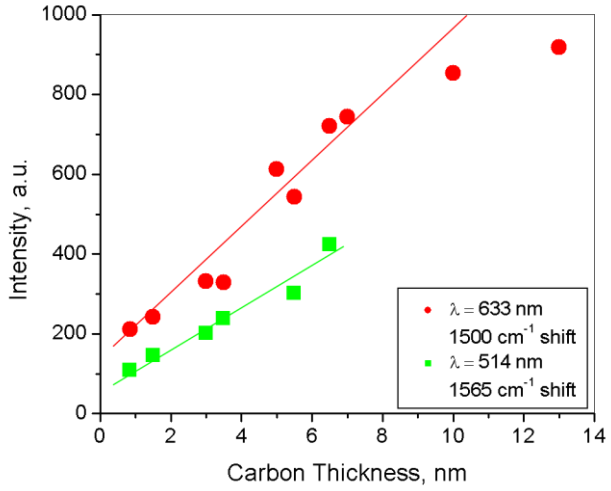

Figure 12: SERS signal of evaporated carbon as a function of film thickness.

The protocol established for *ex situ* SERS analysis of the SOFC electrodes is presented in Figure 13.Under operating conditions, the electrode surface undergoes chemical and physical change. Ag nanoparticles were then sputtered on electrode surfaces to identify the chemical change with SERS.

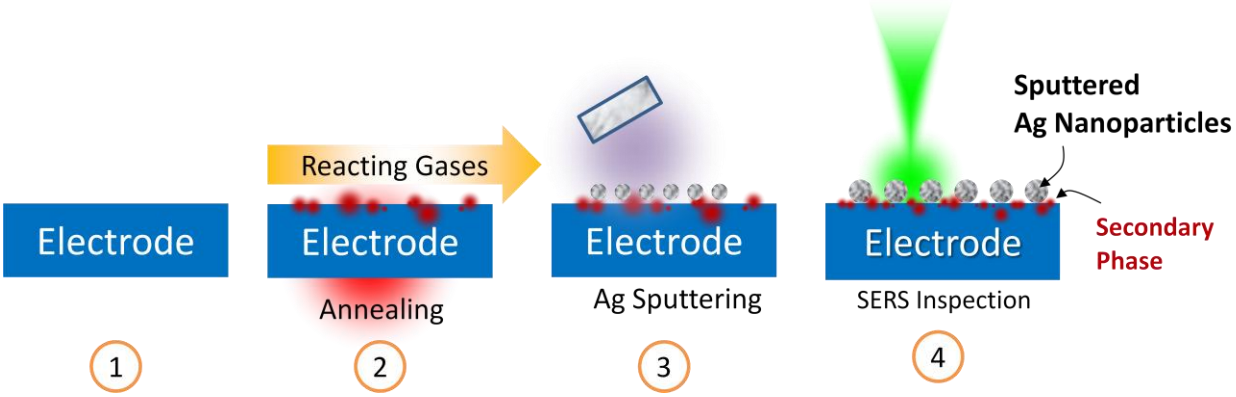

Figure 13: Stepwise schematic of *ex situ* SERS analysis of SOFC electrode materials.

3.3. Ag@SiO_2 Nanoparticles as Thermally Robust SERS Probes

Ag nanoparticles coated with SiO_2 shell are fabricated through a revised polyol method for the *in situ* SERS analysis of SOFC electrode materials. In the seeding process, the $AgNO_3$ is reduced by ethylene glycol to generate Ag nano crystals in a solution-based nucleation-and-growth process. The average diameter of the Ag cores was controlled by adjusting the concentration of $AgNO_3$ solution, the reaction temperature, and the duration of reaction. In general, the average particle diameter goes up with concentration of $AgNO_3$, reaction temperature and duration of reactions, although the detailed function is under investigation.[102, 103] PVP was added to promote a more homogenous size distribution by adjustment of the surface tension between the Ag cores and glycol solution. The fabrication parameters of silver cores and the resulting particle size and standard deviation are presented in Table 2. The average sizes of

the Ag cores and their standard deviations were obtained from the TEM images of 40-60 nanoparticles of all seeding parameters. As displayed in Figure 14, the size distribution of silver cores shows clear distinction under different preparation parameters. In general, the batches of Ag cores with larger diameters have wider size distribution.

Table 2: Fabrication parameters of silver cores of different sizes

Sample CODE	AgNO3:PVP:EG	Reaction Duration	Reaction Temperature	Particle Size (± Stdev)
AgNP-30	0.2g:1.5g:3mL	1 hr	120^0C	18 ± 6 nm
AgNP-40	0.25g:0.75g:3mL	1 hr	120^0C	34 ± 16 nm
AgNP-50	0.25g:0.75g:3mL	2 hr	120^0C	46 ± 19 nm
AgNP-60	0.5g:0.75g:3mL	1 hr	120^0C	82 ± 37 nm
AgNP-80	0.25g:0.75g:3mL	1 hr	150^0C	64 ± 23 nm

Table 3: Fabrication parameters of SiO_2 shells of different thicknesses

Sample CODE	TEOS / Ag Sol	Thickness (± Stdev)
Ag@SiO_2-x1	0.05 mL / 3 mL	6.3 ± 0.7
Ag@SiO_2-x2	0.1 mL / 3 mL	9.8 ± 1.1
Ag@SiO_2-x3	0.2 mL / 3 mL	16.2 ± 1.3
Ag@SiO_2-x4	0.5 mL / 3 mL	29.4 ± 1.7

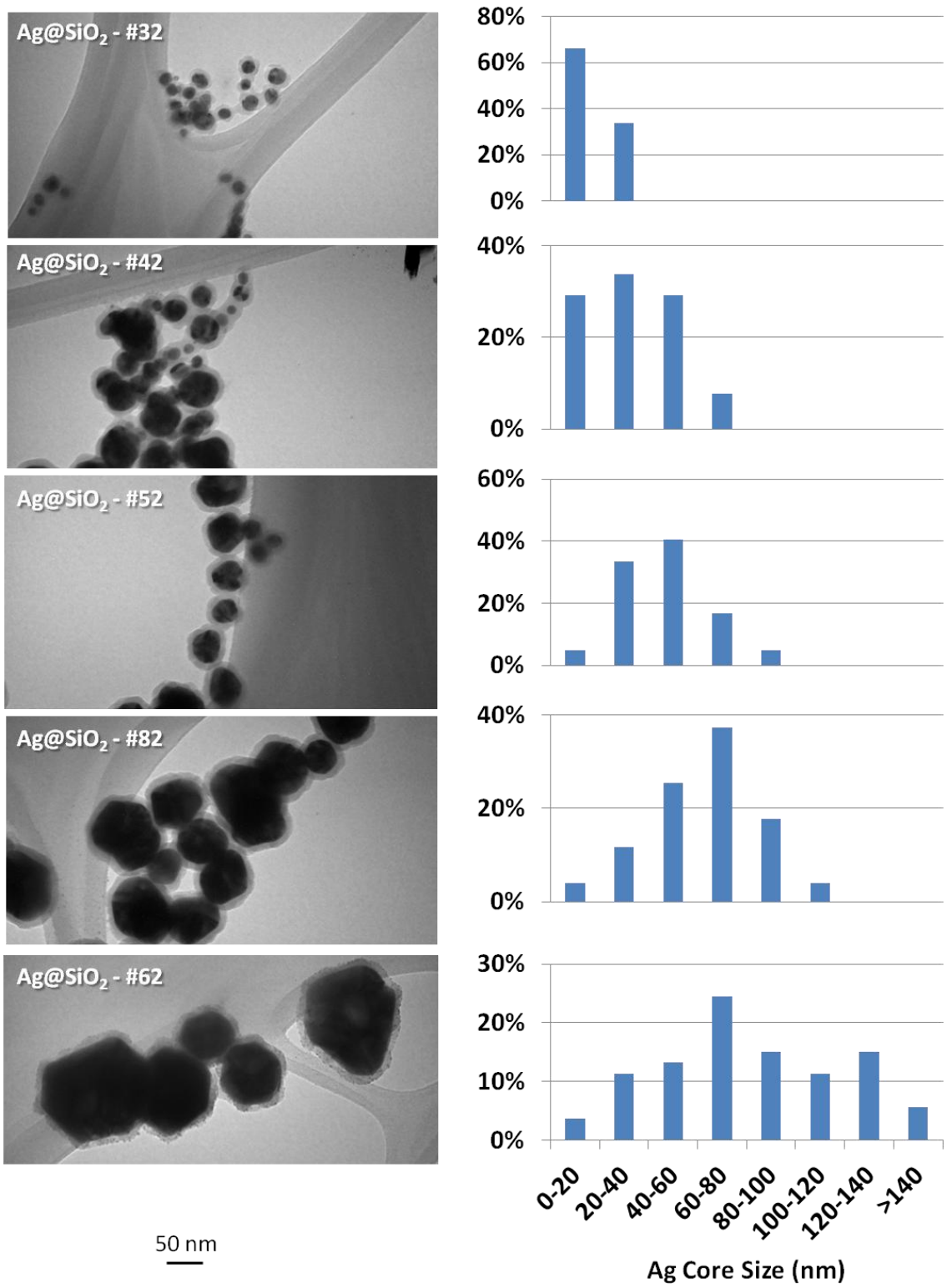

Figure 14: TEM images and size distribution analysis of $Ag@SiO_2$ nanoparticles with Ag cores of different sizes.
Images are of the same scale. Distribution of Ag core sizes obtained from 40-60 particles from 3-5 images.

The thicknesses of SiO_2 coating were controlled by the amounts of tetraethyl orthosilicate (TEOS) solution added to the sol of Ag nanocrystals after the seeding process. Shown in the Table 3 are the processing parameters to develop SiO_2 coating on Ag nano crystals, along with the resulting thickness. The coating was performed on the AgNP-80 nanoparticles, and the TEM images of the samples of each processing parameter were utilized to evaluate the thickness of coating, as shown in Figure 15.

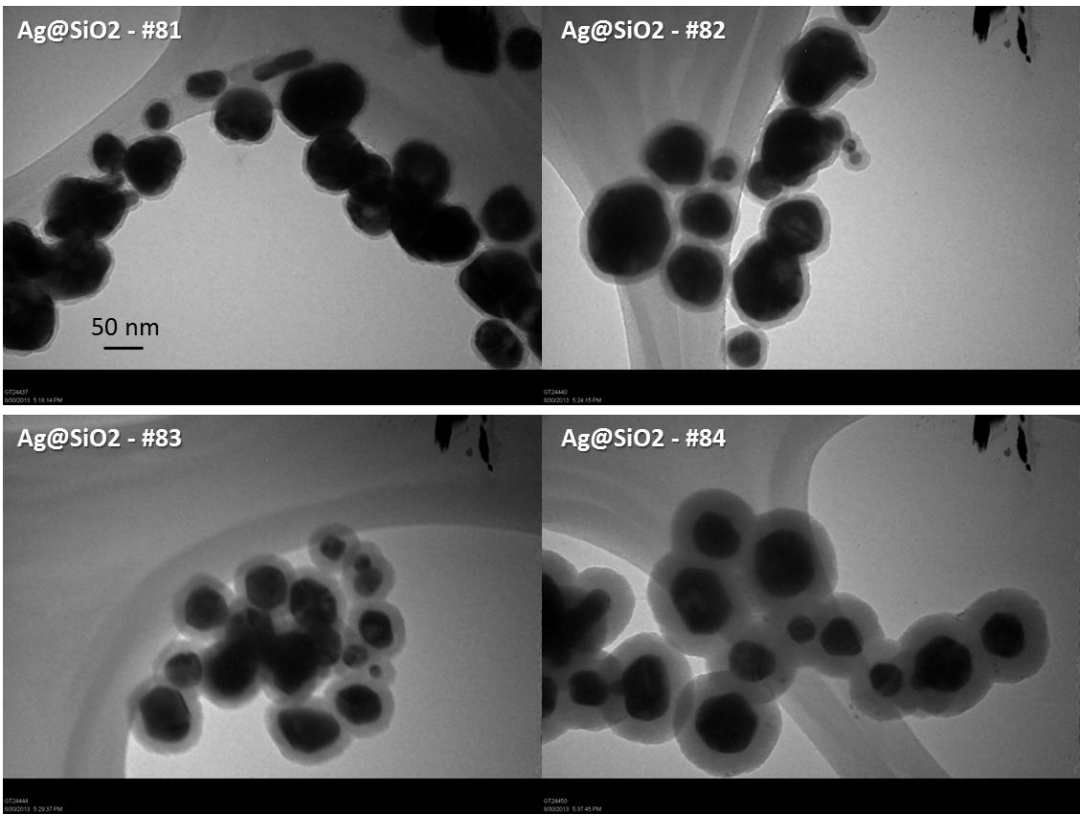

Figure 15: TEM images of $Ag@SiO_2$ nanoparticles of different shell thickness.
Nanoparticles fabricated with different amount of TEOS for SiO_2 coating. Images are of the same scale.

The LSPR extinction properties of the $Ag@SiO_2$ nanoparticles changes with the size of the Ag cores and SiO_2 shell thickness. The effect of particle size is presented in Figure 16. As the particle size increases, the peak position first red-shifted from 430nm to ~480nm, accompanying

a broadening of peak width, and then blue shifted gradually back to 420nm. Since the LSPR peak depends on many other factors such as size distribution, particle shape and inter particle distance, the existing data cannot be used to assess the impact of particle size on LSPR peak position. The inability to find correlation between Ag core sizes and the LSPR properties may be resulted from the wide distribution of particle sizes. In contrast, the impact of SiO_2 coating thickness on the peak position of LSPR is clear, as shown in Figure 17. The LSPR peak is red-shifted with increasing SiO_2 shell thickness, without causing significant peak broadening.

Thermally robust SERS capability of the $Ag@SiO_2$ NPs with different geometries was evaluated with standard GDC thin films. The GDC thin film was deposited on silicon wafers by RF magnetron sputtering, and annealed in air at 800^0C for 1hr. After loading of SERS probes through spin coating, the samples were heat treated in air at 400^0C for 1hr. The enhancement factors (EF_{net}, as defined in Section 2.3.3) were calculated by taking ratios of the peak intensities of the F_{2g} mode of GDC before and after loading of SERS probes.

The enhancement factors of SERS probes of different sizes and shell thicknesses are presented in Figure 18. As the particle size increases, the enhancement factor increases, with the AgNP-60 series reporting the strongest enhancement. As the particle diameter increases, the number of Ag atoms in the core increases. The greater the number of Ag atoms at the surface, the greater the number of valence electron involved in the LSPR field, and thus, the greater the resonance.

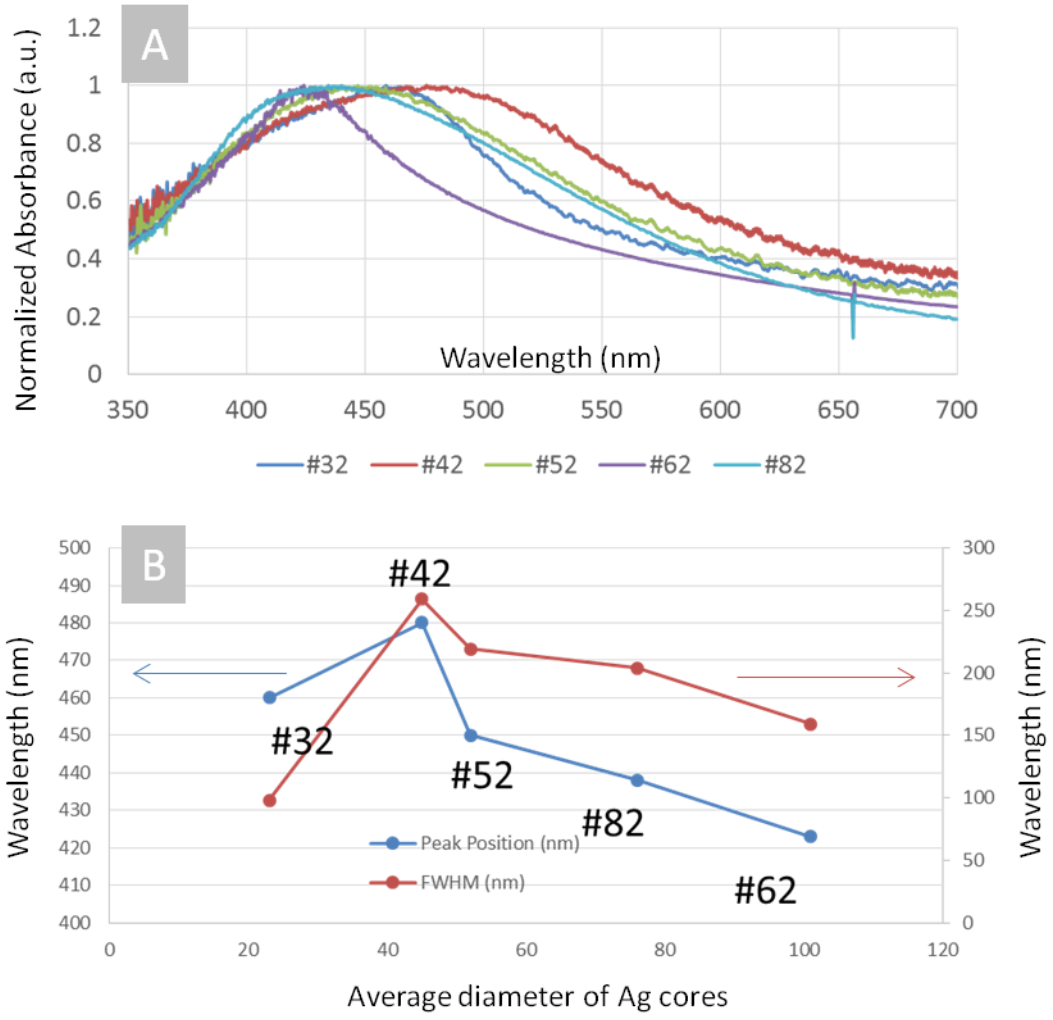

Figure 16: UV-Vis extinction properties of Ag@SiO_2 nanoparticles with different sizes of Ag cores.
(A) Normalized extinction spectra of Ag@SiO_2 nanoparticles deposited on glass slides. (B) Peak position and FWHM of the absorbance band of the Ag@SiO_2 probes. Nanoparticles with various sizes fabricated with different seeding batches (#30, #40, #50, #60, #80), and a same SiO_2 coating protocol (SiO_2 x 2).

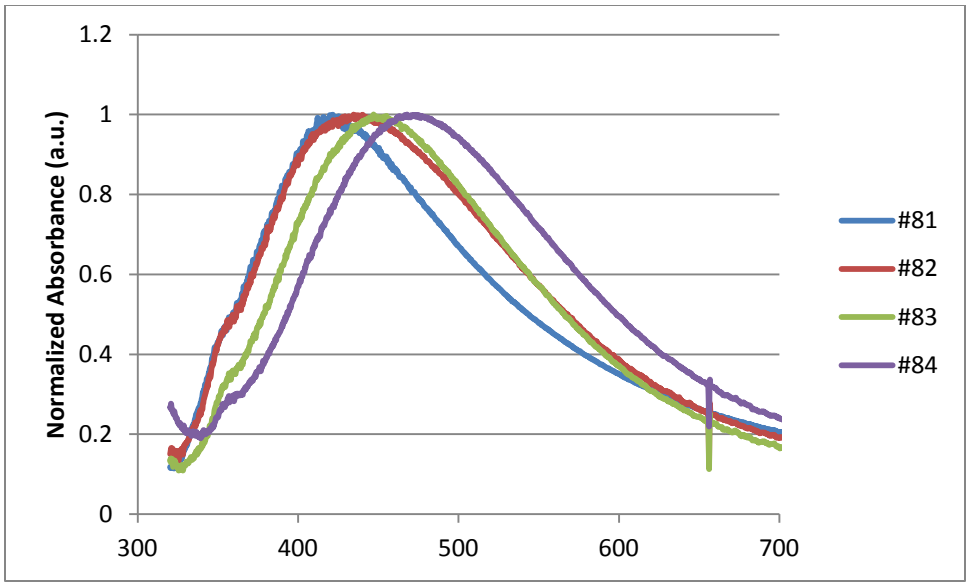

Figure 17: UV-Vis extinction spectra of Ag nanoparticles with different SiO_2 coating thicknesses.
All samples are based on a same batch of Ag cores (AgNP #80), and different shell thickness were created as a result of different TEOS concentration.

While an adequate thickness is necessary to prevent particle sintering at the annealing process at 400°C, SiO_2 with excess thickness blocks the LSPR field that enhances the Raman signal of the tested substrate. As presented in the following equation:[80]

$$I = \left(1 + \frac{r}{a}\right)^{-10}$$

In which I represents the intensity of the Raman mode after the enhancement of $Ag@SiO_2$ nanoparticles, r represents the thickness of the shell, while a denotes the size of the silver nanoparticles. The optimal SiO_2 shell thickness was found to be 10nm.

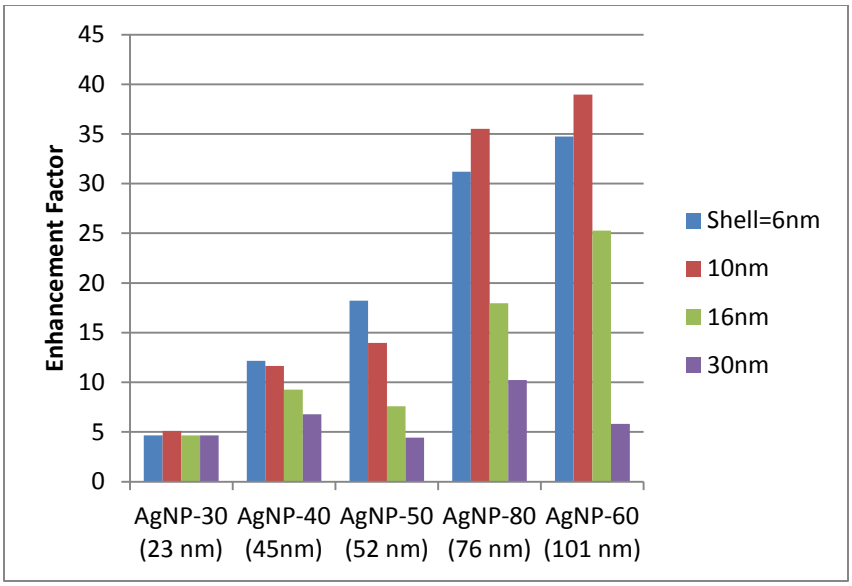

Figure 18: Enhancement factors of Ag@SiO_2 nanoprobes of systematically varied sizes of Ag cores and SiO_2 thicknesses.

The enhancement capability of the Ag@SiO_2 probes is also sensitive to the thickness of the substrate. As illustrated in Figure 19, same set of SERS probes were loaded GDC thin films deposited on silicon wafers, with two thicknesses of 90nm and 10nm, respectively. Both types of GDC thin films were annealed at 800^0C for 1hr prior to the SERS activation. The SERS tests were conducted after annealing at 400^0C for 1 hr in air, to remove all the organic residue and also test the thermal stability of the SiO_2 coating. While the ordinary Raman signal differs by ~10 times, the SERS signal are similar. This translates to ~10 fold higher enhancement factors using the thinner GDC as the substrates. The higher enhancement capability observed on thinner GDC films indicates that the SERS signal is dominated by the topmost layer that is in contact with the probes. Therefore, the SERS probes are ideally suited for the identification of trace amount of contamination phases and surface chemicals on SOFC electrodes.

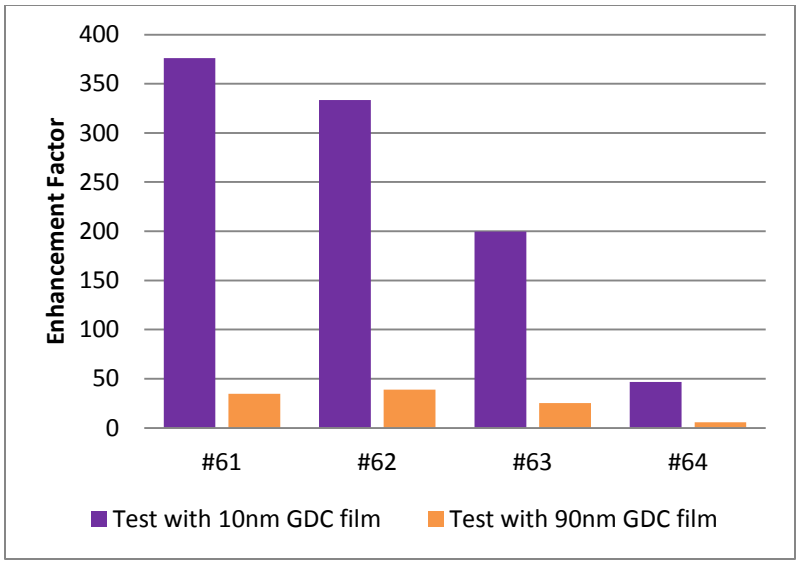

Figure 19: Enhancement factors measured by GDC thin film with different thicknesses.
SERS probes used are comprised of AgNP-60 cores with different SiO_2 thicknesses (x1 to x4), labeled as #61-#64, respectively.

The SERS capability of the $Ag@SiO_2$ SERS probes was evaluated using excitation lasers of different wavelengths. As displayed in Figure 20, core-shell nanoparticles (#61) were loaded onto the standard GDC thin films (after annealing at 800C for 1hr), and the SERS activated samples were heat treated at 400C in air for 1hr. Raman spectra were collected with excitation lasers of wavelengths of 488 nm, 514 nm, and 633 nm, respectively. Normal Raman (NR) spectra were collected from a blank GDC thin film (after annealing at 800C for 1hr), and the control spectra were obtained from a silicon wafer loaded with $Ag@SiO_2$ nanoparticles of the same kind. Raman modes of GDC were shown prominently on the SERS activated sample with all excitation wavelengths, reporting enhancement factors (EF_{net}) of ~40. The excitation laser of 514 nm wavelength reported the highest absolute intensity of the F_{2g} mode of GDC, however, inspection of the Raman spectra collected from the control sample shows that 514nm excitation results in the strongest fluorescence background.

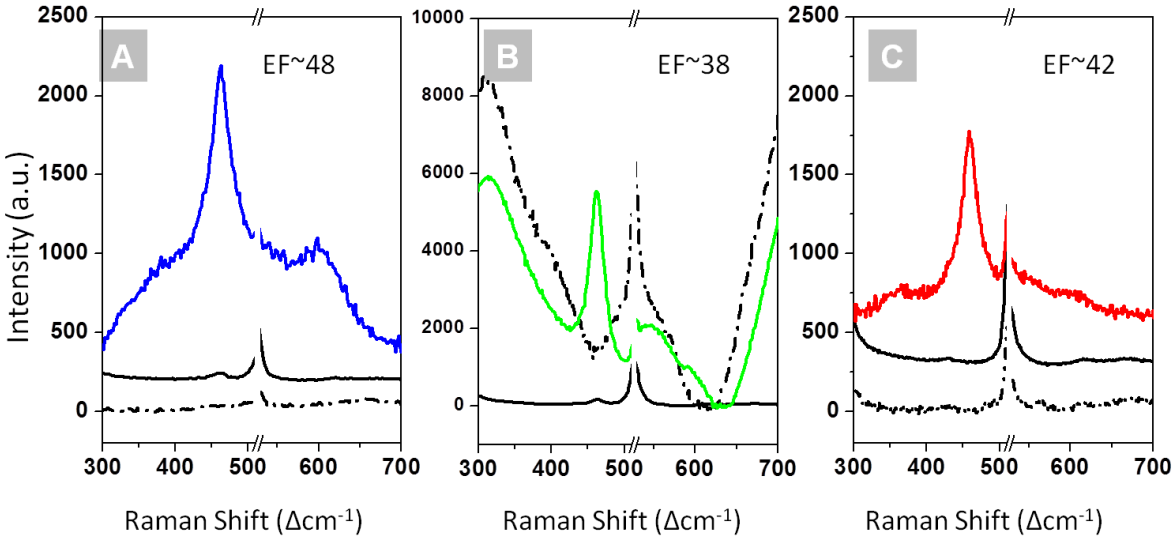

Figure 20: Effect of incident wavelengthes of lasers on the SERS capability of the Ag@SiO_2 probes.
(A) The pure Ag@SiO_2 nanoparticles (#61) loaded on silicon wafer (Ag@SiO_2|Si, dash-dot line), blank GDC thin film deposited on silicon wafer (GDC|Si, solid black line), and Ag@SiO_2 nanoparticle loaded GDC thin film after heat treatment in 4% H_2 (Ag@SiO_2|GDC|Si, solid colored line), inspected with 30mW blue laser (488nm). (B) Same samples inspected with 10mW green laser (514nm). (C) Same samples inspected with 15mW red laser (633nm). Each spectrum represents the average of spectra collected from 9 random points.

Long term stability of the Ag@SiO_2 SERS probes at elevated temperatures was evaluated upon the exposure to H_2, propane and air, as shown in Figure 21. Ag@SiO_2 nanoparticles (#61) were loaded onto an annealed GDC thin film sample, and the intensity of the F_{2g} mode was recorded when the sample was heat treated upon exposure to different atmospheres. The SERS capability retained in the high temperature testing for up to 35 hours, although when heated in air, the SERS efficiency dropped significantly. This test suggests the SERS probes are reliable for qualitative analysis of surface species, while its application for quantitative analysis needs further validation, especially when gas switching is involved.

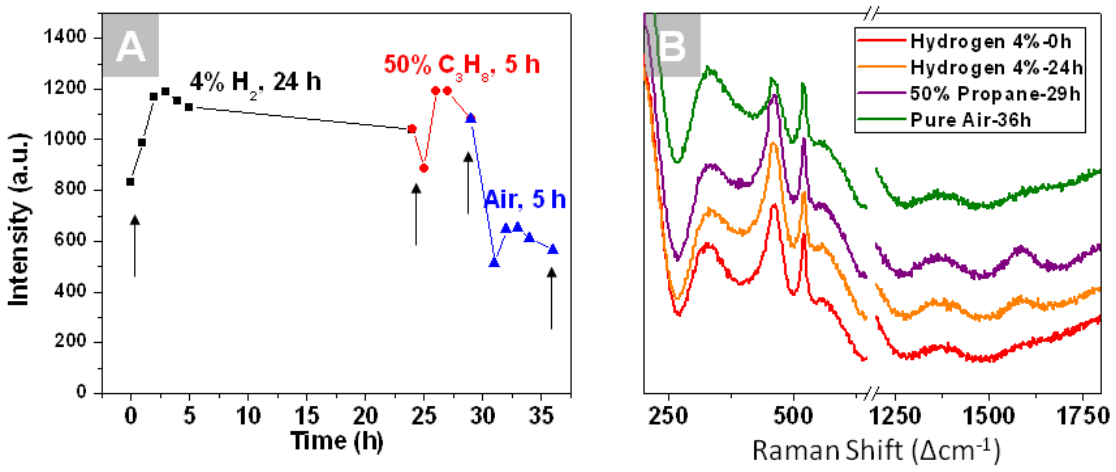

Figure 21: Long term thermal stability of the Ag@SiO_2 nanoprobes.
SERS probes (#61) were loaded onto GDC thin film upon heat treatment 450^{0}C under 4% H_2, 50% C_3H_8 and air with an excitation wavelength of 514nm. (A) The F_{2g} band intensity collected *in situ*. (B) The Raman spectra taken at different time during the heat treatment experiment, as indicated by the arrows in (A). Each spectrum represents the average of spectra collected from 9 random points.

In summary, the LSPR properties and SERS capability of the Ag nanoprobes coated with SiO_2 shell can be adjusted through fine-tuning the geometric factors. The optimal fabrication protocol that maximizes the enhancement factor was determined experimentally. In general, Ag nanoparticles with larger cores (up to 100nm) and thinner shells (~10nm) displays better SERS capability. The stability of the SERS probes was evaluated upon long term heat treatment under 4% H_2, 50% C_3H_8 and air, showing reasonable robustness for qualitative analysis. These results demonstrate the feasibility of using Ag@SiO_2 NPs for SERS study of SOFC materials under *in situ* conditions. Loading these SERS probes onto the electrode surfaces may help to identify the surface intermediates and incipient species on the SOFC electrode surfaces during operation, as schematically shown in Figure 22.

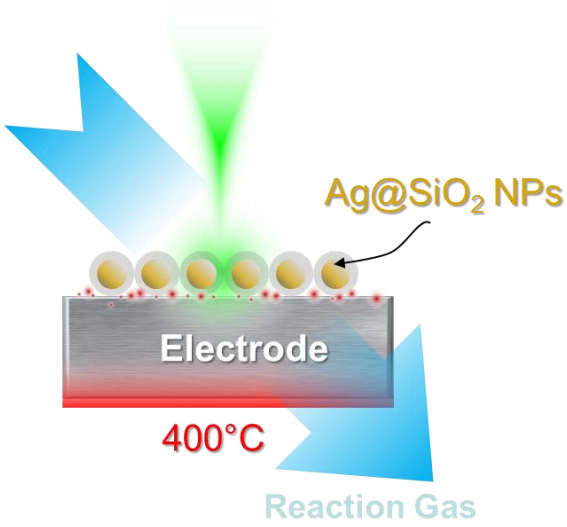

Figure 22: Schematic of *in situ* SERS analysis of SOFC electrode materials.

3.4. Electrostatic Force Microscopy

Electrostatic force microscopy (EFM) detects the local surface potentials by sensing the electrostatic force between the conductive AFM tip and the sample, offering simultaneous topography and surface potential images with nanoscale spatial resolution. In this study, a MultiMode AFM equipped with MMEFCH electrical sample holder and MikroMasch NSC-16Au coated tips was used for EFM analysis. A detailed hands-on operation protocol is presented elsewhere. [104] In practice, the samples are usually biased positively or negatively vs. the tip, providing enhanced contrast for surface species identification.

As shown in Figure 23(A), EFM signal is acquired in an interleave mode: the AFM tip first scans across the sampled region to collect topography profile, and then raises a constant distance (20-30nm) to travel across the same region. The topography profile collected on the first trip generates the moving trajectory for the second trip, in which the tip is set to the EFM mode to gauge the electrostatic force from the scanned region. Displayed in Figure 23 B is the

detection mechanism of EFM.[105, 106] The electrostatic force between the tip and the sample acts like a spring tethered to the AFM tip that changes its vibration frequency. As the tip is set to vibrate at its free resonance frequency (f_0) during the EFM scan, the electrostatic interaction translates into a change in vibration phase angle ($\Delta\varphi$), which is registered as EFM image. Since the electrode materials and surface degradation species, (e.g., nickel, carbon, and BaO) have different surface potentials that originate from their different work functions, the tip experiences different magnitude of electrostatic interaction and is reflected in the EFM image.

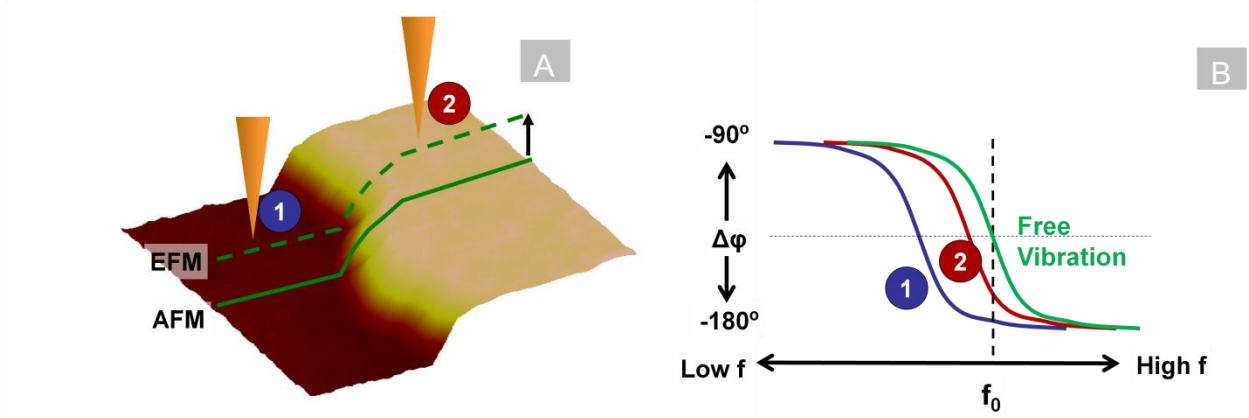

Figure 23: Schematic of electrostatic force microscopy (EFM).
EFM was performed simultaneously with AFM. Due to the difference of surface potential between point 1 and 2, the electrostatic force changes, which incurs the shift of natural resonance frequency of the AFM tip that results the difference in phase angle ($\Delta\varphi$).

The sensitivity and spatial resolution of EFM towards carbon deposition on nickel surface was evaluated with a model interface created by evaporated carbon. Carbon was deposited onto a polished nickel foil with a Kepton tape template, which was subsequently removed to reveal the edge of carbon film. Topography and EFM images were collected simultaneously across the edge of evaporated carbon film, as displayed in Figure 24(A-B). The $\Delta\varphi$ image collected by EFM manifested clear contrast between carbon covered region and bare nickel surface with spatial resolution less than ~50nm. To validate that the phase angle contrast is due to the electrostatic

interaction, EFM linescans were obtained across the interface with different sample biases, as displayed in Figure 24(C). When the sample bias potential (U) varied from 1.5 V to -1 V, the phase angle contrast between the two regions reversed, corroborating the fact that the EFM contrast find its origin in the difference of surface potentials between nickel and carbon.

The EFM contrast of different surface species is originated from their difference in surface potentials. The correlations between $\Delta\varphi$ and sample bias (U) on both carbon and nickel phases were plotted in Figure 24(D). The magnitude of $\Delta\varphi$ is proportional to the square of contact potential difference between the AFM tip and the scanned region. The maximum of the $\Delta\varphi$-U curve corresponds to the bias (U_0) at which the electrostatic force is minimized, signifying that surface potential of the sampled region and that of the gold coated tip equilibrate. Comparing the $\Delta\varphi$-U curves collected on nickel and on carbon showed that $U_{o,\,Ni}$ is about 0.5V higher than that of $U_{o,\,C}$. Figure 24(E, F) schematically shows the energy diagrams of Ni, carbon and the gold coated tip under different sample biases, illustrating the origin of EFM contrast. Since the surface potential is mainly determined by the work function of material in addition to the dipoles formed by adsorbed layers, this observation is consistent with the fact that nickel has higher work function than carbon. [107, 108]

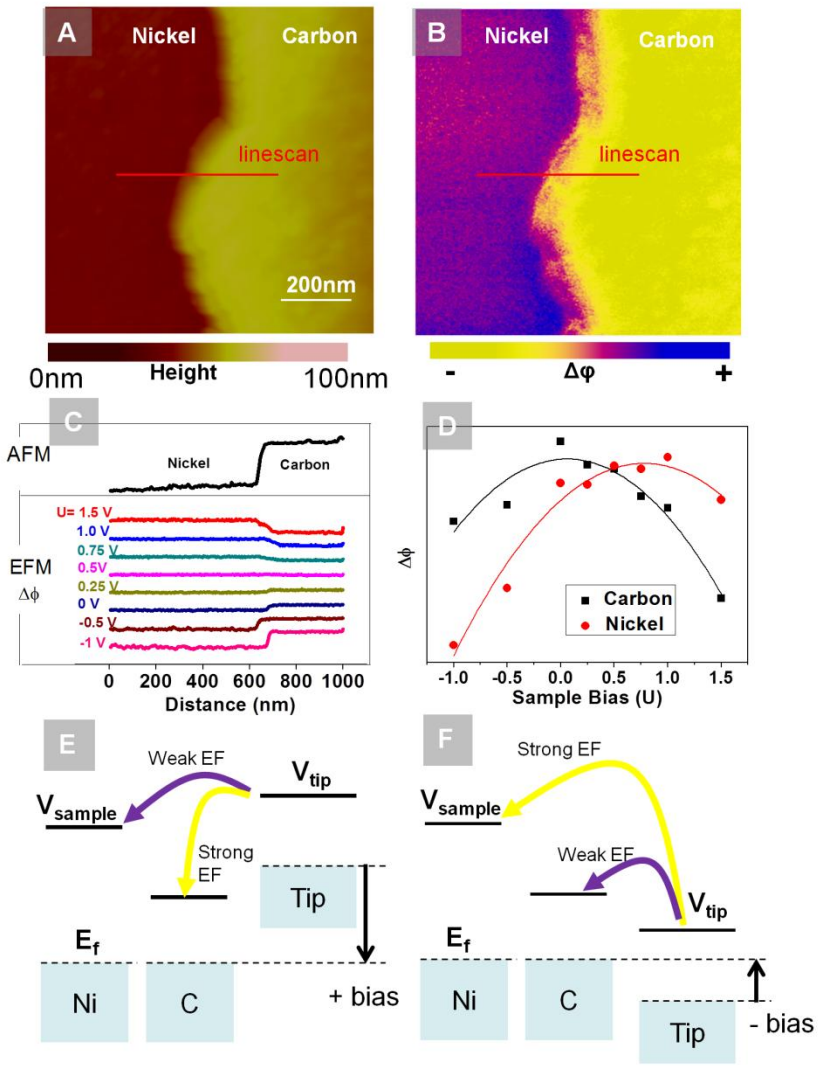

Figure 24: EFM response of simulated carbon-Ni interface and the origin of the phase angle contrast.
(A) The surface topography of the carbon covered area and blank nickel. (B) The EFM image acquired on the same area with the sample biased at 1V. (C) The topography and EFM phase angle collected from a line scan over the carbon-nickel interface. (D) The EFM phase angle curves as functions of applied sample bias, collected from the carbon loaded area and blank nickel regions, respectively. (E) The energy diagram of electrons in nickel (sample), carbon (sample) and gold AFM tip, sample being biased with positive potential and (F) with negative potential. The electrostatic force (EF) determined by $(V_{sample}-V_{tip})^2$.

Differentiating BaO from Ni under EFM mode is more difficult, since the BaO and Ni have similar surface potentials. Displayed in Figure 25 are the AFM topography and the corresponding EFM images of the BaO nanorings deposited on nickel surfaces under different

sample biases. When the sample was biased positively (+2V), the BaO nanocatalysts showed stronger interaction with the tip, manifesting negative contrast in the phase angle image; while when the sample was biased negatively (-2V), the BaO nanoparticles showed weaker interaction. The phase angle curve as the function of bias potential (Figure 26) shows that BaO has slightly higher surface potential than Ni, consistent with the surface potential mapping. While the capability of EFM to differentiate Ni and BaO is not as prominent as Ni and carbon, the BaO nanoparticles with unique feature or patterns still make possible of phase identification.

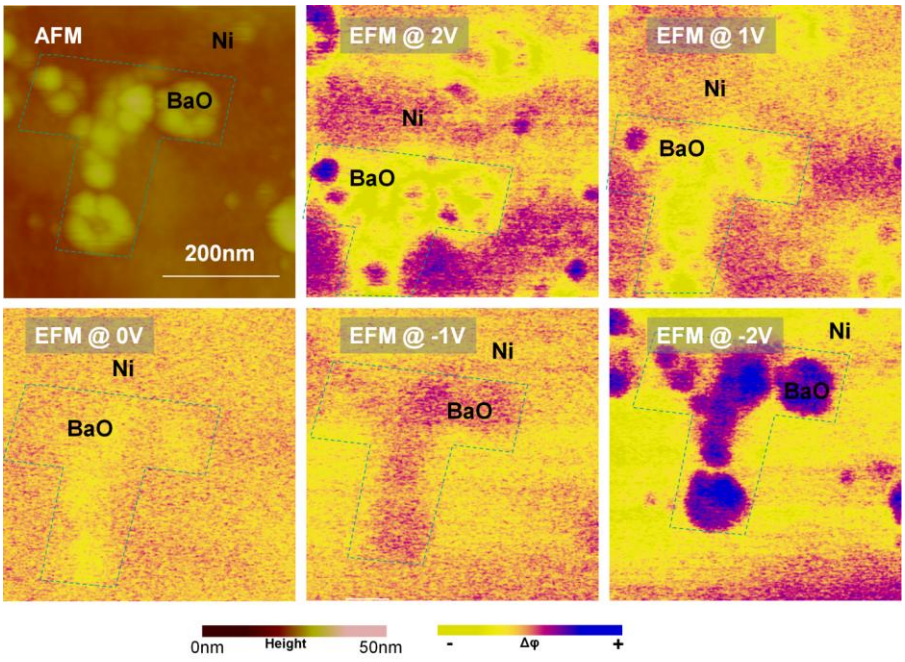

Figure 25: AFM and the corresponding EFM images BaO nanorings loaded on nickel surface.
The potential value shown in the EFM images are the bias applied to the sample. The T-shape regions enclosed in the dashed lines consist of several BaO nanorings.

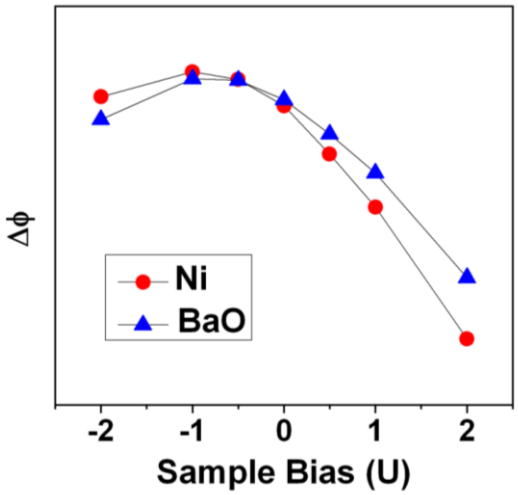

Figure 26: Surface potential difference between Ni and BaO.
Phase angle curves as functions of applied sample biases were obtained from EFM analysis of the BaO nanocrystals and blank nickel regions, respectively.

3.5. Patterned Electrodes

Fabrication of patterned electrodes is key to isolating the intrinsic properties of SOFC electrode surfaces governing the electrochemical reactions and degradation processes. In this study, patterned microelectrodes of cathode materials (LSM and LSCF) were fabricated by RF magneton sputtering. The patterned electrodes of Ni were created with an embedded mesh method. The patterning of surface catalysts, such as BaO and Yb_2O_3, on the surface of Ni, was achieved by block copolymer templates and photo lithography, which is described separately in Section 5.1.

3.5.1. Magnetron Sputtering of Patterned Micro Electrodes

Patterned micro-electrodes can help to to identify the reaction paths through systematic variation of electrode sizes and geometries. By elimination of the geometric randomness, the intrinsic properties of the electrode can be revealed. For instance, Fleig et al. [109] measured the

polarization resistance (R_p) of dense circular LSM electrode of different diameters (D), and correlated the R_p-D relationship with the dominant oxygen reduction paths: If the oxygen reduction is through bulk path, $1/R_p$ will scale with the D^2. While if the surface-TPB path is dominating, $1/R_p$ will scale with D. In this way the authors demonstrated that the bulk path of LSM opens up under cathodic bias, while under anodic bias, only surface-TPB path is active for oxygen reduction.[109] Similar studies on Pt electrode, indicate that the oxygen reduction process is fully controlled by the TPB path. [110]

Patterned LSCF and LSM electrodes were fabricated through radio frequency (RF) magnetron assisted sputtering of the corresponding targets. Sputtering target preparation and detailed working parameters were systematically studied previously. [111, 112] In this study, the working pressure during LSM and LSCF sputtering was set at 2.5x10-2 mBar, with a constant power output of 20W. Thickness of the electrodes was controlled by sputtering duration (1 - 4.5 hrs), as calibrated in previous studies.[111, 112] Modification materials, including GDC, SSC and LSM, were also introduced to the LSCF patterned electrode through RF sputtering. The GDC and SSC target were also fabricated by powder dry-pressing followed by sintering for 5 hours at 1450^0C and 1250^0C, respectively. The amounts of surface catalysts were controlled by sputtering time (1-10 mins).

Electrolyte substrates were fabricated by dry pressing GDC powders and sintering at 1450^0C for 5hrs. The electrolyte disks have roughly 8mm in diameter and 0.5mm in thickness. For the deposition of patterned electrodes, one side of the electrolyte pellet was polished with 6 μm diamond grids followed by 3 μm, 1 μm and 0.1 μm of diamond suspensions (Allied High Tech).

Nickel mesh grids (SPI) with different open sizes were used as templates to control the sizes of the patterned electrodes. Prior to sputtering deposition of electrodes, nickel grids were pressed onto the polished side of the electrolyte pellets and secured by Scotch tape. During the sputtering, electrode materials deposited onto the electrolyte through the openings on the nickel mesh grids. Square patterned electrodes with different sizes (~40 um, 71 um, 111 um and 145um) were fabricated with this method on the same sample. The patterned electrodes are clearly isolated, while the edges of patterned electrodes spread into a width of 1-2um, it does not impact on the determination of the dominant ORR paths or the evaluation of surface modification catalysts.

The patterned electrodes were tested under a home-made micro-probe impedance station, as illustrated in Figure 27. A Harrick environmental chamber was used to control the temperature. The electrolyte pellets with the patterned electrodes were secured on the hot stage by silver paste (EMS 18DB70X), which also serves as counter electrode, with the metal body of the hot stage as the current collector. During the test, a tungsten carbide tip is pressed onto individual electrodes to make current collection. The impedance spectroscopy was conducted with a Solartron dielectric interface (SI-1296) combined with a Solatron frequency analyzer (SI-1255). Impedance spectra measured under OCV, with 50mV excitation signal.

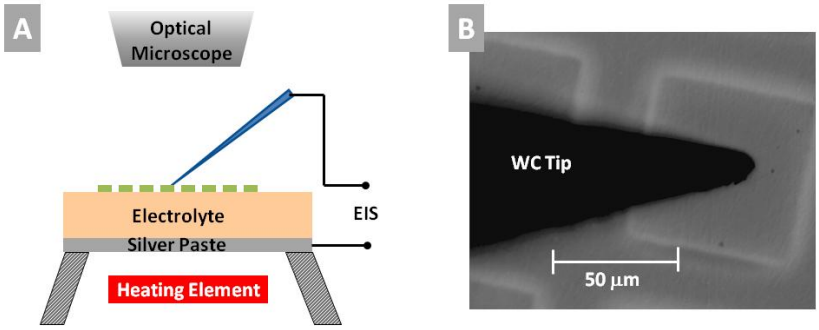

Figure 27: Schematic of micro-probe EIS testing of model cells with patterned electrodes.

The components of the response circuits contains 1) the current collection resistance from the tungsten carbide tip, 2) the polarization resistance of the patterned electrode, 3) the spreading resistance (Ohmic) of the GDC electrolyte and 4) the polarization resistance of the counter electrode, as illustrated inFigure 28(A).

Current collection resistance contains the Ohmic resistance of the tip and the contact impedance between the tip and the patterned electrode. The Ohmic resistance of the tip, R_{tip}, is negligible due to the high conductivity of tungsten carbide, and can be excluded in the equivalent circuit simulation. The contact impedance R_{CC} is related to the pressure applied on the WC tip, as demonstrated in Figure 28(B, C). The different pressures applied by the WC tip have an impact on the medium frequency arc of the impedance spectra. Therefore, the medium frequency arcs were subtracted from the Rp to simplify the mechanistic study. Also, to minimize the influence of Rcc, the tungsten carbide tip was securely pressed on the patterned electrodes during the testing.

The spreading resistance is determined by the ionic resistance of GDC, and is related to the size of the micro electrodes. The spreading resistances for patterned electrodes of electrodes

of different sizes and at different temperatures are calculated intoTable 4. The estimation of spreading resistance follows the following formula:

$$R_{sp} = \frac{\rho}{4r}$$

in which ρ represents the resistivity of GDC and r denotes the size of the patterned electrode. For all temperatures and electrode sizes, the spreading resistance accounts for <1% of the polarization resistance, and therefore has little impact on the interpretation of electrode behaviors.

Table 4: Spreading resistance of GDC for electrodes of different sizes at testing temperatures.

Temp	34um	63um	99um	133um
650	2768.587	1494.158	950.8279	707.7591
600	4475.574	2415.389	1537.066	1144.132
550	8131.019	4388.169	2792.471	2078.606
500	25065.1	13527.2	8608.218	6407.621

To evaluate the impedance of counter electrode (R_{ct}), a model GDC cell with Ag as both electrodes was tested in the environmental chamber at 500^0C and 600^0C, as shown in Figure 28(D, E), respectively. Again, the impedance of counter electrode is negligible compared to the polarization resistance and thereby neglected in the analysis of the patterned electrodes.

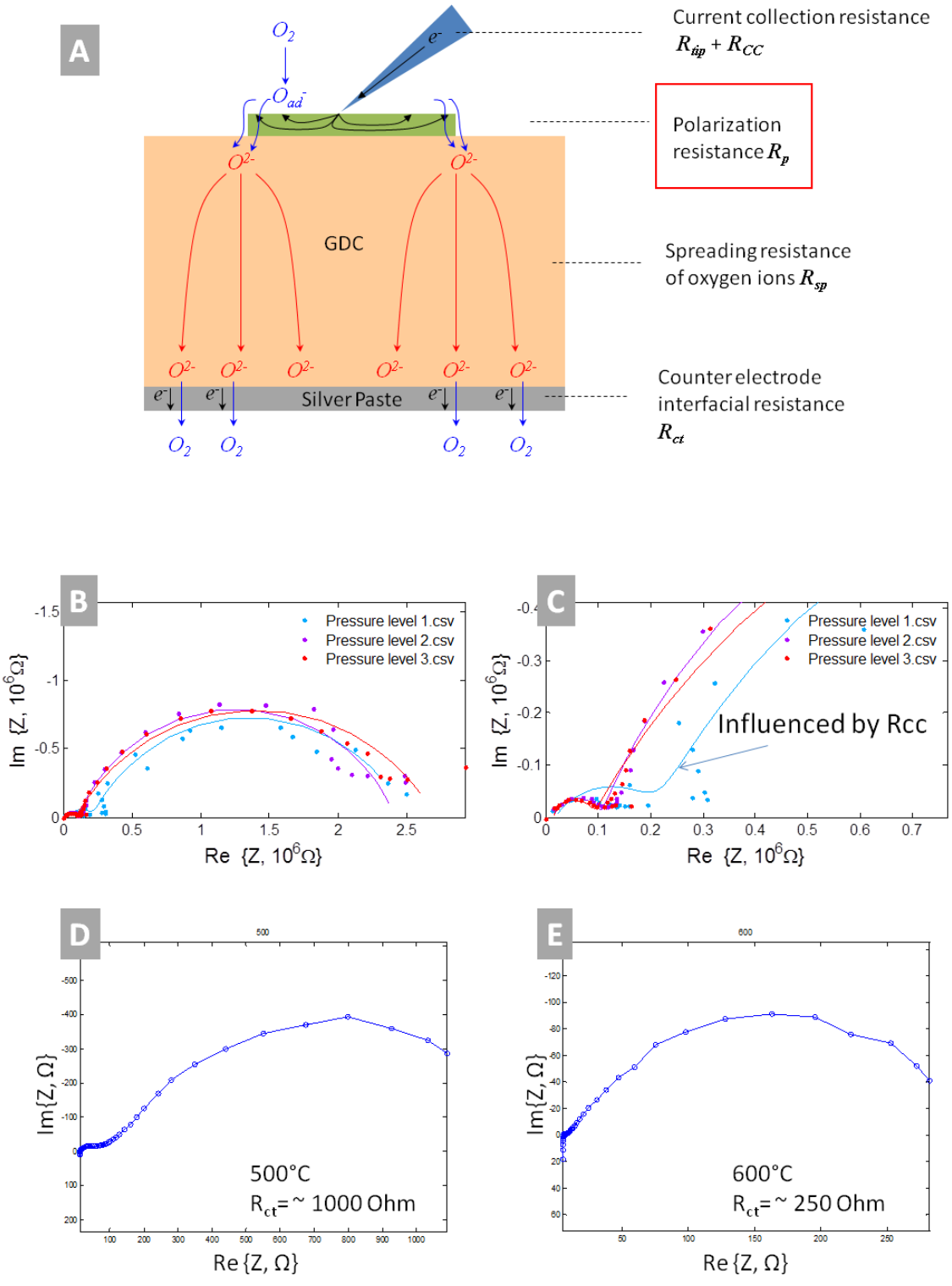

Figure 28: Analysis of components constituting micro EIS testing cirtuit.

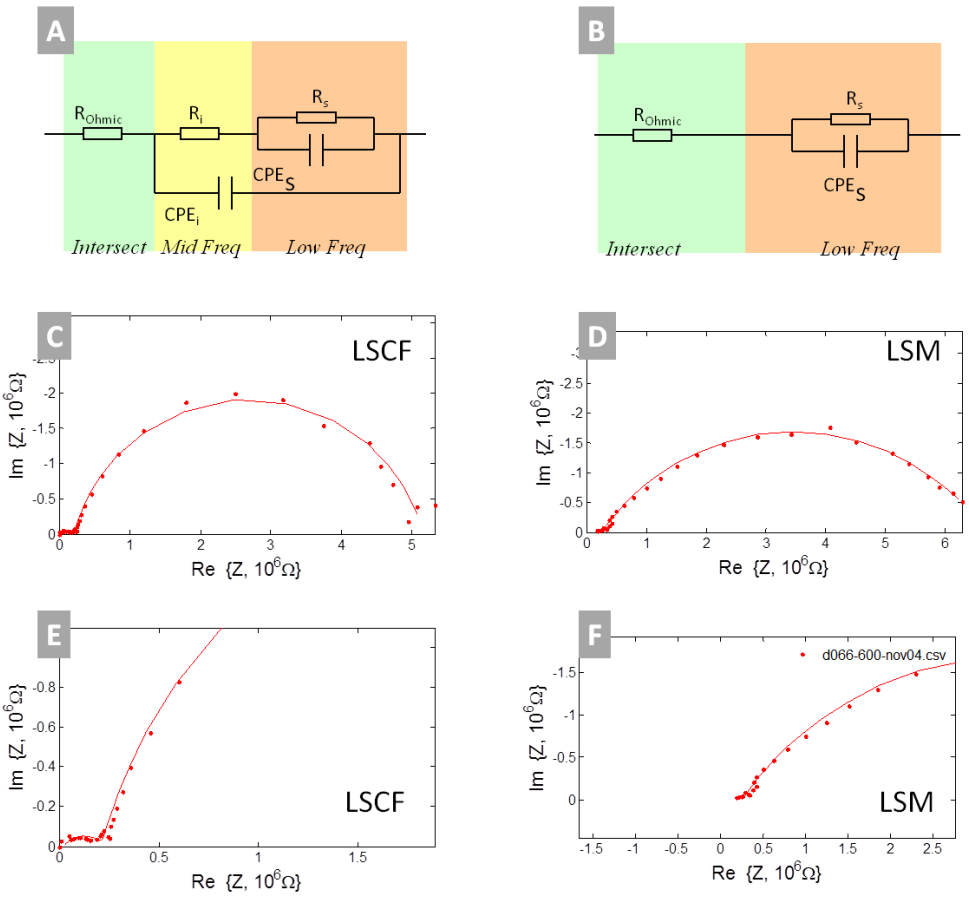

Figure 29: Equivalent circuit analysis of the micro patterned electrodes.
(A, B) The equivalent circuit used to simulate the impedance spectroscopy of LSCF and LSM, respectively. (C, D) Typical impedance spectrum collected from 66um LSCF and LSM patterned electrode at 600^{0}C, with the simulation by equivalent circuit. (E, F) The details of the high-mid frequency range of the impedance data points and the simulated spectra.

Matlab based protocols were developed to simulate the equivalent circuits of the patterned electrodes of different materials, as presented in Figure 29. The impedance spectra of LSCF are interpreted using an equivalent circuit that accounts for the surface oxygen exchange and oxygen transfer through the LSCF-GDC interface[113], as displayed in Figure 29 (A, C, E). In this study, the low frequency arcs dominate the impedance response, and only under high temperatures when the total impedance is lower, the medium frequency arc becomes

distinguishable. Therefore, the resistance component (Rs) of low frequency arcs is extracted as the polarization resistance. For LSM electrodes, there is only one lumped arc for all electrode sizes and temperatures. Therefore, lumped polarization resistance (Rp) are extracted from these single arcs, [114] as shown in Figure 29 (B, D, F).

3.5.2. Patterned Electrodes by Embedded Mesh

To fabricate cells with well defined nickel-electrolyte interface, an embedded-mesh method was employed. As illustrated in Figure 30 , electrolyte powders (YSZ or BZCYYb) were pressed into pellet with nickel mesh embedded. The green pellets with sandwich structure were then sintered in 4% H_2 (balanced by Ar) at 1450°C for 5hs to densify the electrolyte and secure its contact with Ni mesh. The sintered samples were grinded and polished with diamond suspensions on one side to remove the excess electrolyte enclosure and to reveal the interface between Ni and the electrolyte. [104]

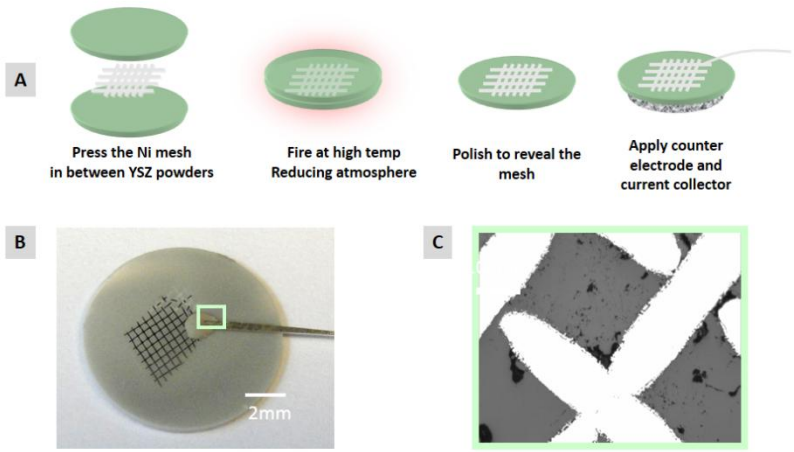

Figure 30: Fabrication of patterned electrodes through embedded mesh method.
(A) Schematic of fabrication, (B) Camera and (C) Optical microscope picture of the surface after grinding and polishing.

Because the strands of the embedded metal mesh are interconnected, the current collecting can be easily achieved by attaching a gold wire on the corner of the revealed mesh with a small amount of platinum paste. Fritted platinum paste was applied on the opposite side as the counter electrode. The patterned electrodes showed versatility in material choice and design of architecture, providing unique capability in isolating the contribution of different components of the interface.

For full cell testing: To test the patterned electrode in a full cell configuration, Pt paste (Heraeus) was applied to the side opposite to the revealed patterned electrodes as the counter electrode (and current collector). On the polished side, Au wire was attached to the Ni mesh with a tiny drop of Pt paste just enough to ensure good electrical contact but not too much to avoid influence on the measurement of the electrochemical performance. The current collectors (Pt pastes) were fired at 900°C for 1 hr to form a strong electrical contact. Afterwards, the sample was mounted onto an alumina tube for the electrochemical tests. The established cell was first annealed in air at 100^0C for 1hr and 260^0C for 1hr to cure the sealant, and heated to 800^0C for 1hr under H_2 to stabilize the surface of nickel mesh. The furnace temperature then descended to values for cell testing.

For *in situ* **Raman and SERS**: The open structure of the patterned electrode also allows *operando* probing and mapping by Raman spectroscopy in parallel to the electrochemical testings. The specially designed environmental chamber can apply polarization to the Ni-electrolyte interface while the temperatures and atmospheres are properly controlled. SERS probes can also be deposited onto the surface of patterned electrodes for the study of intermediate species on the electrode interfaces, as shown in Figure 31.

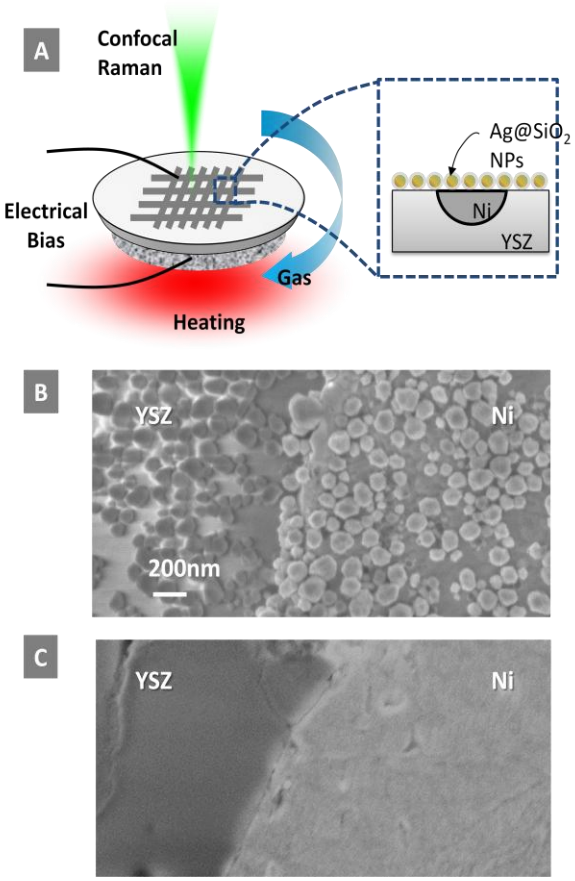

Figure 31: *Operando* SERS analysis of well-defined nickel-electrolyte interface.
(A) The schematic of the *in situ* SERS testing cell composed of patterned Ni electrode embedded in YSZ pellet, with $Ag@SiO_2$ nanoparticles deposited as the SERS probe. Au wire was used as the current collector for the patterned electrode, while the counter electrode was electrically connected to the metal body of the Raman chamber. (B) The SEM image of a typical SERS activated Ni-YSZ interface after testing at elevated temperatures, and (C) The Ni-YSZ interface without the SERS probes.

CHAPTER 4: CARBON DEPOSITION ON NICKEL-BASED ANODE

Hydrocarbon fuels usually bring forth carbon deposition, or "coking", on the nickel-based SOFC anode materials, resulting in performance degradation.[36] To achieve rational design of SOFC anode materials, in-depth knowledge of the interaction between hydrocarbon fuels and the anode surface under operating conditions is imperative. Especially, the kinetics of carbon deposition at early stage can help to identify the intrinsic coking propensity of material surfaces.

This chapter utilizes the *ex situ*, *in situ* and *operando* surface enhanced Raman spectroscopy (SERS) to study the early stage carbon deposition on nickel surface. The enhanced sensitivity makes possible of detection of coking at its incipient stage, and correlates the degree of coking to the amount of propane exposure. In particular, *operando* SERS analysis of the Ni-YSZ interface revealed the function of the triple phase boundary during the process of carbon deposition and removal. CeO_2 modification was found to enhance the coking resistance of Ni significantly, and *in situ* SERS analysis showed that doped ceria inhibited coking initiation on nickel surface. In addition, the functionality of CeO_2 was studied with *in situ* SERS, and surface oxygen vacancies were identified during the red-ox gas exchange.

4.1. Study of Early Stage Carbon Deposition

To simulate the early stage carbon deposition on nickel-based anode, a polished nickel foil (purchase from Alfa Aesar, 1mm thick sliced into coupon of 1 cm size) was exposed to mixed gas composed of 15% H_2, 10% propane and 3% H_2O in argon in a quartz tube at 550ºC for 2 minutes to build up carbon deposition. With a flow rate of ~150 sccm, the total volume of

propane introduced to the reactor was ~30 mL. During the heating and cooling process, the quartz reactor was purged with 15% H_2, 3% H_2O and 82% Ar. After the exposure test, the foil was inspected with SEM, ordinary Raman, and SERS following Ag sputtering using 633 nm excitation.

The optical and SEM micrographs of the nickel foil are shown in Figure 32(A) and (D). Patches of discoloration form on the nickel surface. Raman spectra of domains of different degree of discoloration are shown in Figure 32 (B) and (C). Under ordinary Raman, only the dark region shows significant Raman bands associated with carbon, while the bright region does not have any features with an appreciable signal-to-noise ratio. After SERS treatment by Ag sputtering for 180 s, the carbon signal in the dark region (Figure 32C) increased by several folds. More prominently, carbon peaks appeared sporadically in the light regions (Figure 32 B). The SEM images under high magnification collected before any silver deposition, show that the dark regions were fully covered in carbon, while in the bright region only some white dots formed on the surface (Figure 32 E, F). The degrees of discoloration, intensities of carbon bands in Raman spectroscopy and SERS and the microstructures collected from these two different regions suggest different degrees of carbon deposition. The difference in coking propensities find their origin in the different orientation of grains, which revealed different crystal faces after polishing. SERS enhanced the detection sensitivity towards early stage carbon deposition.

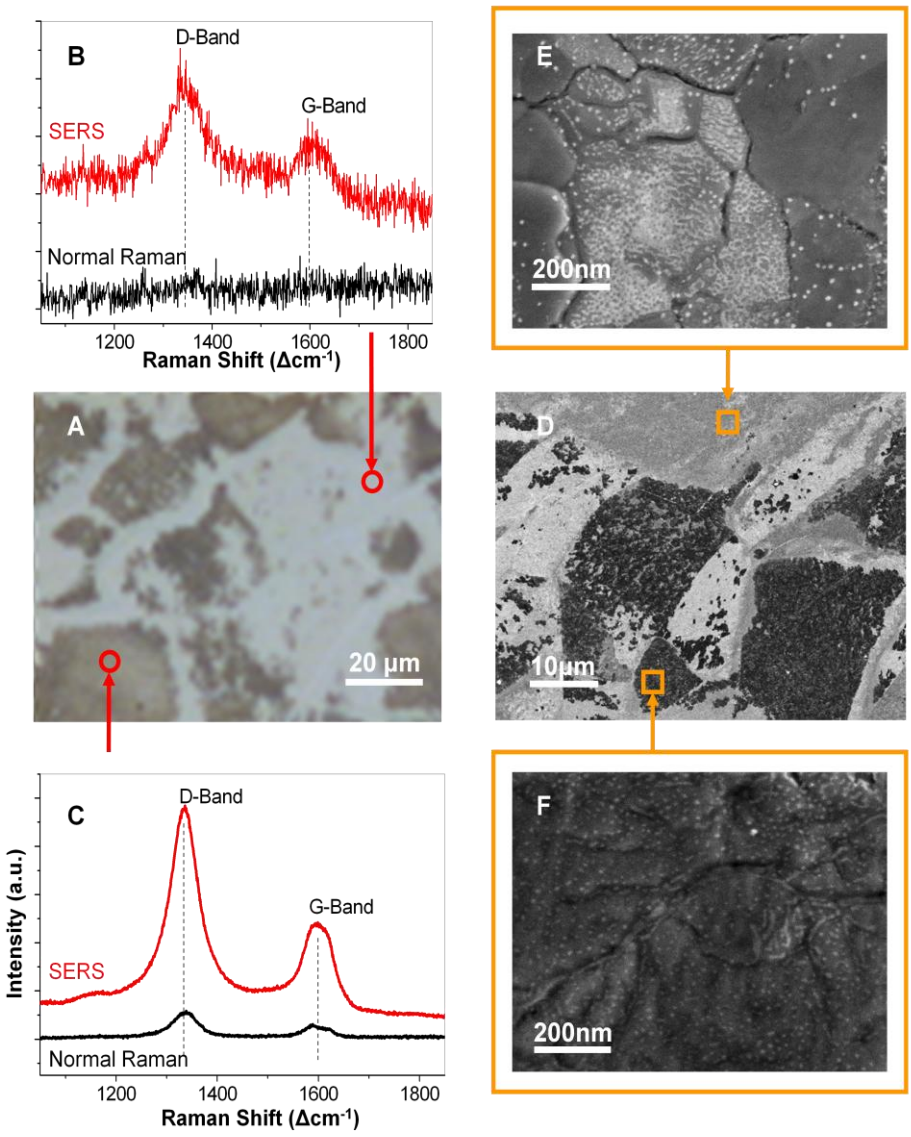

Figure 32: *Ex situ* SERS identification of early stage carbon deposition on nickel surface.
(A) Optical micrograph of hydrocarbon-exposed nickel surface and (D) SEM image with low magnification, both showing patches related to different grades of carbon deposition. (B) The Raman spectroscopy and SERS analysis of the mildly coked region and (C) of the heavily coked region.. (E) The high magnification SEM of mildly coked region and (F) heavily coked region. SEM images (D, E, and F) were taken before any silver deposition. All Raman spectra were collected with 633 nm laser, and the silver deposition duration was 180 s.

The process of carbon deposition was monitored *in situ* using $Ag@SiO_2$ nanoparticles as the SERS providers to enhance the sensitivity. Figure 33(A,B) show the time-resolved normal Raman and SERS study of a polished nickel surface exposed to wet propane at 450 °C,

respectively. In both occasions, the carbon D-band and G-band increased over time, but the SERS activated sample showed much higher intensity and signal-to-noise ratio. The signals strength of the carbon D-band and G-band are both enhanced significantly. In Figure 33(C), the integrated area under the carbon D-band for both samples was plotted over time. The signal intensity from the SERS activated sample shows a better-resolved trend: carbon quickly deposited on the nickel surface initially and the deposition rate slowed down over time. The coked samples were then exposed to a gas mixture composed of 1% O_2, 3% water vapor and 96% Ar. The time-resolved Raman and SERS spectra of this carbon removal experiment, along with the integration of carbon D-band are shown in Figure 33(D, E, and F), respectively. In both cases, carbon peaks decrease with the introduction of oxygen. As evident from the SERS data (of higher sensitivity), most deposited carbon was removed within 1000 s. The contribution of carbon deposition on SERS nano-probes and the possibility of enhanced carbon deposition in the presence of $Ag@SiO_2$ nanoparticles are found negligible, through careful control experiments reported elsewhere. [115]

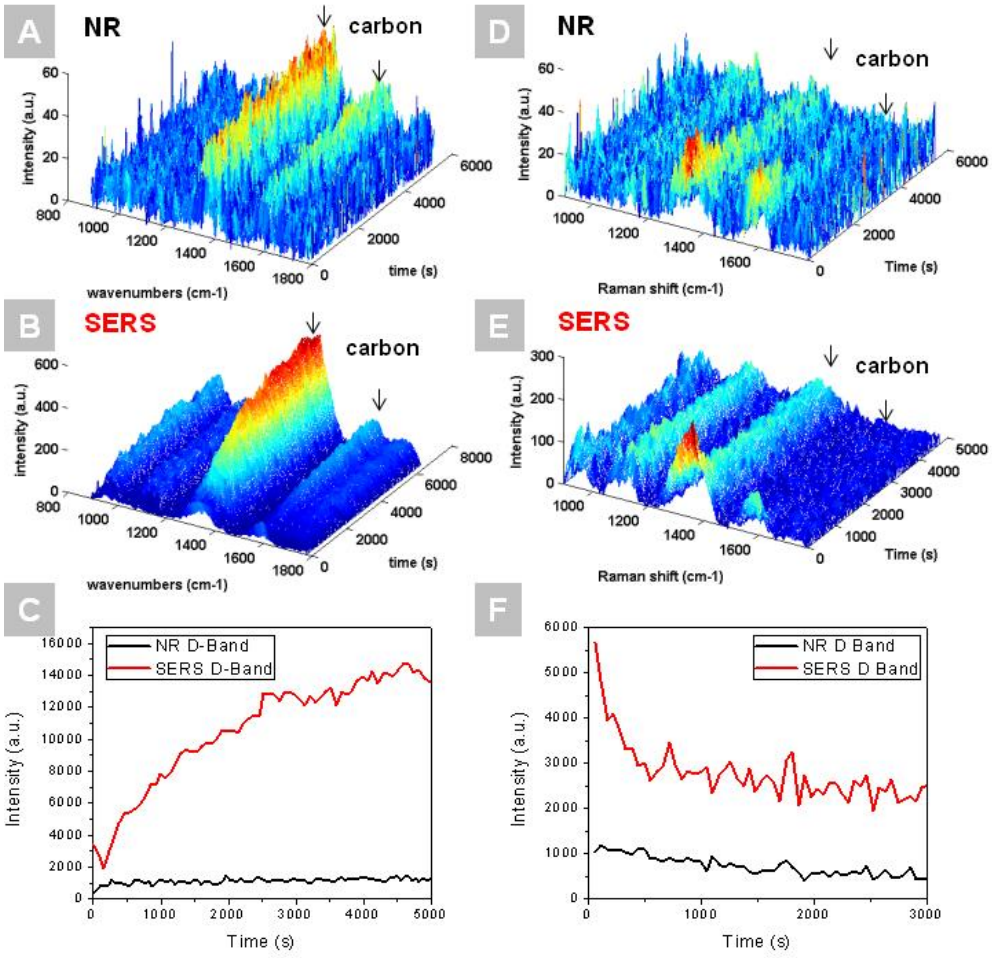

Figure 33: *In situ* normal Raman (NR) and SERS analysis of carbon depostion and removal.
(A-C) Monitoring the carbon deposition process on nickel surface through wet propane exposure at 450 °C (A) on Blank Ni (B) on Ag@SiO_2 loaded Ni and (C) Integrated intensity of carbon D-band at 1350 cm^{-1}. (D-E) Monitoring the subsequent removal of carbon deposition through exposure to wet 1% O_2 (D) on Blank Ni (E) on Ag@SiO_2 loaded Ni and (F) integrated intensity of carbon D-band at 1350 cm^{-1}. Each individual spectrum is taken with the 514 nm laser at 5 mW with an acquisition time of 10s.

While *in situ* SERS provided significant enhancement of the carbon signals developed on nickel surface, the continuous exposure to wet propane introduces carbon deposition too fast, and the spectra collected cannot represent the amount of carbon deposition at very early stage. In order to quantify the effect of early stage carbon deposition, short pulses of propane were utilized to deliver propane into the chamber. During the 10-15s pulses, 50% propane (2% H_2 and 48% Ar)

flow into the chamber, with an equivalent propane volume of 10-20 mL. Afterwards, the chamber was purged with dry 4% H_2 (96% Ar) for spectra collection (2 mins per spectrum). In contrast to the continuous flow of high concentration propane, this method can register a precise amount of propane exposure to each SERS spectra collected from the nickel sample surface.

Through precise control of the volume of propane exposure, different stages of carbon deposition can be identified. The first stage is a quick growth of carbon signal in the first 20mL pulse, as shown in Figure 34(A). After the first few pulses, carbon deposition proceeds, but the growth rate slowed down. Continuous exposure to more hydrocarbon molecules shows linear increase of carbon G-band intensity as a function of amount of propane exposure, as displayed in Figure 34(B). The quick development of carbon peaks during the first 20mL of exposure suggest a quick initiation of carbon deposition on the nickel surface. However, during the first pulse, nickel regions active for carbon deposition are covered, and further deposition needs to overcome higher energy barrier and thus slowed down.

In contrast to the SERS analysis, ordinary Raman spectroscopy study of carbon deposition on the same type of nickel foil showed no signal until 1000mL of propane was introduced, but the signal quickly developed subsequently, indicating a self-catalyzed growth of bulk carbon, such as encapsulation, whisker or filaments. The formation of bulk phase carbon is characteristic of late stage carbon deposition when severe structural and functional impairment has already occurred, and therefore cannot be used as a good characterization of the intrinsic property of material surface. SERS, in contrast, provides high sensitivity towards the incipient stage of carbon deposition, and is useful for the characterization of the intrinsic catalysis properties of anode surfaces.

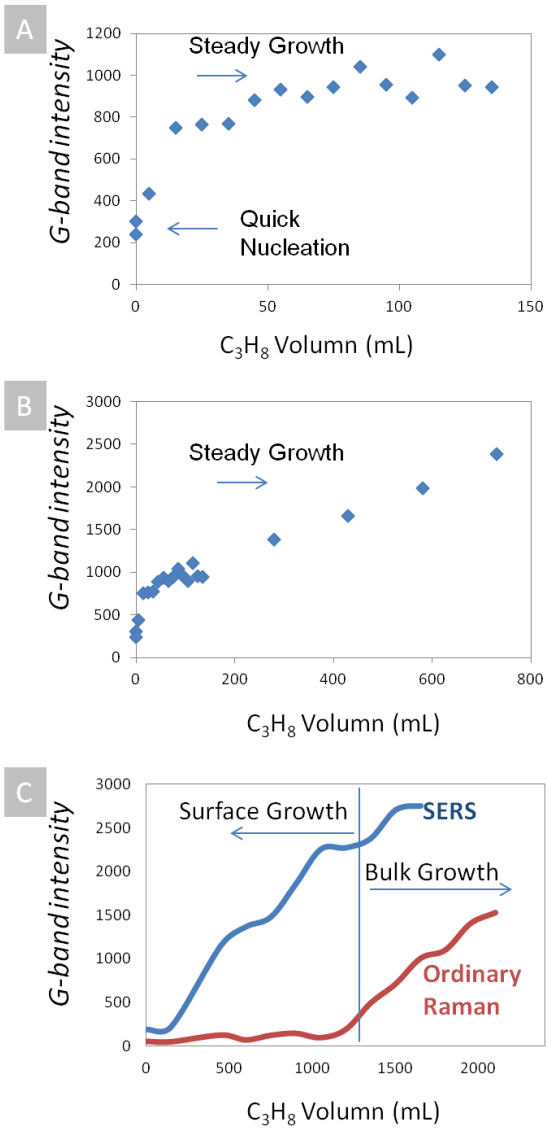

Figure 34: *In situ* SERS analysis of carbon deposition at different stages.
(A) SERS intensity of carbon G-band intensity as a function of propane exposure as carbon deposition initiates, each pulse contains 10mL propane. (B) SERS intensity of carbon G-band intensity as a function of propane exposure as the carbon steadily deposit, each pulse contains 150mL propane. (C) SERS and ordinary Raman analysis of carbon G-band intensity with continuous flow of propane.

4.2. Coking Resistance from CeO_2 Modification

The sputtered Ag nanoparticles were also used to detect a thin film coating of catalysts on electrode surfaces that enhanced the performance and stability of the electrode materials.

Displayed in Figure 35(A, B) are the SEM images of nickel foil samples before and after the electrodeposition of a thin layer of CeO_2. No significant microstructure difference can be observed from these SEM images, due to the small amount of CeO_2. The normal Raman of the CeO_2 modified nickel foil did not show any features of CeO_2 either. However, after SERS activation, the peaks associated with the CeO_2 appeared. As shown in Figure 35(C), the 460 cm^{-1} and 600 cm^{-1} peak can be assigned to the F_{2g} and A_{1g} mode of CeO_2, respectively,[116] while the 570 cm^{-1} peak indicates the presence of oxygen vacancies.[60, 61] This thin layer of CeO_2 acted as a very effective surface modifier to resist carbon deposition. As is evidenced from the Raman spectra and SEM images in Figure 35(D, E, F), when the blank nickel sample and the CeO_2 modified nickel were exposed to C_3H_8 containing gas for the same amount of time, the blank nickel foil developed large patches of coke while the CeO_2 foil remained clean.

The coking resistance of cerium oxide was further investigated with *in situ* SERS. To create samples suitable for evaluation of the intrinsic property of modified nickel surface, gadolinium doped ceria (GDC) was sputtered onto a nickel foil. GDC target was sputtered under Ar with pressure of 2.2 x 10^{-2} mBar, with power of 20W for a duration of 3 mins. Discontinuous but uniform deposition of GDC nanoparticles was expected. Following the deposition, $Ag@SiO_2$ nanoprobes were deposited by spin coating. The SERS activated sample was placed in the environmental chamber, and heated to 450^0C under vacuum (with small amount of air leakage), to let all organic residue decompose. Afterwards, 4% H_2 was introduced to the chamber to reduce the nickel surface.

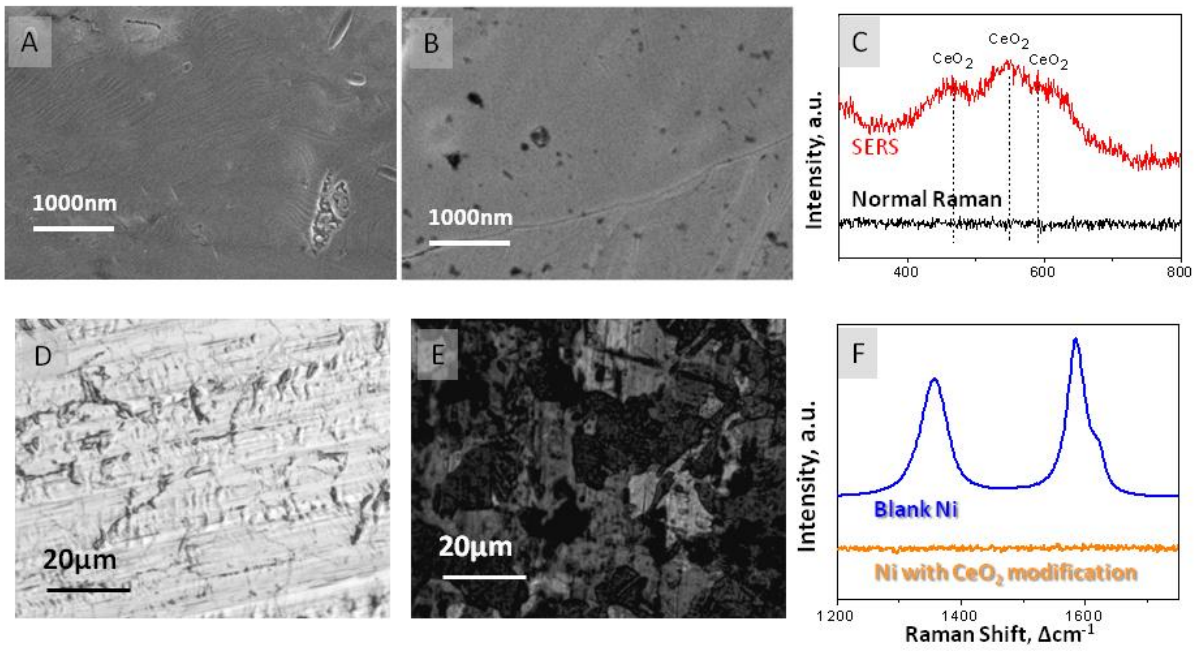

Figure 35: Detection of CeO_2 surface modification through Raman spectroscopy and SERS.
(A, B) The SEM images of the nickel foil with and without CeO_2 coating. (C) Normal Raman and SERS spectra from the nickel foil with electrochemical CeO_2 coating. (D, E) The optical microscope images of the nickel foil with and without CeO_2 coating after coking test. (F) The Raman spectra from nickel foils with and without CeO_2 modification after coking test. (C) is reproduced from reference [87].

Propane exposure was carried out with short pulses of 50% propane, delivering 20mL of propane during each pulse of 10-15 secs. Figure 36 presents the SERS response of GDC modified Ni upon the exposure to small amount of propane. As is shown in Figure 36(A), the initial round of dry 50% propane (2% H_2, 48% Ar) exposure yielded much less carbon deposition compared to the blank nickel sample. In particular, the rapid adsorption of carbon at the first 20mL of propane exposure was inhibited in the presence of 3nm GDC on Ni surface.

After the initial round of propane exposure, the GDC modified nickel sample was regenerated by letting it dry in air to oxidize the deposited carbon. After this regeneration process, the following rounds of propane exposure showed drastically different SERS response from the

GDC modified nickel sample. As is shown in Figure 36(B), exposure to dry 50% C_3H_8 (2% H_2 and 48% Ar) yielded quick and significant carbon deposition, showing a rapid carbon initiation that was absent at the initial round, suggesting that the surface of Ni sample has changed during the initial round of coking and regeneration by air. Most likely, the enclosure provided by GDC coating has been damaged due to the surface restructure in the re-oxidation process. On the other hand, after regeneration by air, the subsequent exposure to wet 50% C_3H_8 (2% H_2, 3% H_2O and 45% Ar) showed very little coking tendency at early stage, suggesting that even the re-structured surface showed resistance to carbon deposition when water vapor was introduced along with propane. Since the steam-to-carbon ratio (S/C=0.06) of the gas mixture is much less than the stoichiometric value for complete reforming of propane (S/C=1), this observation suggest the presence of a small amount of water inhibit the deposition of carbon on nickel surface in the incipient stage.

The change of coking tendency after the initial round of coking-regeneration process was also illustrated by the capability of 4% wet H_2 (3% H_2O, 93% Ar) to remove carbon deposition. As displayed in Figure 37 (A), following the initial round of propane exposure (before the regeneration by air), the exposure to 4% wet H_2 can quickly remove a significant part of carbon deposition, indicating that some carbon deposition on the GDC modified nickel surface are loosely bonded, and can be removed easily. However, after the Round 2 of carbon deposition, exposure to wet 4% H_2 showed no effect to remove carbon, as displayed in Figure 37 (B). While it was suspected that the structure of carbon could be different during these two rounds of propane exposure, the analysis of D/G ratio showed no evidence of the presence of different allotropes, as is shown in Figure 37 (C, D). These results suggest that the initial sample surface has not only less coking tendency, but also better capability to remove the carbon that deposited

on it. While the deposited carbon share the same structure, the easiness to remove carbon by exposure to 4% H_2 might be originated from the uniform distribution of GDC modification, which may be significantly changed during the regeneration process.

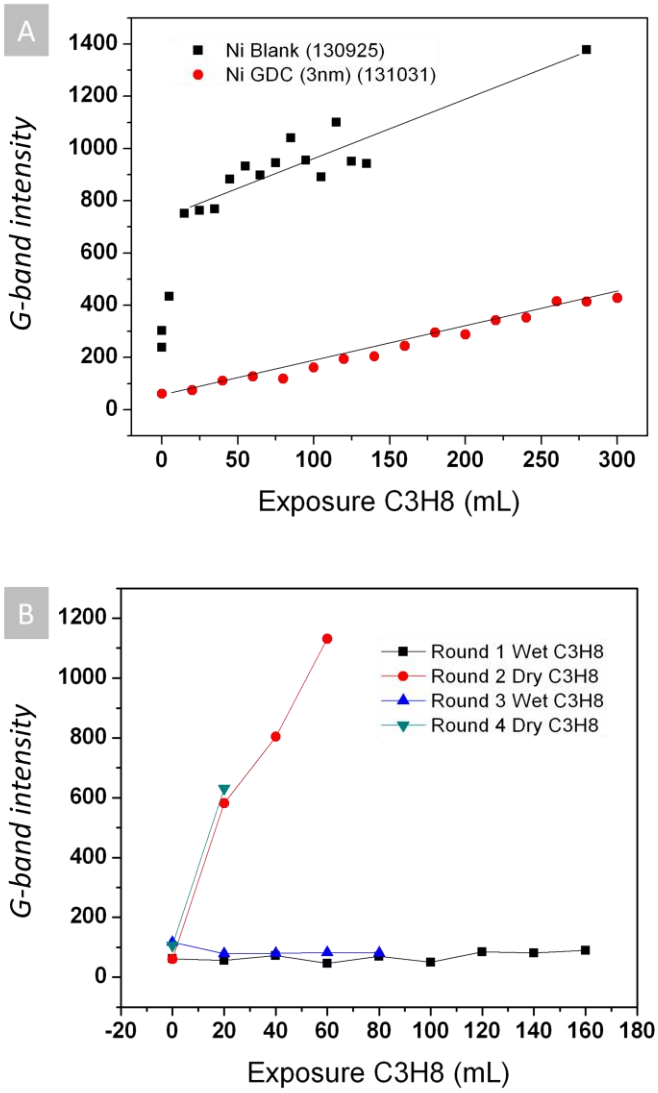

Figure 36: Impact of GDC modification and oxygen regeneration on the initiation of coking.
(A) Intensity of carbon G-band as a function of propane exposure volume, collected from blank Ni foil and GDC modified Ni foil, respectively, during the initial round of exposure. (B) Intensity of carbon G-band upon exposure to dry/wet propane collected from GDC modified Ni foil after the initial round. After each round of propane exposure, the sample was regenerated by air.

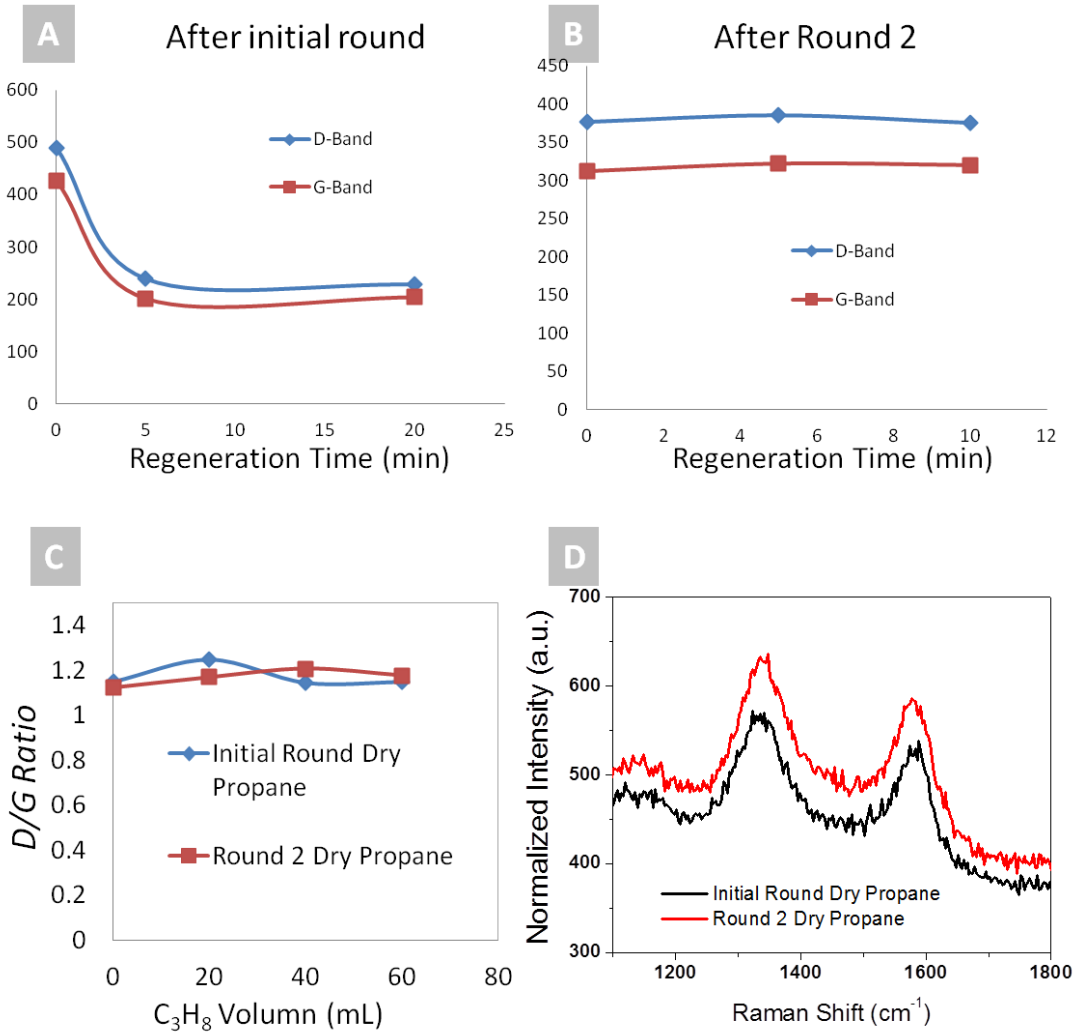

Figure 37: Impact of surface regeneration on the capability of coking removal.
Following the *in situ* coking analysis presented in Figure 36. (A) Surface regeneration by 4% wet H_2 after the initial round. (B) Surface regeneration by 4% wet H_2 after Round 2. (C) The D/G ratio of deposited carbon during the initial round and round 2. (D) The normalized SERS spectra of the GDC modified nickel surface after initial round and round 2.

The coking resistance provided by either CeO_2 or GDC roots in its superior catalytic activity towards reforming of hydrocarbon fuels. To identify the active surface species, *in situ* SERS was employed to probe the surface of CeO_2 upon exposure to different gas atmospheres.

CeO_2 powders were mixed with $Ag@SiO_2$ nanoparticles and drop-coated onto a silicon substrate which was subsequently heated to 450 °C in a Raman chamber for *in situ* study. Raman spectra were collected while the SERS enabled CeO_2 powders were exposed to air and 4% H_2 alternatively. For ordinary Raman spectroscopy on CeO_2, a band at 465 cm^{-1} is characteristic of the F_{2g} mode.[60, 65] On the SERS activated CeO_2 powders (Figure 38A), a peak at around 540 cm^{-1} was present when the sample was exposed to argon with 4% H_2, and disappeared when exposed to air. This peak can be associated with the oxygen vacancies on the CeO_2 surface, which emerges under a reducing atmosphere and diminishes when exposed to an oxidizing gas.[60, 64] Another notable feature is the weak hump at 800–1000 cm^{-1} which appears only when the sample is exposed to air. The Raman shift of this hump is consistent with the oxygen adsorbed on CeO_2 and Au electrode surfaces. [65, 117] Control groups were tested with the same procedure, as displayed in Figure 38(B, C). The pure $Ag@SiO_2$ nanoparticles showed no prominent features during the redox cycling; on the blank CeO_2 powders, only F_{2g} mode is observable while no oxygen vacancy or adsorbed oxygen peak can be detected.

SEM and TEM micrographs are taken after the high temperature SERS analysis to validate the thermal robustness of the SERS probes. Shown in Figure 38(D) is the SEM image of $Ag@SiO_2$ NPs mixed with CeO_2 powders after the red-ox testings at 450°C. The $Ag@SiO_2$ NPs retained the same particle size and geometry. TEM analysis of the $Ag@SiO_2$ NPs after high temperature treatments in both air and argon with 4% H_2 also confirmed the stability of the core-shell microstructure, as seen in Figure 38(E, F). The core-shell microstructure of the $Ag@SiO_2$ nanoparticles remained unchanged over the prolonged testing period.

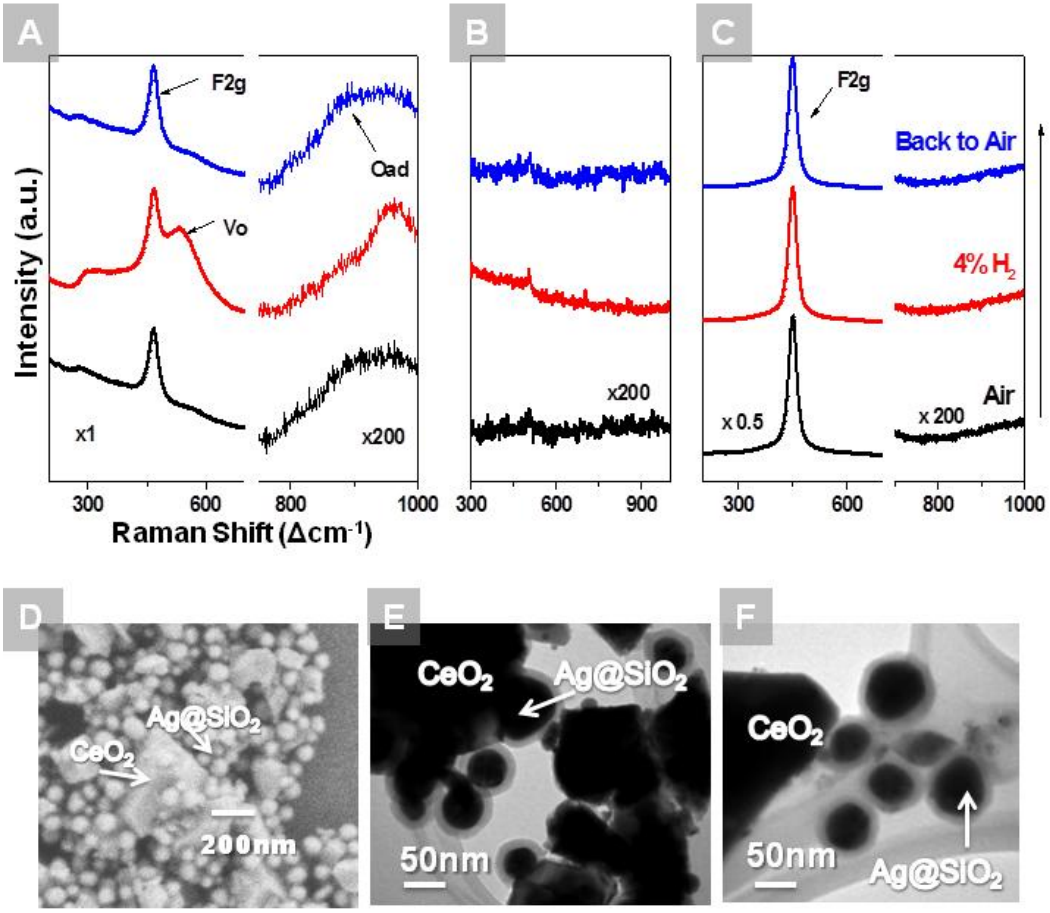

Figure 38: *In situ* SERS study of the surface functional groups on CeO_2 powders.
(A, B,C) typical Raman spectra taken at 450 °C under air, 4% H_2, and back to air on the sample of (A) CeO_2 powders mixed with $Ag@SiO_2$ NPs, (B) Pure $Ag@SiO_2$ NPs, and (C) Blank CeO_2 powders. All spectra were taken with a 633 nm laser at 10 mW with the an acquisition time of 10s. (D) SEM image of the CeO_2 powders mixed with $Ag@SiO_2$ after the redox test. (E) TEM images of the $Ag@SiO_2$ NPs loaded on CeO_2 powders after annealing at 450°C for 1 hr in air and (F) in 4% H_2.

Observation of the accumulation and depletion of oxygen vacancies on CeO_2 surface at high temperatures revealed the role of CeO_2 in the SOFC electrodes. As a catalyst, CeO_2 is often used as an electrode modifier to help resist carbon deposition on the nickel-based anode and promote oxygen reduction on the cathode. It has been found that CeO_2 stores and releases oxygen under oxidizing and reducing conditions, respectively, leading to the unique catalytic activity. The cycling of oxygen vacancy band in response to the change of gas atmosphere

supports this hypothesis. More importantly, this suggests that the surface species, which were undetectable previously under *in situ* conditions using ordinary Raman spectroscopy, can now be identified using SERS – a powerful tool for *in situ* study of materials for fuel cells and catalysis.

4.3. Coking on Ni-YSZ Interface

The triple phase boundary of the SOFC anodes is a complicated electrocatalytic interface that influences the performance and stability of SOFC system. On a nickel-based anode, the performance depends sensitively on the accessibility of the TPBs by the reactants involved in fuel oxidation. Coking on the TPB region could block the accessibility of reaction species, and results in significant degradation of anode performance. On the other hand, TPBs are also "hot spots" for the electrochemical oxidation of fuel molecules and deposited carbon, and thus have certain degree of self-cleaning capability. [57] In addition, the interface between Ni and electrolyte materials may possess unique catalytic properties, since the electrolyte and nickel could act as synergetic couples for fuel oxidation. [118-121]

Operando SERS analysis of carbon deposition on patterned Ni-YSZ interface explores the key factors influencing carbon deposition and removal. The patterned electrode was fabricated by the embedded-mesh method. After polishing, nickel strands of ~100 um width showed clear interface with the YSZ electrolyte. After application of $Ag@SiO_2$ nanoparticles, the sample pellet was attached to the metal base of the environmental chamber with silver paste, which also serves as counter electrode. A gold wire was attached to the nickel mesh with silver paste for current collection. Before the testing, the sample was first annealed in vacuum (with air leakage) at 450^0C to remove organic residue and to cure the silver paste. Afterwards, the

chamber was purged with 4% H_2 to reduce the nickel surface. Carbon deposition was introduced by a continuous flow of 50% C_3H_8 (2% H_2 and 48% Ar). Carbon elimination was experimented by exposure to wet 4% H_2 (3% H_2O and 93% Ar), and application of an anodic potential to the Ni-YSZ electrode during the exposure to 50% C_3H_8. SERS spectra were collected on different locations across the Ni-YSZ interface to reveal the impact of carbon deposition on the TPB, and the synergetic effect on the interface.

With the presence of SERS probes, the sensitivity towards carbon is significantly enhanced, allowing for the mapping of carbon deposition profile on patterned Ni-YSZ interface *in situ*. As shown in Figure 39, after exposure to dry 50% propane, carbon deposition manifested only on the nickel surface. As the laser inspection spot moved from Ni surface to YSZ surface, the peak intensities of carbon bands first increased, showing a maximum near the Ni-YSZ interface, and then diminished on the YSZ surface.

Exposure to 4% wet H_2 effectively removed carbon deposition across the Ni surface. In particular, coking removal seems to be more effective in the location near the Ni-YSZ interface. While the initial higher concentration of carbon on the Ni-YSZ interface can be ascribed to the higher density of defects along the edge of Ni electrode, the enhanced capability to remove carbon on the Ni-YSZ interface may be due to the synergetic effect. According to the previous DFT calculation of water adsorption energy on different materials, YSZ showed higher affinity to water than Ni. [6 12] Since water is a critical intermediate for carbon removal, the enhanced coking removal on the Ni-YSZ interface might be a result of enhanced adsorption.

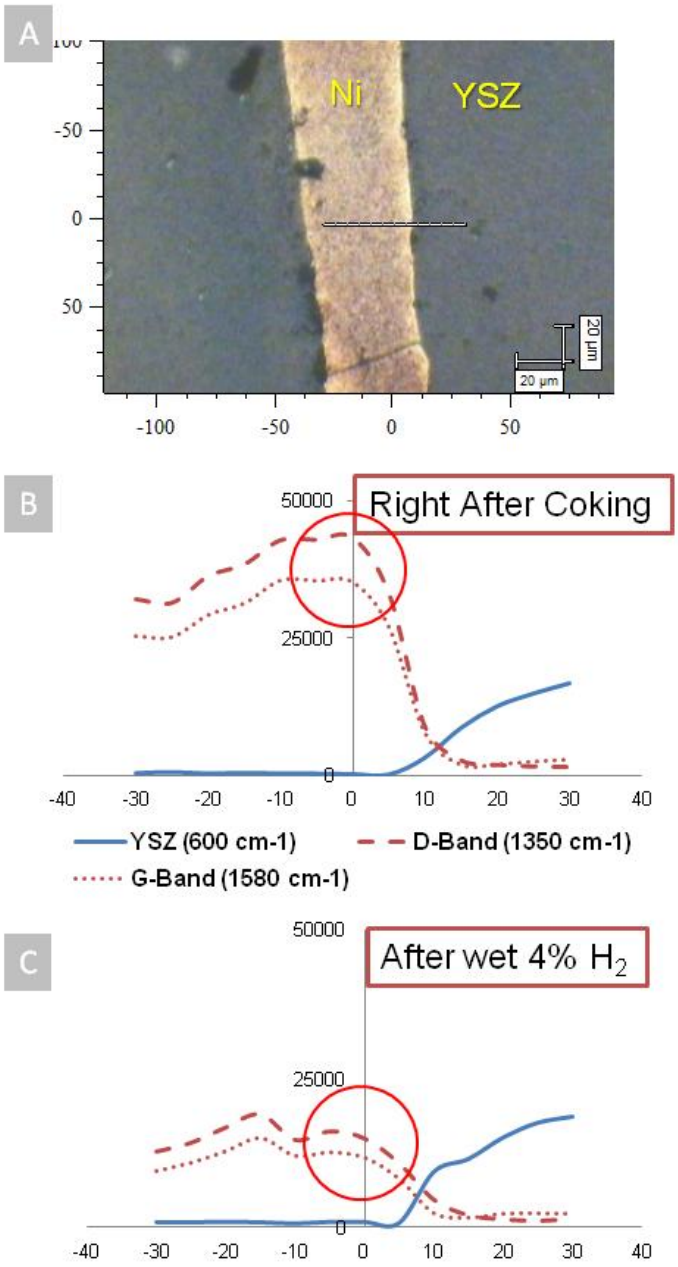

Figure 39: *In situ* SERS analysis of carbon deposition across Ni-YSZ interface.
(A) Optical micrograph of Ni-YSZ interface and linescan locations. (B) Peak intensity of key Raman bands collected across Ni-YSZ interface, from locations indicated by the line in (A), after continuous flow of 50% propane (2% H_2, 48% Ar) for 30 mins, equivalent to 1500 mL of propane. (C) Raman peak intensity collected across Ni-YSZ interface after regeneration with wet 4% H_2 (3% H_2O, 93% Ar) for 30 mins.

To reveal the electrochemical carbon removal on Ni-YSZ interface, the influence of anodic bias on the distribution of carbon are also investigated by *operando* SERS, as shown in Figure 40. Before the initial exposure to propane, all regions exhibit a low level of adventitious carbon. When exposed to 50% C_3H_8 for 30 mins, either Ni surface or YSZ surface showed no significant coking. Interestingly, on the Ni-YSZ interface (Figure 40**E**), many strong Raman bands manifested between 1200 cm^{-1} and 1700 cm^{-1}, suggesting the formation of ethylene (C_2H_4), propylene (C_3H_6), hexane (C_6H_{14}) and dimethyl butylene (C_6H_{12}) (cf. Table 5). After applying anodic bias of 0V/0.1V/0.2V/0.5V/1V, each for 15mins, to the Ni-YSZ interface, while keeping chamber under 50% propane, the Raman peaks suggesting the formation of multiple hydrocarbons disappeared, while the carbon D-band and G-band remained (Figure 40**H).**

The formation of hydrocarbon intermediates were scrutinized through time resolved *in situ* SERS at the Ni-YSZ interface, as illustrated in Figure 41. As the 50% propane (2% H_2 and 48% Ar) was introduced into the chamber, the carbon D-band and G-band increased gradually, along with the peaks related to hydrocarbons. The intensities of the carbon D-band (1350 cm^{-1}), G-band (1580 cm^{-1}), and a band that typically belongs to ethylene, hexane and dimethyl-butene (1450 cm^{-1}, cf. Table 5) were monitored over time. As the coking proceeds, the concentrations of all three species increased over time. Subsequently. anodic biases (0.1V, 0.2V, 0.5V and 1V) were then applied to the nickel mesh electrode for 15 mins at each potential while 50% C_3H_8 was maintained in the chamber. As the polarization was increased, the carbon D-band and G-band gradually decreased and the peaks related to hydrocarbons diminished completely. This behavior indicated that under anodic bias, the hydrocarbon accumulated on the Ni-YSZ interface readily react with the oxygen pumped from the YSZ lattice. However, the carbon deposition, once

formed, has less reactivity with the electrochemical pumped oxygen species. While the features related to deposited carbon, remains significant.

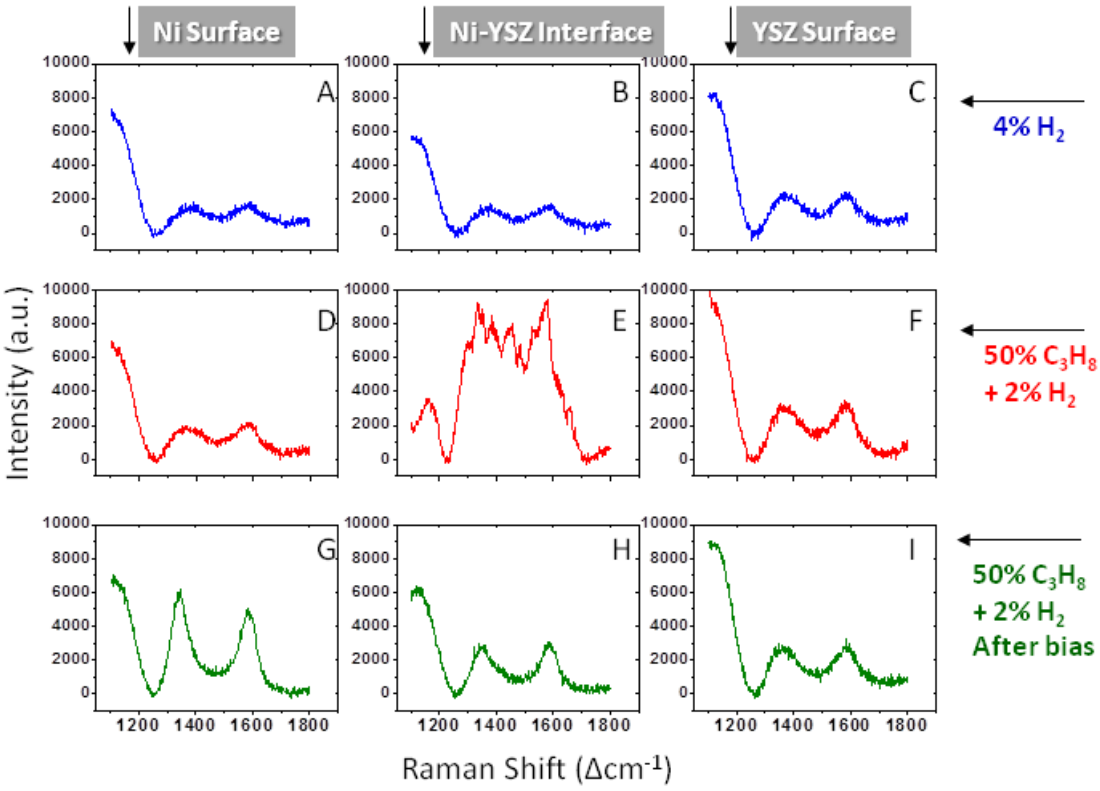

Figure 40: SERS analysis of the coking process on Ni-YSZ interface.
(A, B, C) Spectral features collected from Ni surface, Ni-YSZ interface and YSZ surface under 4% H_2 (96% Ar), respectively. (D, E, F) After exposure to 50% C_3H_8 (2% H_2, 48% Ar) for 30 mins. (G, H, I) After applying a series of anodic potentials (OCV, 0.1V, 0.2V, 0.5V and 1V), each for 15 mins in the presence of 50% C_3H_8.

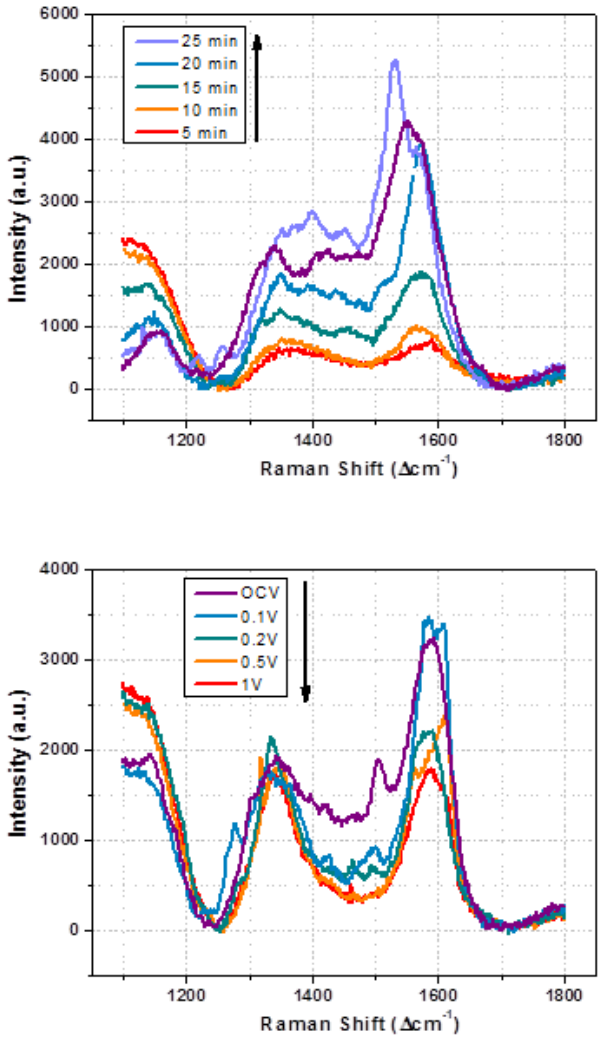

Figure 41: Time-resolved *operando* SERS analysis of carbon deposition and electrochemical removal on Ni-YSZ interface.

(A) Spectra acquired as a function of time under 50% C_3H_8, 2% H_2 and 48% Ar. (B) Spectra acquired under 50% C_3H_8, 2% H_2 and 48% Ar with anodic biases (OCV, 0.1V, 0.2V, 0.5V and 1V) applied consecutively, showing the carbon removal process. Arrows beside the legend indicate the order of spectra acquisition. Each spectrum reflects an acquisition time of 50s. The band intensity was computed by integrating the Raman spectral line over a 20 cm^{-1}bandwidth.

Table 5: Identification of intermediate species of carbon deposition on Ni-YSZ interface.

Observed (Fig. 3, 4)	***Raman bands reported in literature***					
	Ethylene (C_2H_4)[122]	Propylene (C_3H_6) [123]	n-Hexane (C_6H_{14}) [124]	2,3-Dimethyl-1-butene (C_6H_{12}) [124]	3,3-Dimethyl-1-butene (C_6H_{12}) [124]	2-Methylpent-2-ene (C_6H_{12}) [125]
1160[b]	1128		1142	1162		1167
				1208	1209*	1203
1277[b]					1272*	1263
1300[b]			1306*****	1305*	1311*	1305*
1435[a]	1340	1327/1337				
1350[c]		1360				1353*
1386[b]					1390	1382*
1400[b]				1400*	1424	1439*
1450[a,b]	1456		1452*****	1450*	1456*	1455*
1482[b]						1478
1500[d]						
1526[b]					1549	1525
				1550		
1580[c]		1590		1595	1592	
		1622				
1654[b]				1652	1648	1677

Comparison of the observed Raman lines to those characteristic of hydrocarbon compounds within the range between 1100 cm^{-1} and 1700 cm^{-1}

Underlined: Raman bands matching with the observed spectra

* Raman bands with strong intensity

[a] Peak associated with lower order hydrocarbons.

[b] Peak associated to higher order hydrocarbons

[c] Peak associated with carbon D-band and G-band, overlapping some hydrocarbon bands.

[d] The most intensive Raman modes of ethane, propane and butanes [126, 127] are not in this wavenumber range, although the overtone of the 2900-3000 cm^{-1} bands could appear at around 1500 cm^{-1}. [128]

The unique spectral features observed on Ni-YSZ interface suggests that Ni and YSZ play synergetic roles in the reforming of hydrocarbons. To explain the unique function of Ni-YSZ interface, a possible reaction mechanism is presented in Figure 42. Since the Ni is an excellent catalyst for breaking the first C-H bond of hydrocarbons, on the Ni surface, the $-C_3H_7$ (propyl) moities are expected. [129] On nickel surface, propyl moities decompose into monatmoic carbons, and subsequently form carbon patches. [43, 130, 131] Near the Ni-YSZ interface, due to the presence of surface oxygen species from YSZ, the propyl species could be converted to propylene and ethylene through oxidative dehydrogenation, [130, 132, 133] or hexane and dimethyl butane through oxidative coupling.[130, 132, 133] When anodic bias was imposed, large amount of lattice oxygen was pumped to the surface, and the hydrocarbons that accumulated on the Ni-YSZ interface were quickly oxidized to CO and H_2O. On the other hand, the coking patches that had already formed at the Ni-YSZ interface and on the Ni surface could not be easily removed due to the limited reactivity. [43] The precise formula and conversion mechanism of the hydrocarbons accumulated on Ni-YSZ interface cannot be ascertained in this study, due to the complexity of hydrocarbon chemistry.

The location-sensitive, time-resolved, and signal-enhanced Raman spectroscopy technique allowed for the capture of intermediate species specific to propane reformation at Ni-YSZ interface. This interface promotes the formation of a variety of hydrocarbons that may be derived from the oxidative dehydrogenation and coupling of propane, due to the synergetic effect of Ni and YSZ. The hydrocarbons formed on the interface readily react with the lattice oxygen pumped to the surface under anodic bias. In contrast, the carbon formed in either the Ni-YSZ interface or the interior of Ni surface showed less reactivity with the oxygen generated by electrochemical bias.

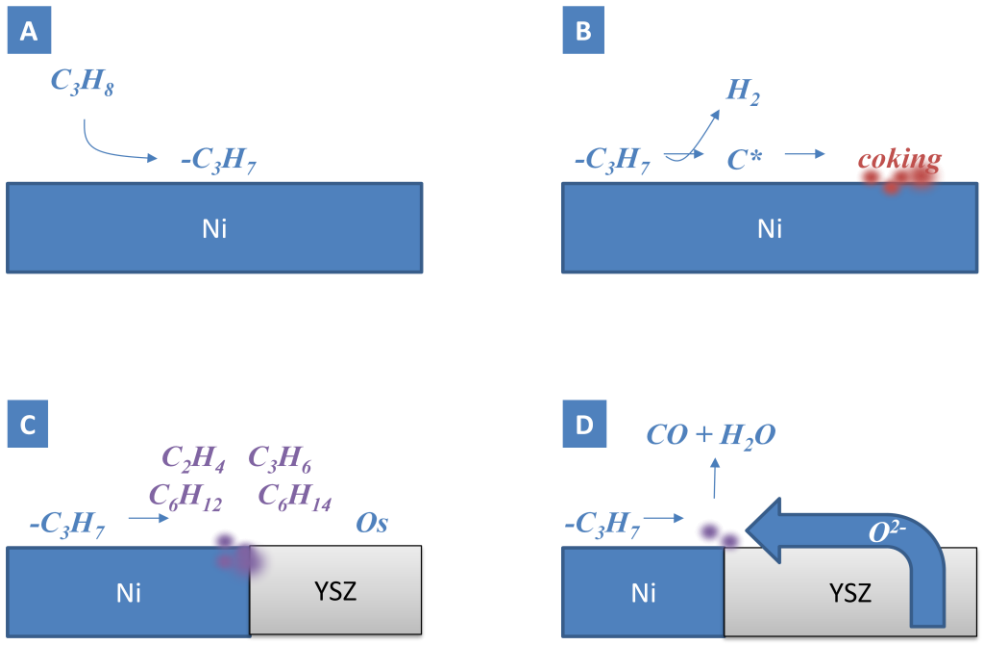

Figure 42: Proposed mechanism of carbon deposition and electrochemical removal on Ni-YSZ interface. (A) Chemical adsorption (activation) of propane on the Ni surface forming propyl moities. (B) Decomposition of propyl moities and formation of ”coke”. (C) Oxidative dehydrogenation and coupling of propyl moities that formed a variety of hydrocarbons. (D) Removal of hydrocarbon species under anodic bias.

4.4. Chapter Conclusions

Surface enhanced Raman spectroscopy technology has been applied to probing and mapping of carbon deposition on nickel-based SOFC anode. The enhanced sensitivity allows for the detection of coking at its initiation stage. On nickel foil exposed to small amounts of propane, regions of different degree of carbon deposition developed, correlating to different morphological features and different Raman/SERS peak intensities. The initiation of coking occurs at the first 20 mL propane exposure, and continuous exposure built up the carbon deposition gradually.

The initiation of coking can be inhibited through surface deposition of CeO_2 or GDC. However, after the sample surface was regenerated with air exposure, the coking resistance at early stage was compromised. The functionality of CeO_2 is related to its active oxygen storage capability, and *in situ* SERS identified the evolution of surface oxygen vacancies upon the exposure to red-ox cycles.

The Ni-YSZ interface was found to catalyze hydrocarbon reforming, resulting in the accumulation of multiple hydrocarbon molecules. Upon the application of anodic bias, the hydrocarbon species can be effectively removed. Raman analysis of the patterned Ni-YSZ anode also showed the distribution of carbon deposition across the triple phase boundary. The effect of coking removal, either by exposure to wet 4% H_2 or application of anodic bias, are more prominent on the Ni-YSZ interface than on the center of Ni electrode.

CHAPTER 5: COKING RESISTANCE OF BA-CONTAINING CATALYSTS

Nickel activates the hydrocarbon fuels for oxidation. Hydrocarbon molecules adsorb on Ni surfaces and undergo a series of dehydrogenation and C-C bond cleavage steps,[41, 42] releasing H_2 and forming surface carbonaceous groups (e.g., $–C_3H_7$, $-C_2H_5$, $-CH_3$, and adsorbed atomic carbon C_{ad}) on nickel surface. The adsorbed carbonaceous groups could be detrimental to the anode, if they coalesce and form surface carbon patches, filaments or whiskers. However, these carbonaceous groups can also react with the adsorbed H_2O, CO_2 and O_2 to escape from the nickel surface without causing carbon deposition. Fine-tuning of the surface properties of the nickel-based anode and catalysts to promote the removal of the adsorbed carbonaceous groups before they form large patches or filaments is one of the key approaches to minimize coking. [131, 134, 135]

Several Ba containing oxides, including BaO, $BaZr_{1-x}Y_xO_{3-d}$ (BZY), and $BaZr_{0.1}Ce_{0.7}Y_{0.1}Yb_{0.1}O_{3-d}$ (BZCYYb), were recently found to provide superior coking resistance to nickel-based SOFC anodes.[6, 12, 52] The coking resistance of the BaO modified Ni surface was attributed to the dissociative adsorption of water, providing abundant -OH groups for removal of carbon atoms on nickel surface.[6] Earlier studies of reforming catalysts also showed that alkaline earth oxides (e.g., MgO, CaO, SrO, and BaO) have high tendency for water and CO_2 adsorption and hence promote reformation of carbonaceous species.[136-138] In addition, DFT simulation validated that the Ba-based perovskites are capable of dissociative adsorption of water, due to the low work function and high Fermi basicity of the BaO terminated crystal faces.[12, 120, 139]

The detailed mechanisms responsible for coking resistance of the catalysts-modified SOFC anode are still not well understood, due to our inability to directly probe the surface species and incipient phases relevant to the electrode processes under realistic operating conditions. In addition, the catalytic activity of the modified nickel anode relies critically on the distribution and morphology of functional heterogeneous interface, which is difficult to study using conventional surface analytical methods.[12, 120, 139]

In this chapter, electrostatic force microscopy (EFM) is utilized to characterize the morphology and distribution of carbon deposition on nickel surfaces with and without the presence of BaO modification after exposure to fuel cell operating conditions. Block-co-polymer patterning was used to create well defined features of BaO nanorings on nickel surface for coking tolerance. In addition, Raman spectroscopy was used to probe and map carbon deposition on BaO modified Ni surfaces, which was further validated using SEM to clarify the effect of surface modification.

To reveal the catalysis mechanism of different Ba containing catalysts, *in situ* Raman spectroscopy and SERS were used to identify phase transformation and surface group evolution on the surfaces of BaO, BZY, and BZCYYb and to monitor their interactions with various gas components. Time-resolved analyses of the surface functional groups (carbon, -OH and $-CO_3$) revealed the kinetics of the elemental steps of the catalytic carbon removal processes. Different mechanisms of coking resistance were proposed, and insight were gained to better design catalysts for direct hydrocarbon SOFC anodes.

5.1. Block Co-polymer Pattering of BaO-Ni Heterogeneous Interfaces

The BaO-Ni interfaces were created with a block co-polymer patterning technique. Figure 43 illustrates the fabrication and testing of block co-polymer patterned BaO features. First, PS-*b*-P2VP diblock copolymer was dissolved in o-xylene solvent and spin-coated onto the nickel substrates. In the polymer thin film, the hydrophilic P2VP phase formed micelles, due to its insolubility in o-xylene, and the micelles are orderly distributed over the substrate. The as-spun film was then immersed in ethanol, a solvent to which the P2VP phase shows affinity, so that the P2VP micelles can convert into ring shaped structures. Subsequently, aqueous precursor of barium (barium nitrate) is introduced, and the Ba cations are absorbed by the swollen P2VP phases. The final step of oxygen plasma removes the organic components and the barium precursors turned into ring shaped nano particles on the substrate. Subsequent firing at 800^0C turns the barium precursors into BaO. After all, the nickel substrates with and without BaO nanorings are both exposed to propane containing fuels at 500^0C. Raman mapping conducted after the coking test was used to evaluate the coking resistance of the substrates. SEM, AFM and EFM were employed to analyze the surface morphology and distribution of surface species.

The nickel substrates were prepared by cutting a 1mm thick Ni foil (Alfa Aesar) into 1cm by 1cm coupons, followed by polishing and argon plasma cleaning. The PS-b-P2VP block copolymer (Polymer Source, M_n^{PS} = 440 kg/mol, M_n^{P2VP} = 353 kg/mol, Mw/Mn = 1.19) was dissolved in O-xylene at the weight ratio of 0.5wt%, and spin coated onto the polished nickel coupons. The P2VP micelles that formed in O-xylene solvent were uniformly distributed in the PS matrix on the nickel substrate. After exposing the sample to ethanol fume for 24 hour, the P2VP micelles reconstructed into ring shape. A UV Ozone treatment was then utilized to enhance the hydrophilicity of the P2VP phase. When the aqueous solution of Barium Nitrate

(0.5wt%) was spin coated onto the sample, the barium cations preferably stay in the P2VP domains, which are highly hydrophilic. In the end, the sample was treated in oxygen plasma that removes all organic components and converts the barium nitrate into BaO. The derived BaO retains the position and ring shape of the P2VP phase.

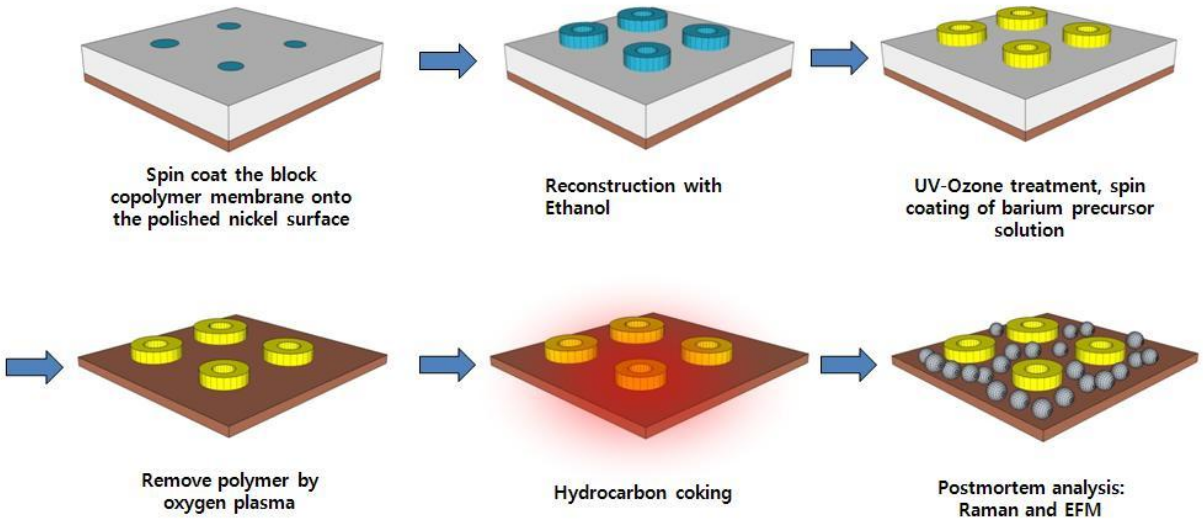

Figure 43: Schematic illustration for fabricating barium oxide nanoring arrays on a surface of Ni substrate via block copolymer patterning.

As shown in Figure 44(A, B), the nano rings appeared on Ni surface are clearly derived from the Ba(NO3)2 precursors. As displayed in Figure 44(C, D), the nanorings exhibited different surface potentials and mechanical rigidity.

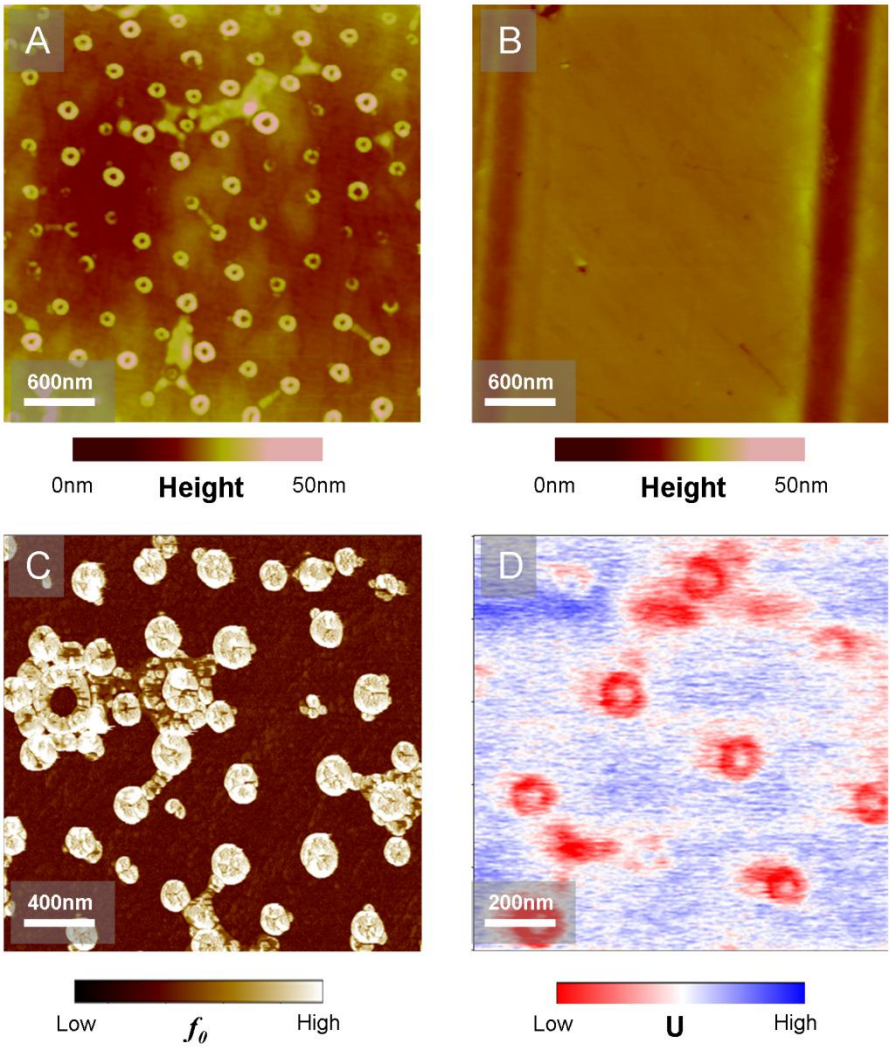

Figure 44: AFM characterization of the BaO modified nickel surface.
(A) AFM topography image of BaO nanorings loaded on polished nickel surface through block copolymers patterning. (B) AFM topography image of the control sample: polished nickel surface treated with the same protocol except the metal precursor loading. (C) Tip vibration frequency (f_0) mapping of the BaO nanorings on nickel surface and (D) Surface potential (U) mapping of the same sample. (C, D Courtesy of NT-MDT Co.)

5.2. EFM Study of the Distribution and Morphology of Carbon Deposition

Nano patterned BaO catalysts on nickel surface effectively resisted carbon deposition. To identify the carbon deposition at early stage, a blank nickel and a modified nickel foil were simultaneously exposed to a gas mixture of 15% C_3H_8, 3% H_2O, and 82% Ar at 550^0C for 3 mins. Confocal Raman mapping (using D-band peak intensity at 1350 cm^{-1}) showed that much less carbon deposition was observed on the BaO nanoparticles modified area than blank Ni without modification, as shown in Figure 45 (A, B, D, E), suggesting that the BaO modified nickel surfaces have enhanced tolerance to coking. The SEM analysis, revealed dark patches of only on the un-modified nickel surface after C_3H_8 exposure (Figure 45C), but not on the BaO modified nickel sample (Figure 45F).

Combined AFM and EFM study of the unmodified and BaO modified Ni foil after hydrocarbon exposure revealed the precise spatial distribution and morphology of carbon deposition. Figure 46(A,C) display the surface topographic images of the blank nickel sample and the BaO modified nickel sample after hydrocarbon exposure test, respectively. The EFM images were collected simultaneously on the same regions with a sample bias of +2V (Figure 46 B, D) and -1V (Figure 46C, E). The carbon deposited region and clean Ni surface were assigned according to their electrostatic response: when the sample is bias positively (+2V), carbon showed a stronger interaction with AFM tip, translated to brighter contrast in EFM image. Again, the phase angle contrast in the EFM images reversed when the sample was biased negatively (-1V). The electrostatic response of BaO in this sample seems hard to distinguish from nickel. However, the unique ring shape of the BaO nanoparticle assisted the assignment of their positions.

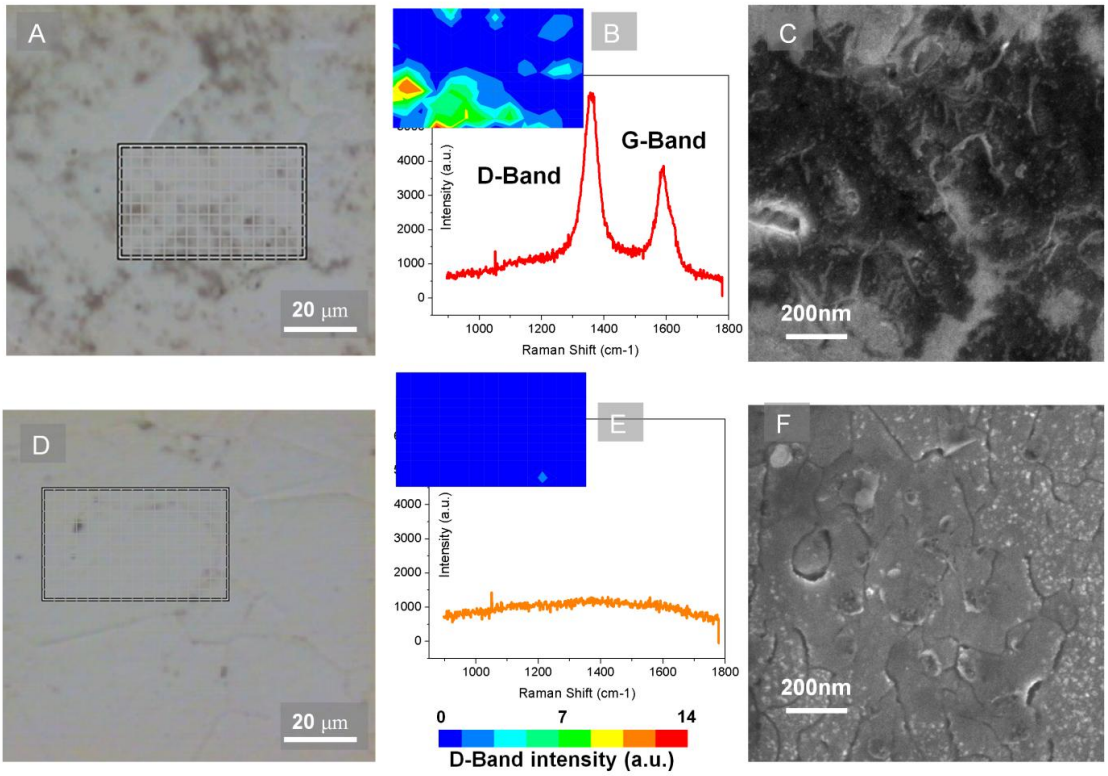

Figure 45: Raman and SEM analysis of coking propensity of blank and BaO modified Ni surfaces.
Optical microscope images (A, D), mapping of carbon D-band intensity from the checkered rigion (B, E insets), averaged Raman spectra (B, E) and SEM images (C, F) collected from the un-modified nickel sample (A,B, C) and BaO modified nickel surface (D, E, F). Both samples are exposed to C_3H_8 containing gas at 550ºC for 3 min.

The unmodified nickel foil (Figure 46B) showed large solid patches of carbon deposition. Sharp edges between the carbon patches and exposed nickel surface in the EFM image indicate that the carbon deposition formed continuous coverage over the nickel surface. In contrast, the BaO modified Ni surface (Figure 46D) developped carbon depositions in the form of loosely scattered nanodots. The EFM contrast due to these carbon nanodots does not possess sharp edges to the surrounding bare nickel regions, indicating lower carbon deposition amount and discontinuous coverage. Evidently, BaO prevented the formation of large patches of carbon deposition. As illustrated in the previous mechanistic studies, large patches of carbon deposition

are detrimental to the nickel-based reforming catalyst: it is difficult to be removed by H_2O or CO_2, and could also facilitate the dissolution of carbon into the nickel grain, leading to the wisker growth that further to the structural destruction. [43, 134] This observation provides an insight that the BaO resist coking through hindering the formation of continuous patch of carbon.

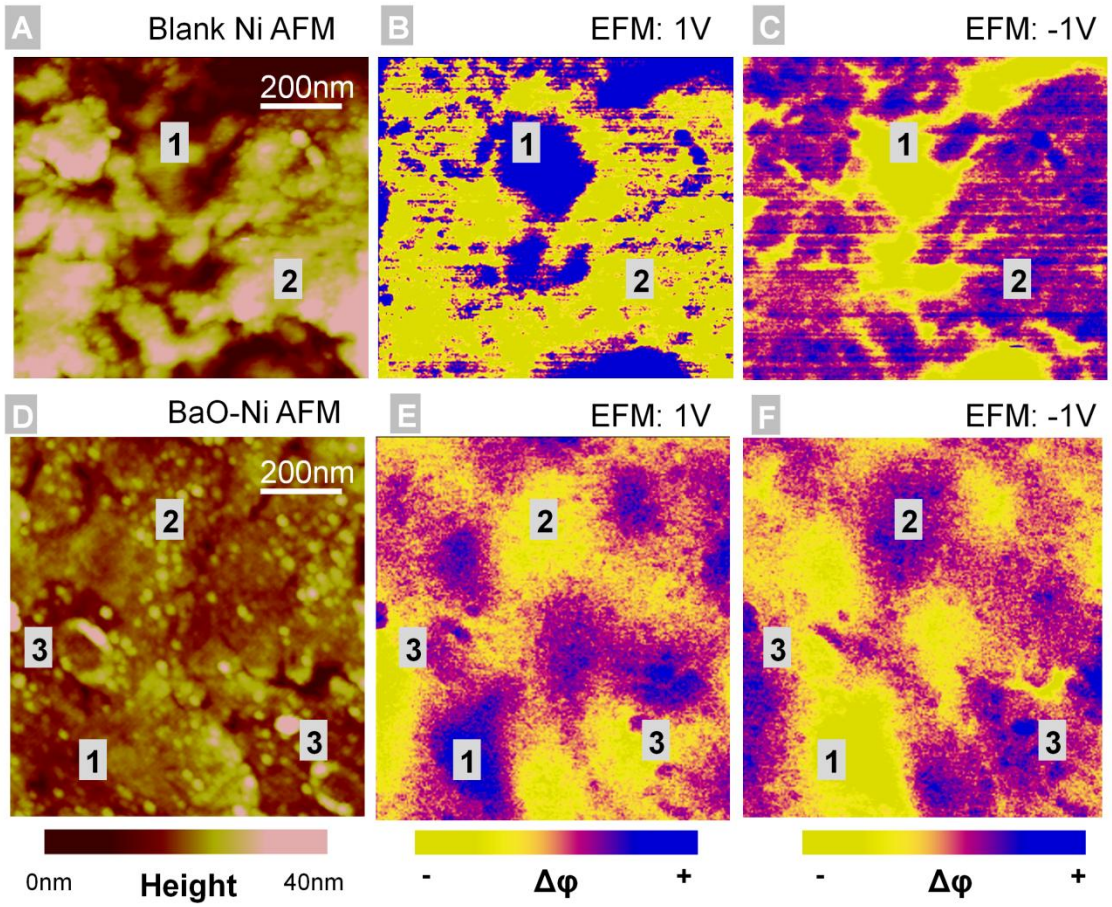

Figure 46: EFM analysis on the morphology and distribution of carbon deposition on nickel surface. Corresbonding AFM and EFM images of un-modifed nickel samples (A, B, C) and BaO modified nickel (D, E, F) after C_3H_8 exposure. (A, D): Surface topography images; (B, E) EFM images collected at sample bias of +2V; (C, F) EFM images collected at sample bias of -1V. Surface species assignment: (1) exposed nickel; (2) carbon deposition and (3) BaO modification.

While it can be clearly shown that BaO resists carbon deposition on nickel surface through the combination of SEM and Raman spectroscopy, EFM images directly registered the

spatial distribution of carbon deposition with respect to the positions of BaO nanoparticles. Previously, it was demonstrated that the BaO modification attracts water adsorption, and thus help to gasify the deposited carbon.[120, 140-143] Since the coking resistance effect is critically tied to the spillover of -OH group from BaO nanoparticles onto Ni surface, it was expected that each BaO nanoring should form a "screening range" that protects the adjacent nickel surface. However, as seen in Figure 46(C, D), the alleviated carbon deposition (nanodots) did not stay significant clearance from the BaO nanoparticles. It is possible that the "protection range" of BaO nanoparticle, due to the spilling-over effect of -OH group, is larger than the BaO separation (~300nm) used in this study, due to the long characteristic distance of -OH spillover. Future work will concentrate on previse engineering of the distribution of BaO nanoparticles to reveal the protection range of BaO on nickel surface.

5.3. *In Situ* Raman Spectroscopy

To reveal the catalysis mechanism of different Ba containing catalysts, *in situ* Raman spectroscopy and SERS were used to identify phase transformation and surface group evolution on the surfaces of BaO, BZY, and BZCYYb and to monitor their interactions with various gas components.

The testing apparatus for *in situ* Raman spectroscopy and SERS was introduced in Section 3.1. Ni powders (Alfa Aesar, 99.8%) and BaO powders (Alfa Aesar, 99.5%) were tested as purchased. BaO modified Ni were fabricated by mixing $BaCO_3$ (Alfa Aesar, 99.8%) and NiO (Fuel Cell Materials) with a weight ratio of 4:3, fired at 1200°C for 5 hours in air to decompose

all $BaCO_3$. Prior to the test, the BaO-NiO mixture was and reduced *in situ* at ~600°C in H_2 to produce BaO modified Ni.

To fabricate the $BaZr_{0.9}Y_{0.1}O_{3-d}$ (BZY) and $BaZr_{0.1}Ce_{0.7}Y_{0.1}Yb_{0.1}O_{3-d}$ (BZCYYb) powders, weighted mixture of $BaCO_3$, ZrO_2 (Aldrich, 99.9%), CeO_2 (Aldrich, 99.9%), Y_2O_3 (Aldrich, 99.99%), Yb_2O_3 (Aldrich, 99.9%), according to stoichiometry, were ball milled, pressed into a pellet and fired at 1125 ℃ for 12h. The fired powders were crushed and grinded with pestle and mortar, followed by another round of pressing-and-firing. These procedures were repeated until pure phase of BZY or BZCYYb was obtained.

During the *in situ* Raman analysis the powder samples were held by a silver foil secured on the hot stage within the Harrick environmental chamber, and the temperatures of the powder surface were calibrated with respect to the nominal temperatures. Gases (4% H_2, CO_2, air and C_3H_8, UHP Grade, Airgas) were mixed by mass flow controllers before being introduced into the chamber. Water was introduced by letting the gas flow through a water bubbler at room temperature.

To enable the BZCYYb samples for surface enhanced Raman spectroscopy study, $Ag@SiO_2$ (10mg/mL) was mixed with CeO_2 suspension (100g/mL) at 1:1 volume ratio and drop coated onto silicon wafer, which was placed on the hot zone of the environmental chamber for *in situ* study.

The acquisition of Raman spectra were designed for statistically reliable analysis. Static Raman spectra were obtained from 9 spots on the sample that formed a 3 by 3 square lattice, with the adjacent spots 20 um away from each other. I*n situ* time-resolved study was conducted by placing the laser spot on a same location, with the laser slightly off focus to cover a larger

area of about 5 um in diameter. Each spectrum covers the range of Raman shift from 150 cm^{-1} to 4000 cm^{-1}. An automated MATLAB program was used to remove the fluorescence background present in the Raman spectra, with a polynomial background fitting protocol.[144] In addition, spectra normalization was applied to correct the intensity attenuation due to the offset of laser focus and change of sample morphology during the exposure to reaction gases. The intensities of the cutting-off edge at ~170 cm^{-1} were used as the normalization factor. For a constant yield of Raman scattering, air-cooled Ar laser (CVI Melles Griot) emitted at 514 nm was used for excitation of Raman signal in this study with a total power of 15mW.

5.4. *In situ* Raman study of BaO Catalyst

BaO modified Ni powders showed excellent coking resistance, as demonstrated by an *in situ* time-resolved Raman analysis. Figure 47 compares the spectral features of plain nickel powders and BaO modified nickel exposed to wet propane at ~450°C. On the Raman spectra collected from the Ni powder sample (Figure 47A), the spectral features of carbon (1350 cm^{-1} and 1580 cm^{-1}, for carbon D-band and G-band, respectively) appeared quickly. In contrast, on the spectra collected from the sample consisted of a mixture of Ni powders and BaO (Figure 47B, C), almost no carbon deposition can be observed. Instead, a strong Raman band at 1060 cm^{-1} developed on the BaO-Ni composite upon propane exposure, suggesting the formation of surface carbonates. Figure 47(D) compares the spectra collected from blank and modified Ni powders, showing stark contrast in tendency of carbon deposition. After ~4 hour exposure to wet propane, carbon deposition eventually appeared on BaO modified Ni, possibly due to the high temperature pyrolysis of propane. While the coking resistance of BaO modification is shown promising, the

formation of surface carbonate groups seems to be related to the capability of coking resistance, which triggered further investigation.

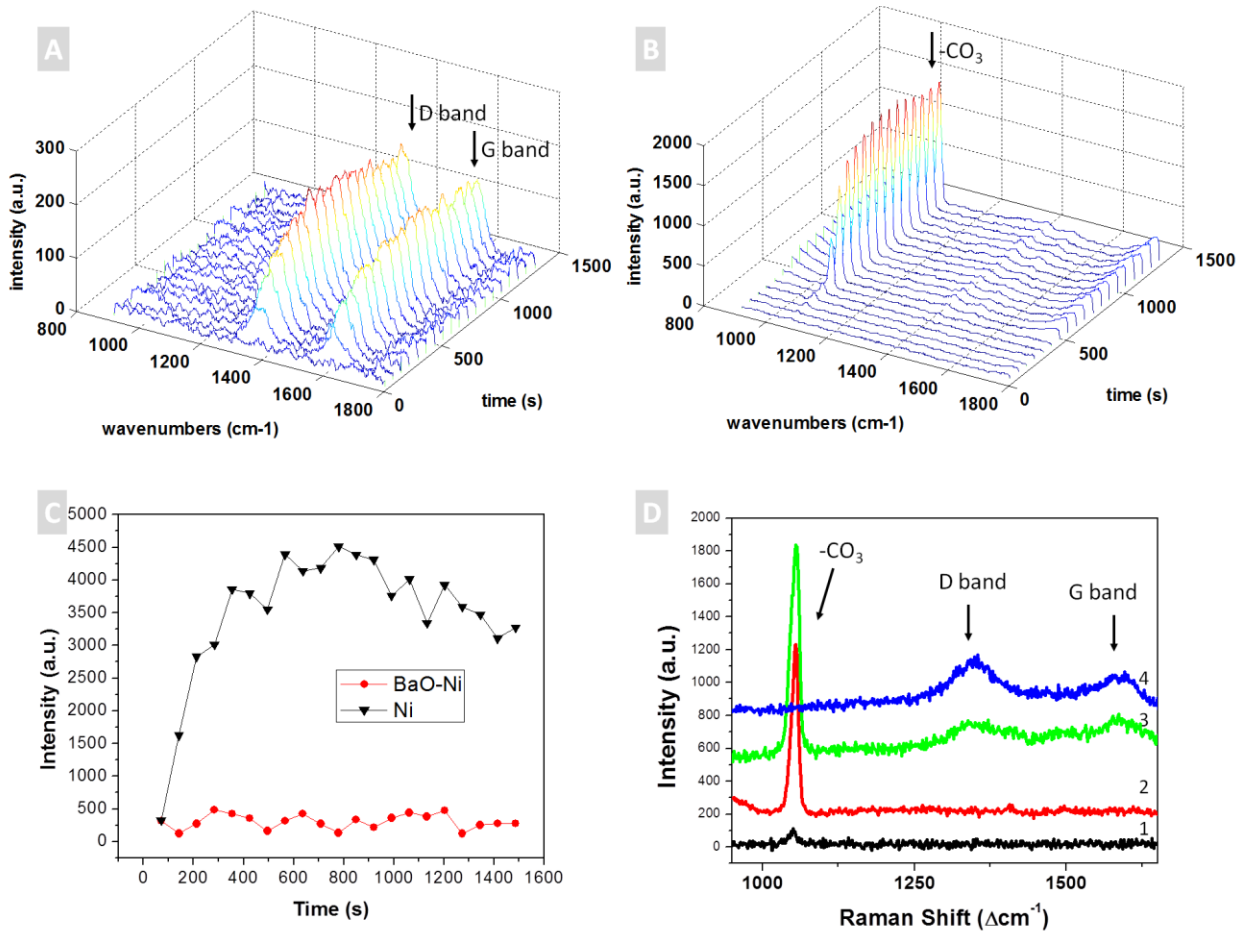

Figure 47: *In situ* Raman analysis of Ni powders and BaO modified Ni powders during propane exposure at ~450^{0}C.
(A) Time resolved Raman spectra collected on Ni powders and (B) BaO modified Ni powders after wet propane was introduced. (C) Intensity of the carbon G-band (1580 cm^{-1}) as a function of duration of propane exposure. (D) Raman spectra collected from 1) BaO-Ni under 4% H_2 2) BaO-Ni under propane exposure for 10 mins 3) BaO-Ni under propane exposure for 4 hrs and 4) Plain Ni powder under propane exposure for 10 mins. All Raman spectra excited by 5mW argon laser emitted at 514nm. Peak intensities integrated within a 20 cm^{-1} bandwidth around the peak position.

Transformations of surface functional groups on BaO during propane exposure were revealed by *in situ* Raman spectroscopy, in order to gain insight for the mechanism of coking resistance. Shown in Figure 48 (A,B) are the time resolved *in situ* Raman spectra collected from

a BaO sample exposed to wet propane (with 3% H_2O), zooming in the change in the intensity of the peaks corresponding to -OH groups and -CO3 groups. The intensities of the -OH and -CO3 peaks as a function of the time exposed to wet propane are presented in Fig. 2(C). Almost immediately after propane was introduced, the -OH band starts to decline, happening simultaneously with the emerging of the -CO3 band, suggesting that the -OH groups on BaO surface reacted with propane or deposited carbon to form -CO3 groups. Time-resolved analysis of BaO powders at 600^0C during the exposure to wet 50% propane (with 3% H_2O, 2% H_2 and 45% Ar) showed more rapid exchange of surface functional groups. As shown in Figure 48 (D), within the first 300 seconds after propane was introduced, the Raman band associated with -OH groups diminished, while a Raman band associated with surface -CO_3 appeared.

The -OH stretching band on BaO powder prior to propane exposure find its origin in a thin layer of $Ba(OH)_2$, due to the adsorption of water vapor from the ambient air. [145, 146] The thin layer of $Ba(OH)_2$ remains stable at 450^0C when exposed to dry 4% H_2, as shown in Figure 49(A). At 600^0C, the thin layer of $Ba(OH)_2$ on BaO surface can decompose under dry 4% H_2, while subsequent exposure to wet 4% H_2 (with 3% H_2O) quickly regenerates the spectral feature associated with -OH stretching, as displayed in Figure 49 (B,C). The formation of $Ba(OH)_2$, was also supported by the significant weight gain on BaO after water exposure in the thermo gravimetric experiments.[6] The $Ba(OH)_2$ layer on BaO surface provided abundant surface –OH groups which could react with deposited carbon on Ni surface and resist coking.

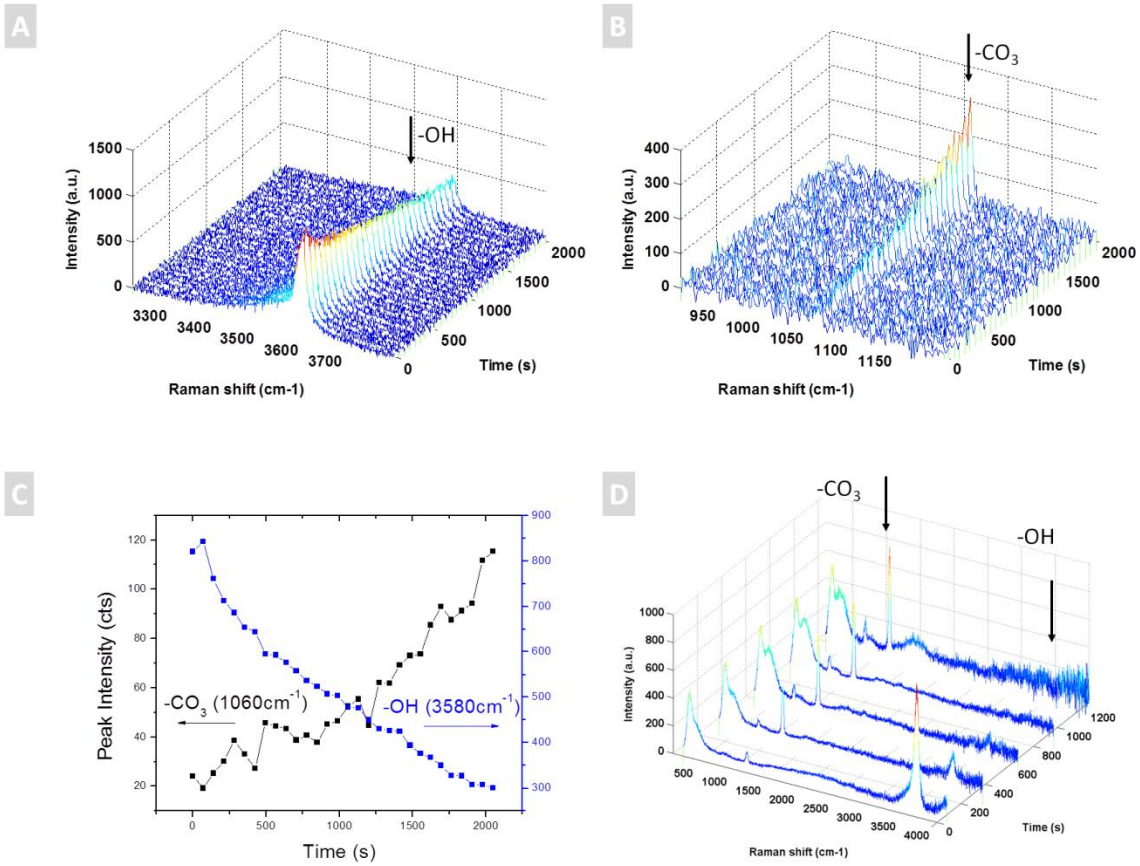

Figure 48: Evolution of surface functional groups on BaO during propane exposure.
(A) Time resolved Raman spectroscopy study of BaO after exposure to wet propane (with 3% H_2O) at ~450^{0}C, zooming in the spectral features associated with -OH group and (B) -CO_3 group. (C) Intensity of the –OH and –CO_3 bands as a function of the exposure time under wet propane. (D) Time resolved Raman spectroscopy study of BaO after exposure to 50% propane (with 3% H_2O, 2% H_2 and 45% Ar) at ~600^{0}C.

The formation of carbonate groups on BaO during propane exposure appears to be an irreversible change to the BaO powder surface. As displayed in Figure 50(A, B), BaO powder samples were heated up to 450^{0}C in 4% dry H_2, and the atmosphere was then sequentially switched to wet 50% propane, 4% wet H_2, CO_2 and dry air. Raman spectra were collected in each gas atmosphere after 30-60 mins exposure, and the intensities of the spectral features of key functional groups at 1060 cm^{-1} (-CO_3), 1580 cm^{-1} (carbon) and 3580 cm^{-1} (-OH) were compared

with respect to gas atmospheres. When the atmosphere was switched from dry 4% H_2 to 50% propane (with 3% H_2O, 2% H_2 and 45% Ar), the Raman band corresponding to –OH groups on BaO diminished while the Raman band corresponding to $–CO_3$ emerged. When the atmosphere was switched to wet 4% H_2, the spectral features remain unchanged, implying that the $–CO_3$ groups formed on BaO were still stable. Further exposure to dry CO_2 did not increase the intensity of -CO3 band, suggesting a saturation of surface carbonate groups. The subsequent exposure to dry air showed no sign of decomposition of the surface carbonate groups.

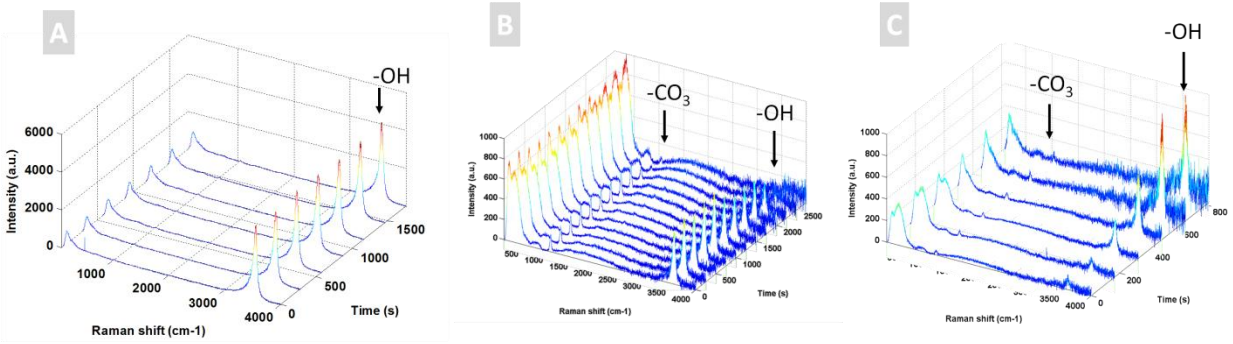

Figure 49: ***In situ*** **Raman spectroscopy analysis of surface -OH groups on BaO powders.**
Spectra collected upon exposure to (A) dry 4% H_2 (with 96% Ar) at 450^0C, (B) dry 4% H_2 (with 96% Ar) at 450^0C and (C) subsequent regeneration with dry 4% H_2 (3% H_2O, 93% Ar).

The irreversible transformation from a surface enriched with –OH groups to one occupied with $-CO_3$ groups was also observed when BaO was exposed to propane at 600^0C, as seen in Figure 50(C, D). The sequence of gas exposure at 600^0C is the same as that at 450^0C, except for the initial gas atmosphere being wet 4% H_2, since the surface –OH groups can be removed at 600^0C in dry gas. For the gas switching from wet H_2 to propane, the –OH groups were replaced by $–CO_3$ groups. Once $-CO_3$ groups occupied the surface of BaO, they cannot be replaced by -OH groups through subsequent exposure to wet 4% H_2. Similar to the situation at 450^0C, continuous exposure to dry CO_2 at 600^0C further increased the intensity of $-CO_3$, while keeping

the sample under dry air showed no sign for surface carbonate decomposition. In addition, the attempt to regenerate -OH groups by keeping the sample under wet 4% H_2 at even higher temperature (700^{0}C) showed no effect, as presented in Figure 51.

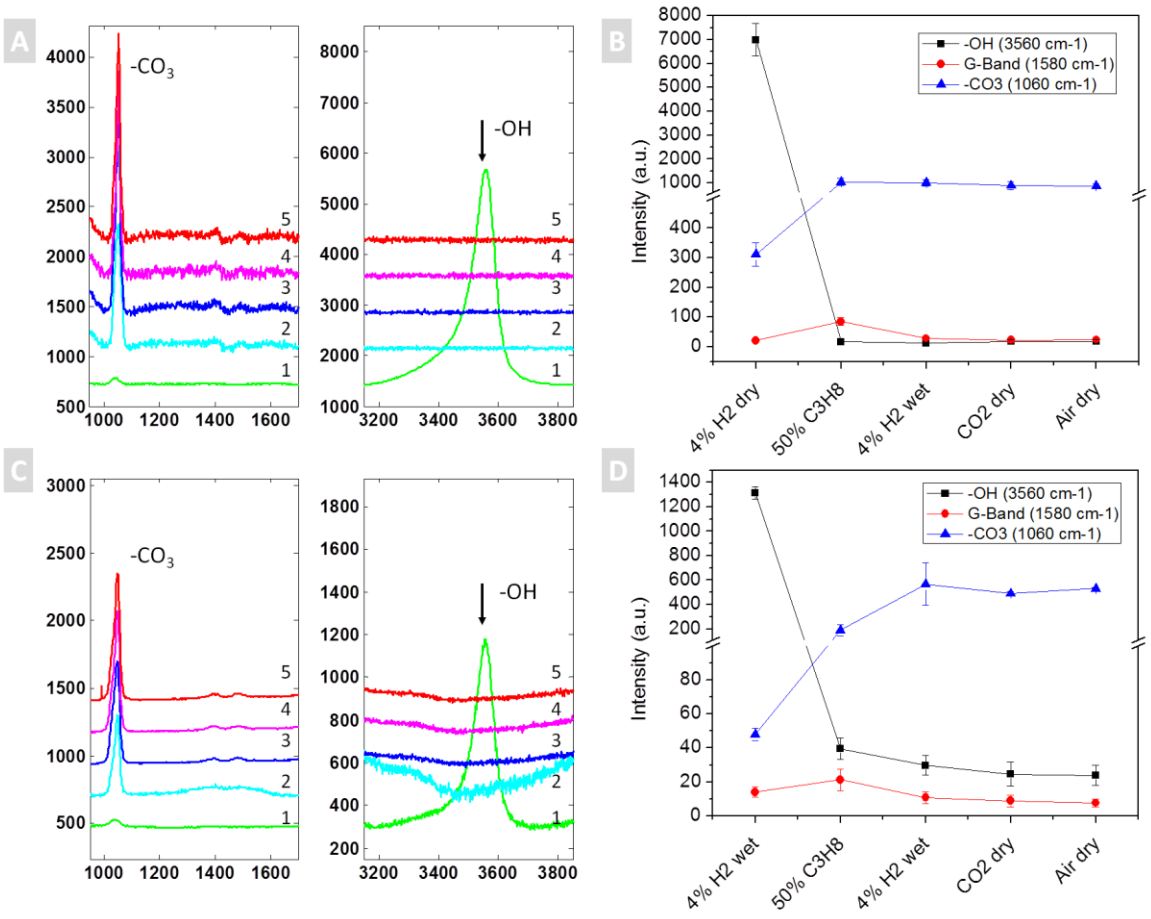

Figure 50: ***In situ*** **Raman spectroscopy study of BaO powders upon exposure to different gas atmospheres.** (A) Raman spectra collected from BaO at ~450^{0}C after exposed to 1) Dry 4% H_2 (with 96% Ar), 2) Dry 50% C_3H_8 (with 2% H_2, 48% Ar), 3) Wet 4% H_2 (with 3% H_2O, 93% Ar), 4) Dry CO_2, and 5) Dry air (B) The intensities of key spectroscopic features with respect to different gas species. (C) Raman spectra collected from BaO at ~600^{0}C after exposed to the variety of gas atmospheres, and (D) the corresponding intensities of key functional groups. All spectra excited with 15mW argon laser emitted at 514nm. Feature intensity calculated by averaging the signal count around the peak within 20 cm^{-1} bandwidth.

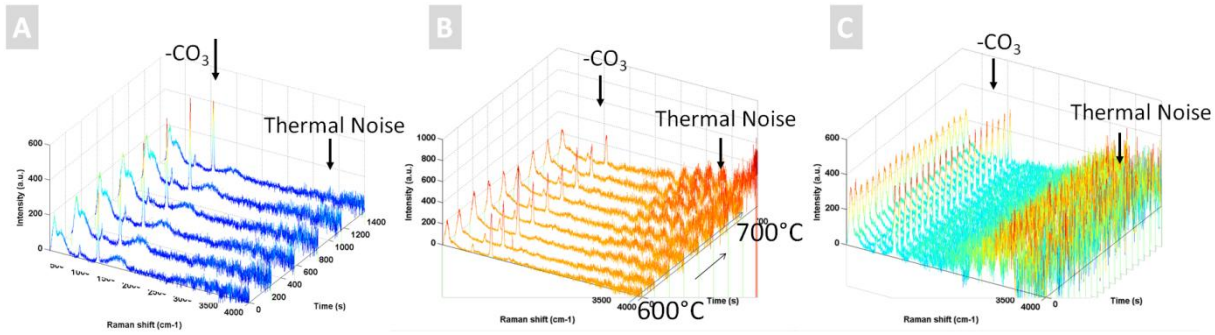

Figure 51: ***In situ*** **Raman spectroscopy analysis of BaO surface after exposure to propane.**
Regeneration attempt with (A) wet 4% H_2 at 600^0C, (B) wet 4% H_2 with temperature ramping from 600-700^0C and (C) intermittent exposure to dry/wet 4% H_2 at 700^0C.

The nature of the spectral feature associated with $–CO_3$ groups is examined by post mortem analysis with synchrotron-based XRD. As shown in Figure 52(A), after exposure to propane, the BaO modified Ni showed prominent patterns associated with witherite structure, indicating the formation of bulk $BaCO_3$.The $BaCO_3$ phase on BaO surface is shown to be stable under both reducing at oxidizing atmospheres, with and without water, preventing BaO from regeneration.The inertness of the $BaCO_3$ covered surface can be attributed to the fact that $BaCO_3$ has high decomposition temperature (~1000^0C).[147]

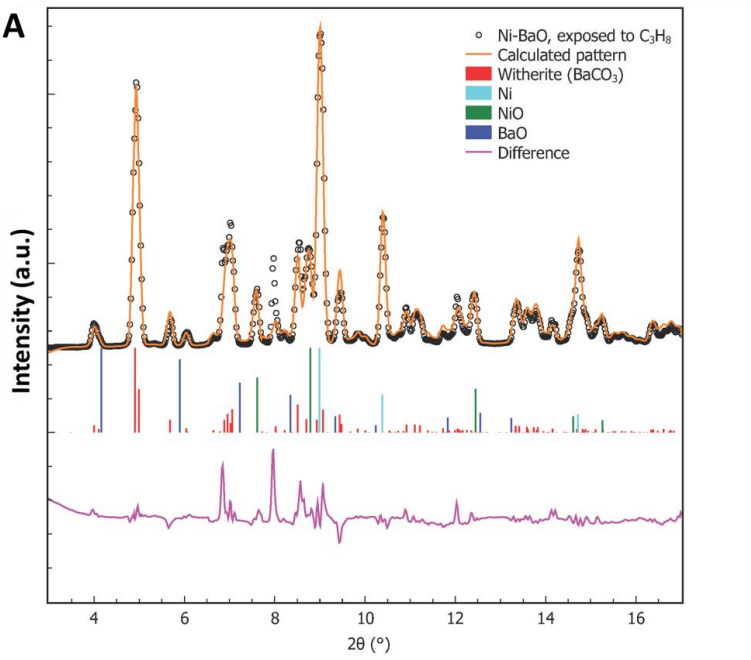

	BaO	BaCO3	Ni	NiO	Graphite
wt %	0.0	49.9	33.3	16.8	0.0

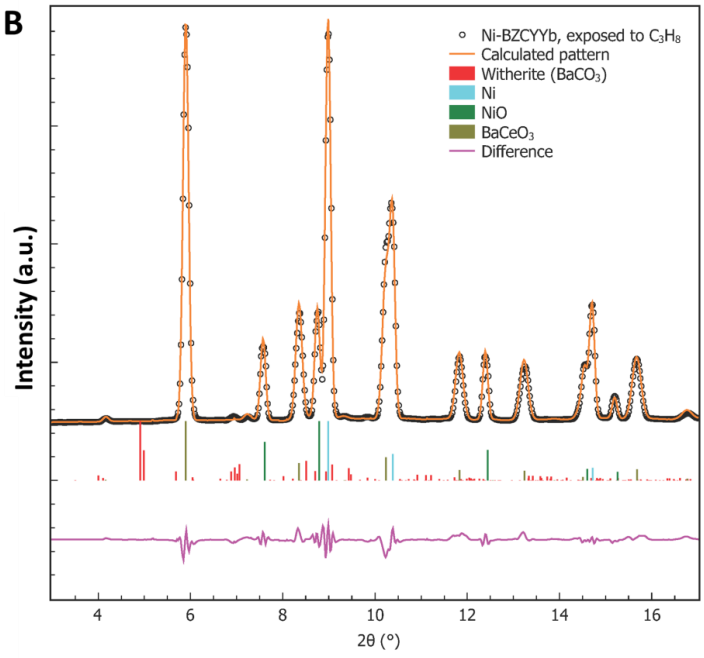

	BaCeO3	BaCO3	Ni	NiO	Graphite
wt %	31.8	0.0	46.6	21.6	0.0

Figure 52: Synchrotron-based x-ray diffraction analysis of BaO and BZCYYb modified Ni.
(A) Mixed BaO-Ni powders and (B) Mixed BZCYYb-Ni powders after exposure to dry 50% C_3H_8 at 600^{0}C for 1hr. Red arrows indicating the formation of witherite ($BaCO_3$) phase.

Based on the analysis of the evolution of surface functional groups, the elementary routes associated with the coking resistance capability of BaO can be formulated as follows:

$$BaO + H_2O = Ba(OH)_2 \quad (1)$$

$$C_3H_8 = 3C_{ad} + 4H_2 \quad (2)$$

$$C_{ad} + Ba(OH)_2 = BaO + CO + H_2 \quad (3)$$

$$CO + Ba(OH)_2 = BaO + CO_2 + H_2 \quad (4)$$

$$BaO + CO_2 = BaCO_3 \quad (5)$$

Eq. (1) depicts the reversible conversion between BaO and $Ba(OH)_2$ when switching between dry and wet atmospheres. Eq. (2-5) propose the elemental route through which the $Ba(OH)_2$ was converted to $BaCO_3$ irreversibly after exposure to propane.

5.5. *In situ* Raman and SERS analysis of Ba-based perovskite catalysts

in situ Raman study on BZCYYb and BZY powders suggested different mechanisms for coking resistance. As displayed in Figure 53, BZCYYb and BZY powders were heated to 450°C and exposed sequentially to dry 4% H_2, propane, wet 4% H_2, CO_2 and air, and the Raman spectra collected from the powder samples after exposure to each atmosphere for 30-60 mins. In contrast those on BaO, the -OH groups on BZCYYb and BZY showed regeneration capability. At initial atmosphere of dry 4% H_2, both BZY and BZCYYb showed prominent spectral features around

3580 cm^{-1}, corresponding to adsorbed -OH groups. On BZY surface (Figure 53 A,B), the propane exposure only slightly decreased the intensity of -OH band , and after subsequent purging of the chamber with wet 4% H_2, the intensity of Raman band of –OH groups recovered. Further exposure to dry CO_2 and dry air decreased the -OH band intensity by ~30%, likely due to desorption of water due to competitive adsorption. On BZCYYb surface (Figure 53 C, D), strong fluorescence background appeared on the high wavenumber range upon the exposure to propane, making the quantification of –OH groups unreliable. After the chamber was purged with wet 4% H_2, the fluorescence noise disappeared along with the carbon peaks, and the -OH band intensity was still found prominent. The carbon D-band and G-band appeared on BZCYYb surface after propane exposure, suggesting carbon deposition on BZCYYb. However, these spectral features related to carbon disappeared after treatment with wet 4% H_2, indicating that the carbon accumulated on BZCYYb surface is easy to remove. On BZCYYb, further exposure to CO_2 and air did not change the intensity of any spectral features significantly.

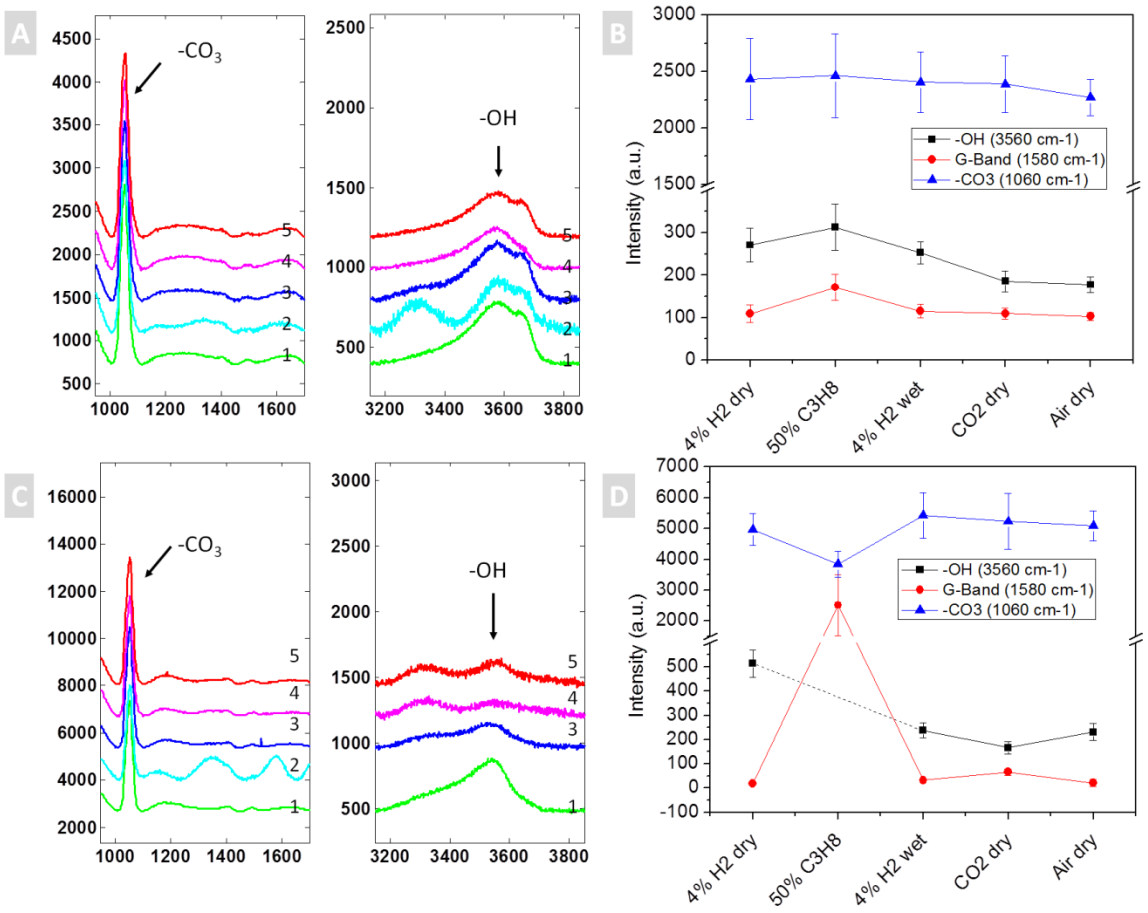

Figure 53: *In situ* Raman spectroscopy study of BZY and BZCYYb upon exposure to different gas atmospheres.
(A) Raman spectra obtained from BZY surface at ~450^{0}C after exposed to 1) Dry 4% H_2 (with 96% Ar), 2) Dry 50% C_3H_8 (with 2% H_2, 48% Ar), 3) Wet 4% H_2 (with 3% H_2O, 93% Ar), 4) Dry CO_2, and 5) Dry air, and (B) the intensities of key spectroscopic features with respect to different gas species. (C) Raman spectra collected from BZCYYb at ~450^{0}C after exposed to the variety of gas atmospheres, and (D) the corresponding intensities of key functional groups. All spectra excited with 15mW argon laser emitted at 514nm. Feature intensity calculated by averaging the signal count around the peak within 20 cm^{-1} bandwidth.

Regeneration capabilities of the surface –OH groups are compared between BaO, BZY and BZCYYb, as displayed in Figure 54. In the pristine state, the –OH groups on BZY and BZCYYb are present in less amount than those on BaO. After exposure to propane, the –OH groups in BaO diminished and cannot be recovered through exposure to wet 4% H_2. On the other hand, the Raman band associated with –OH groups on both BZY and BZCYYb retained its

intensity after propane exposure. Especially, the –OH groups on BZY are shown to be recoverable through exposure to wet 4% H_2. Rather than forming $Ba(OH)_2$, the water vapor introduced only surface –OH groups onto the BZY and BZCYYb powders. The elementary routes of reactions can be described as follows:

$$2H_2O = 2OH_{ad} + H_2 \quad (6)$$

$$2OH_{ad} + 2C_{ad} = 2CO + H_2 \quad (7)$$

$$2OH_{ad} + C_{ad} = CO_2 + H_2 \quad (8)$$

Eq. (6) depicts the dissociative adsorption of water that forms surface –OH groups, and Eq. (7, 8) describes the interaction between surface –OH groups and deposited carbon. In combination with Eq. (2) which shows the decomposition of propane, these steps describe the -OH group mediated removal of carbon deposition on BZY and BZCYYb surface.

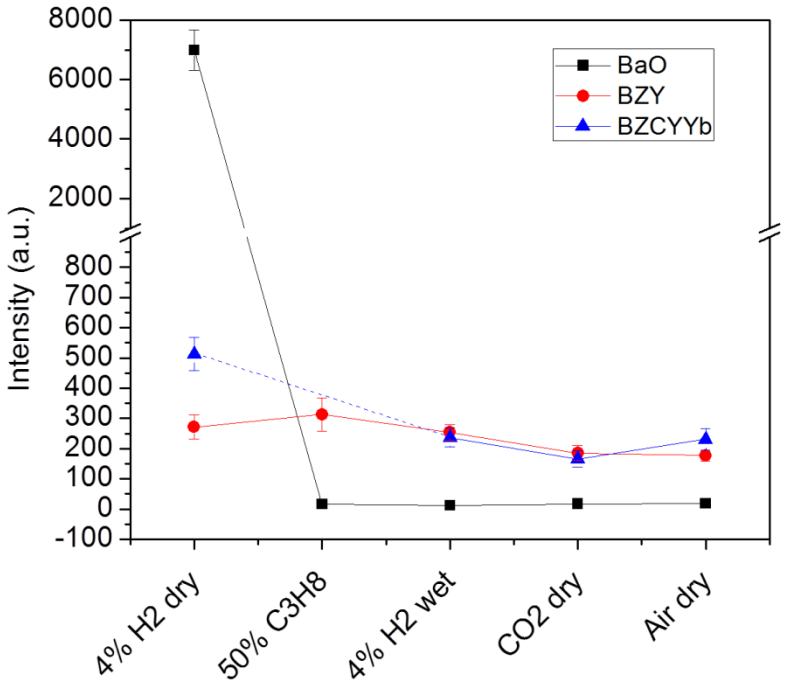

Figure 54: Intensity of -OH band (3580 cm^{-1}) collected from BaO, BZCYYb and BZY upon exposure to different species at ~450^{0}C.
Data regrouped from Fig.3 and Fig. 4 for clear comparison.

The absence of the irreversible formation of surface $BaCO_3$ layer is key to the regeneration capability of BZY and BZCYYb surface. In contrast to Ni-BaO, the mixture of Ni-BZCYYb does not form bulk carbonate after the exposure to propane, as shown in the synchrotron-based XRD analysis of the sample post mortem (Figure 52). More importantly, the -CO_3 groups on the Ba-based perovskites surfaces also appeared to be active in reforming deposited carbon. As indicated in Figure 55(B, D), the intensity of the Raman band associated with –CO_3 groups decreased upon exposure to propane but recovered by wet 4% H_2 exposure. To confirm the interaction between -CO_3 and deposited carbon, time resolved Raman analysis was conducted on BZCYYb powders during the exposure to propane and the subsequent exposure to wet 4% H_2, as shown in Figure 56. Initially, carbonate groups are present on

BZCYYb surface, due to the adsorption of CO_2 during sample preparation. When propane was introduced, the intensity of $-CO_3$ band decreased, and the spectral features associated with carbon increased simultaneously. When the gas atmosphere was switched to wet 4% H_2, the surface carbonate features recovered and the carbon features disappeared. These observations indicate that the surface carbonate groups participate in reforming of deposited carbon.

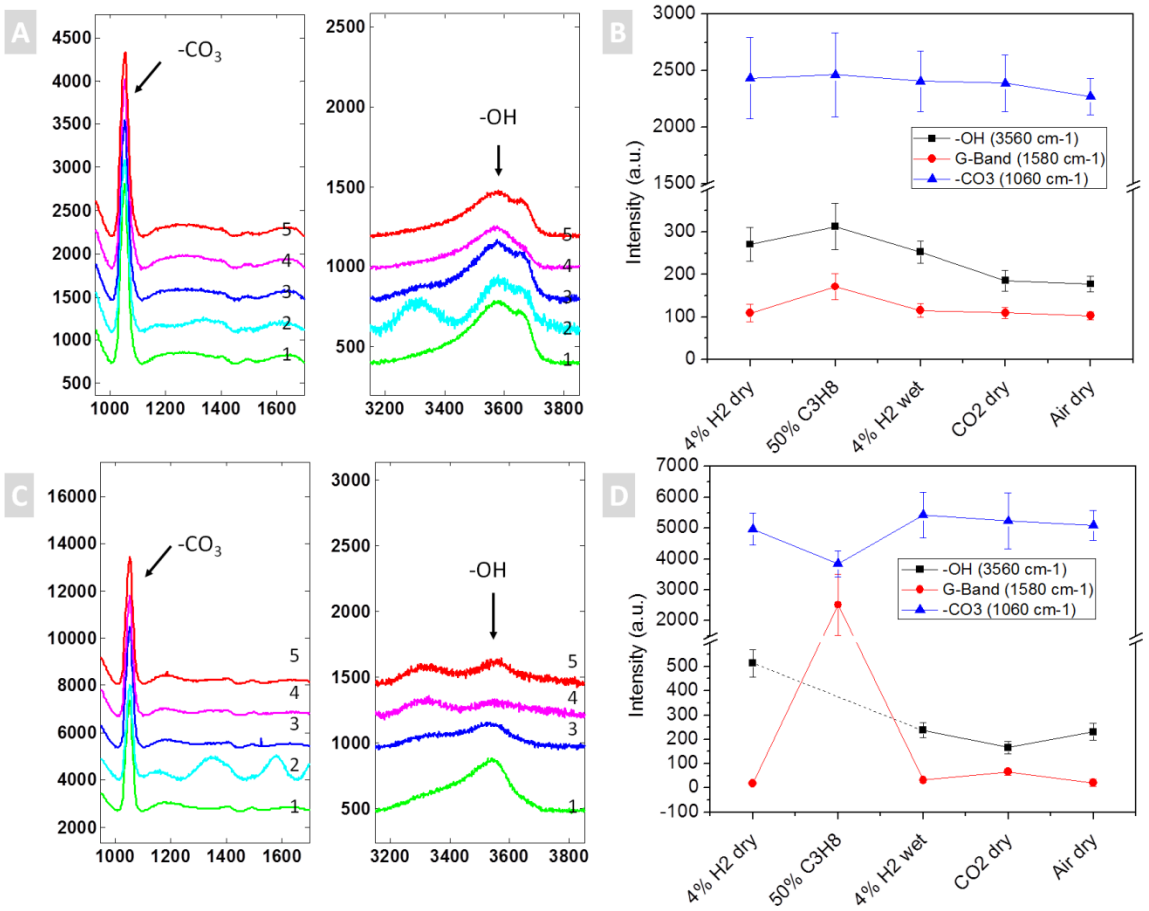

Figure 55: ***In situ*** **Raman spectroscopy study of BZY and BZCYYb after exposure to different gas atmospheres.**
(A) Raman spectra obtained from BZY surface at ~450^{0}C after exposed to 1) Dry 4% H_2 (with 96% Ar), 2) Dry 50% C_3H_8 (with 2% H_2, 48% Ar), 3) Wet 4% H_2 (with 3% H_2O, 93% Ar), 4) Dry CO_2, and 5) Dry air, and (B) the intensities of key spectroscopic features with respect to different gas species. (C) Raman spectra collected from BZCYYb at ~450^{0}C after exposed to the variety of gas atmospheres, and (D) the corresponding intensities of key functional groups. All spectra excited with 15mW argon laser emitted at 514nm. Feature intensity calculated by averaging the signal count around the peak within 20 cm^{-1} bandwidth.

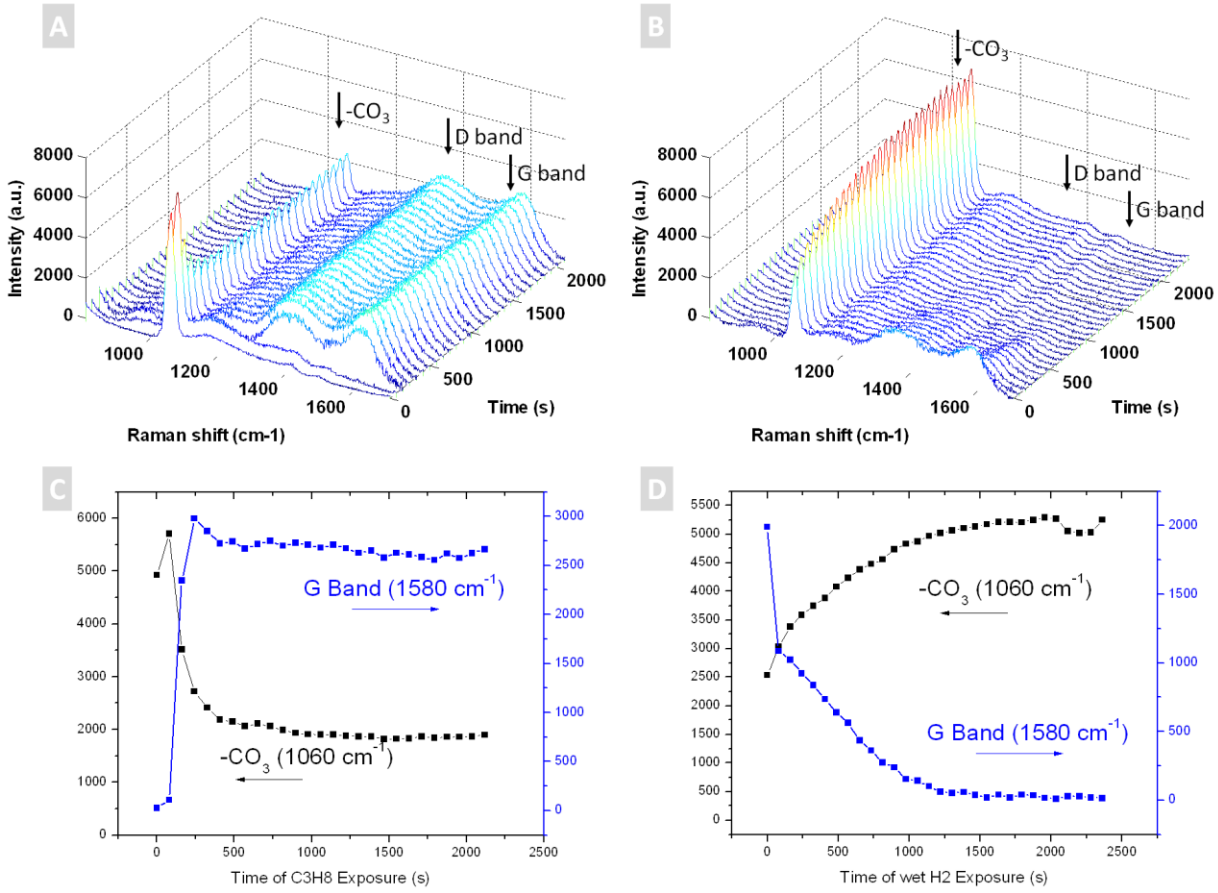

Figure 56: *In situ* Raman analysis of BZCYYb powders upon exposure to propane at ~450^{0}C.
(A) The time-resolved Raman spectra obtained after the introduction of dry 50% C_3H_8 (with 2% H_2, 48% Ar) and (B) after the subsequent purging with wet 4% H_2 (with 3% H_2O and 93% Ar). (C, D) The intensities of key spectral features as functions of propane exposure. All spectra excited with 15mW argon laser emitted at 514nm. Feature intensity calculated by averaging the signal count around the peak within 20 cm^{-1} bandwidth.

The active interaction between surface carbonate groups and carbon deposition suggests BZY and BZCYYb are excellent catalysts to promote CO_2 mediated reforming of carbon deposition. The adsorption and desorption of CO_2 on BZCYYb surface was investigated by *in situ* surface enhanced Raman spectroscopy (SERS), as shown in Figure 57. The Ag@SiO_2 SERS probes[115] was mixed with BZCYYb powders and loaded on Si wafer. The SERS enabled sample was heated up in the environmental chamber under dry air, and held at 400°C until clean

background is achieved. SERS spectra were collected when the sample was exposed to wet 4% H_2 dry CO_2 , dry 4% H_2 and dry CO_2 sequentially. Under wet 4% H_2, strong carbon bands on 1350 cm^{-1} and 1570 cm^{-1} appeared, indicating carbon deposition. While the feeding gas contains no components that promotes coking, the environmental chamber has certain level of carbon deposition, which could react with wet H_2 to form hydrocarbon. SERS picked up the signal from trace amount of carbon deposition due to its ultra high sensitivity. When the feeding gas was switched to CO_2, spectral features associated with carbon deposition disappeared, replaced by a prominent Raman band of surface carbonate. Switching the purging gas again to 4% dry H_2 revealed the Raman signal related to coking, due to the trace amount of carbon source in the chamber. Subsequent CO_2 exposure, again eliminated spectral features related to carbon and made manifestation of -CO_3 peaks. These observations indicate that CO_2 exposure result in reversible adsorption and desorption of surface -CO_3 groups at 400^0C, which actively participate in the reforming of hydrocarbon species on BZCYYb. Elemental reaction steps related to dry reforming of carbon deposition on BZY and BZCYYb surfaces are proposed as follows:

$$CO_2 + O_s = -CO_3 \quad (8)$$

$$-CO_3 + C_{ad} = 2CO + O_s \quad (9)$$

$$2H_2O + C_{ad} + O_s = -CO_3 + 2H_2 \quad (10)$$

C_{ad} is produced by decomposition of propane, as indicated by Eq. (2). Equation (8) describes the reversible adsorption of CO_2 on BZY and BZCYYb surface, forming surface carbonate groups. Equation (9) depicts the interaction between carbon adsorption and surface carbonate groups, while Equation (10) shows the subsequent regeneration of surface carbonates when wet 4% H_2 was introduced.

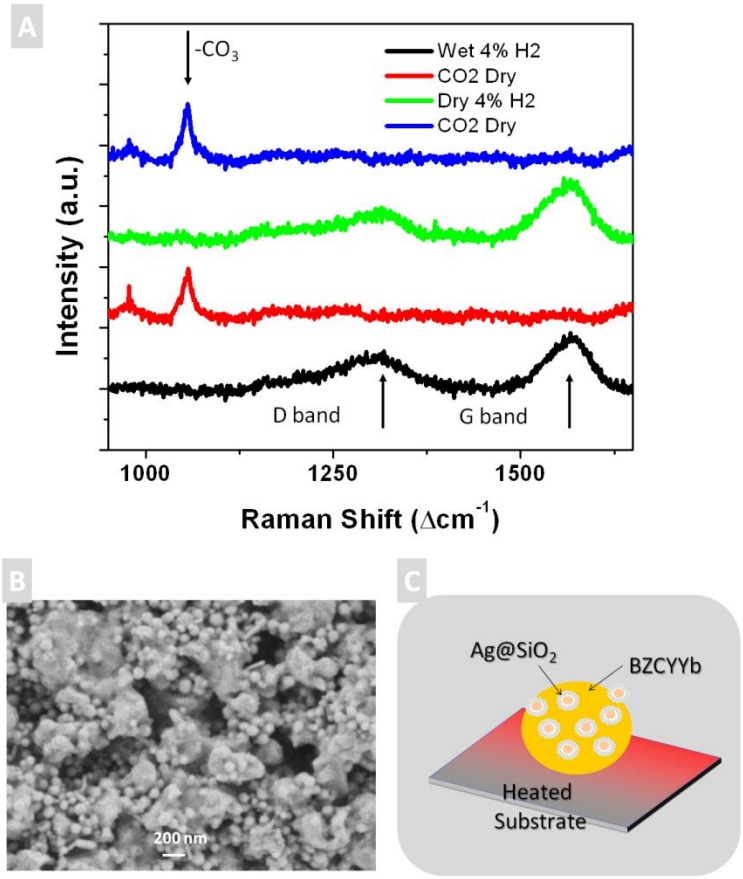

Figure 57: *In situ* SERS analysis of CO_2 adsorption/desorption on BZCYYb surface.
(A) The SERS spectra collected on BZCYYb powders mixed with Ag@SiO_2 nano probes at ~450°C upon the exposure to 1) wet 4% H_2, 2) pure CO_2, 3) dry 4% H_2 and 4) pure CO_2. All spectra processed by subtracting the initial spectrum collected under dry air. (B) SEM image of Ag@SiO_2-BZCYYb mixture after high temperature tests and (C) schematic of sample prepared for high temperature *in situ* SERS analysis. All spectra excited with 15mW argon laser emitted at 514nm.

5.6. Reforming routes of deposited carbon

BaO and Ba containing perovskites (BZY and BZCYYb) showed different pathways for coking resistance, as presented in Scheme 1.Upon water exposure, BaO develops a thin layer of $Ba(OH)_2$ on the surface, which reacts with deposited carbon and turns into $BaCO_3$. BaO has

strong basicity, and readily reacts with CO_2 to form $BaCO_3$ on the surface, keeping BaO from regeneration. The –OH groups on BZY and BZCYYb, in contrast, show capability of regeneration. Exposure to propane does not result in exhaustion of surface –OH groups, and purging with wet 4% H_2 could regenerate a considerable portion. More importantly, the surface –CO_3 groups on BZY and BZCYYb react with propane and surface carbon deposition, and thus resist coking through a possible CO_2 reforming route. Similarly, the –CO_3 groups on BZY and BZCYYb can also be replenished. Both water and CO_2 mediated coking removal pathways happen on the surface of BZY and BZCYYb. Since H_2O and CO_2 are the natural products of SOFC anode reactions, BZY or BZCYYb modified anodes could be self cleaned during operation. [12, 52]

Fast turnover of the –OH and –CO_3 groups is critical to coking resistant catalysts. On one hand, the catalysts need high basicity to facilitate dissociative adsorption of H_2O and CO_2, while on the other hand, the catalyst need to avoid formation of inert bulk phase that prevents regeneration. BaO, as shown in this study, provided excellent coking resistance at the early stage due to its large amount of –OH groups. However, reaction between BaO and CO_2 formed $BaCO_3$ irreversibly, which could be undesirable for the catalyst application. Therefore, to optimize the coking resistance through surface modification, it is vital to adjust the catalysts affinity to H_2O and CO_2 to appropriate level.

The results presented herein do not disqualify BaO as an effective catalyst for coking resistant SOFC anode, since the presence of anodic current flow can help remove the carbon deposition on the nickel-based anode, resulting in less destructive consumption of surface -OH

groups.[6] In addition, the BaO-Ni nano interface may stabilize the BaO from phase transformation. Nevertheless, the irreversible formation of $BaCO_3$ evidenced a potential degradation route of BaO catalyst when it is used as anode modification, which should not be overlooked.

5.7. Chapter Conclusions

To investigate the influence of BaO-Ni interface on the resistance of carbon deposition, block co-polymer patterning was used to create uniformly distributed BaO nano rings on Ni surface. Electrostatic force microscopy (EFM) identified the distribution of carbon deposition according to the different surface potentials of nickel and carbon patches. As evident from Raman spectroscopy and SEM, BaO modification enhanced coking tolerance of nickel foil. The EFM analysis of the nickel surface after hydrocarbon exposure indicated that the presence of BaO nano-catalysts prevented the formation of solid patch of carbon encapsulation and thus improved the coking resistance of nickel-based SOFC anode significantly.

In situ Raman and SERS analysis of the surfaces of BaO, BZY, and BZCYYb revealed the details of the formation and evolution of surface functional groups related to carbon removal. While the surface $Ba(OH)_2$ layer on BaO surfaces readily react with hydrocarbon molecules in the gas or carbon atoms on Ni surface, providing coking resistance, $BaCO_3$ developed on the BaO surface in the process and prevented regeneration of surface -OH groups. On BZY and BZCYYb surfaces, in contrast, both -OH groups and $-CO_3$ groups are present in the form of surface adsorption, readily reacting with deposited carbon while being capable of regeneration. BZY and BZCYYb facilitate both steam reforming and CO_2 reforming of deposited carbon,

making them excellent candidates for coking-resistant catalysts for surface modifications of SOFC anodes. In this study, *in situ* Raman and SERS technique provided critical information of the interactions between catalysts and gas species under operating conditions. Extensive utilization of *in situ* Raman and SERS on fuel cell anodes and hydrocarbon reforming catalysts may help unravel complex reaction mechanisms that are critical to the knowledge-based material design.

CHAPTER 6: **SULFUR POISONING OF NI-BASED ANODE**

Sulfur poisoning is another major factor that impairs the performance of nickel-based SOFC anodes. When ppm level of H_2S is present in the fuel gas, the nickel-based anode suffers significant performance drop immediately and slow but steady performance degradation under long term operation.[148] S adsorption on nickel surface is widely accepted as the key step responsible for the sulfur poisoning. However, the detailed mechanisms that lead to performance degradation are not well understood. Similarly, while many surface modification strategies report excellent sulfur tolerance, the mechanisms that provide the poisoning resistance has not been elucidated.[52]

The most active electrochemical interface on the Ni-based anode is the triple phase boundary, where electrons, oxygen ions (or protons), and fuel molecules meet and react with each other. The performance of a nickel-based anode depends sensitively on the accessibility of the TPBs by the reactants involved in fuel oxidation. Accordingly, coking or sulfur deposition on the TPB region could block the accessibility of reaction species, and thus degrade anode performance. On the other hand, TPBs are also "hot spots" for the electrochemical oxidation of fuel molecules and deposited carbon, and thus have certain degree of self-cleaning capability.[57] In addition, the interface between Ni and electrolyte materials may possess unique catalytic properties, since the electrolyte and nickel could act as synergetic couples for a variety of chemical and electrochemical reactions.[118-121]

The triple phase boundary of the SOFC anodes is a complicated electrocatalytic system which critically influences the performance and stability of SOFC systems, and the fundamental

knowledge in this area are difficult to unravel. Conventional electrochemical testing with porous electrode cannot isolate the contribution from material intrinsic properties, surface properties and the influence of microstructures. The use of well-defined metal-electrolyte interfaces could effectively remove the complexity brought in by the random microstructure of porous anodes, providing additional insight into sulfur poisoning mechanisms. Foremost, the simpler architecture allows us to fine-tune one property at a time and mapping of the deposition of sulfur-related species near the TPB area. The anticipated outcome of analysis of patterned electrodes is improved surface modifications, material combinations and microstructures for sulfur tolerant SOFC anodes.

This chapter focuses on investigating the factors influencing the sulfur poisoning on Ni-electrolyte interfaces. Well-defined triple phase boundaries were fabricated through an embedded mesh method, providing a unique platform for the isolation of factors responsible for coking and sulfur poisoning. Surface enhanced Raman spectroscopy was applied to study the surface adsorption species correlating to the sulfur poisoning process.

6.1. Patterned Electrode Study of Sulfur tolerance on Ni-based anode

Different combinations of electrode and electrolyte materials and surface modifications were evaluated through the fabrication of patterned electrodes to reveal the key factors responsible for the susceptibility to sulfur poisoning, as shown in Figure 58. To evaluate the effect of metal component on sulfur tolerance, different metal gauze (Ni, Pt) were used to fabricate patterned electrode with the YSZ electrolyte. The influence of surface modification was evaluated by different surface modifications (BaO, GDC, BZCYYb) on top of the Ni/YSZ

patterned electrodes. In addition, Ni patterned electrodes interfaced with different electrolyte materials, Ni/YSZ and Ni/BZCYYb, was assessed to identify the impact of electrochemical interface on sulfur tolerance.

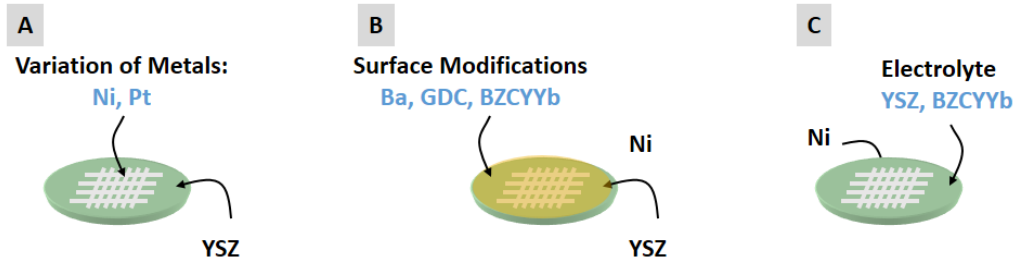

Figure 58: Architectures of patterned electrode for study of sulfur poisoning.
(A) cells with different metal components in YSZ electrolyte: Ni and Pt. (B) Ni-YSZ cells with different surface modifications: BaO, GDC, BZCYYb (C) cells with different electrolytes: YSZ and BZCYYb.

The susceptibility of Ni and Pt metals to sulfur poisoning was investigated by testing the modeled fuel cells with patterned electrodes, at 750^0C with H_2 containing different concentrations of H_2S. Under a constant cell terminal voltage of 0.7V, the cell power output with clean H_2 as fuel were used as the normalization factor for estimation of sulfur poisoning. As shown in Figure 59, Pt electrode showed no performance degradation for H_2S level up to 50ppm, but Ni mesh suffered severe performance loss upon the exposure to the 10ppm of H_2S. The observation suggests that Ni is susceptible to sulfur poisoning, and the metal phase is critical to the susceptibility to sulfur related performance degradation.

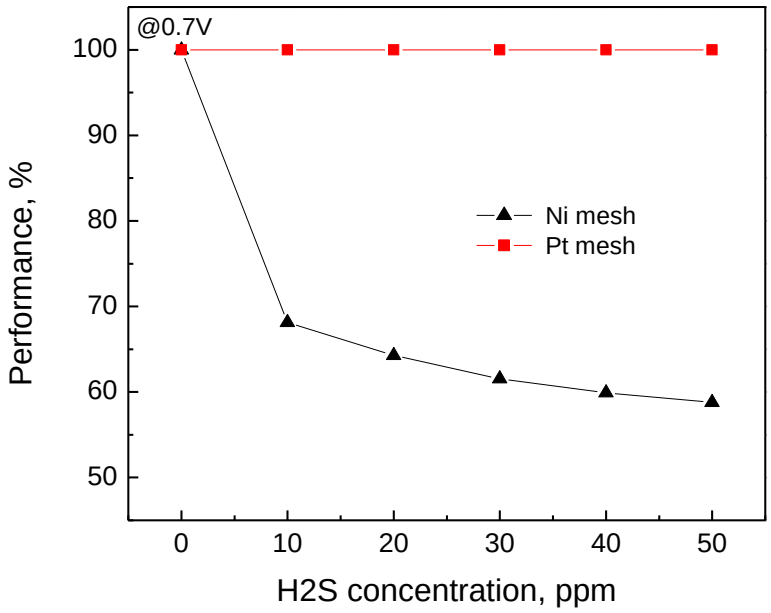

Figure 59: Impact of metal phase on H_2S susceptibility of the modelled anode.
Performance loss of cells with pattern electrodes measured under different H_2S concentrations. (Data courtesy of Mingfei Liu)

Modification of the surface of patterned Ni-YSZ interface was investigated for the effectiveness of different catalysts to prevent S poisoning. The surface modification of BaO was applied through the spin coating of aqueous $Ba(Ac)_2$ solution, which decomposed to BaO when the cell was heated. The modification catalysts of GDC and BZCYYb were loaded through RF sputtering. Both the GDC and BZCYYb sputtering targets were home-made by dry-pressing and sintering. The working pressure during the sputtering was 2.5 mBar, and the power utilized was 20W. The amount of the modification catalysts was controlled by sputtering time: 5 min for GDC and 10 min for BZCYYb. The patterned electrodes were tested under potentiostatic mode at 750C upon the exposure to H2 with different level of H_2S contamination. As shown in Figure

60. Compared to the unmodified Ni-YSZ patterned electrode, GDC and BZCYYb showed improvement in sulfur tolerance, while BaO showed little effect.

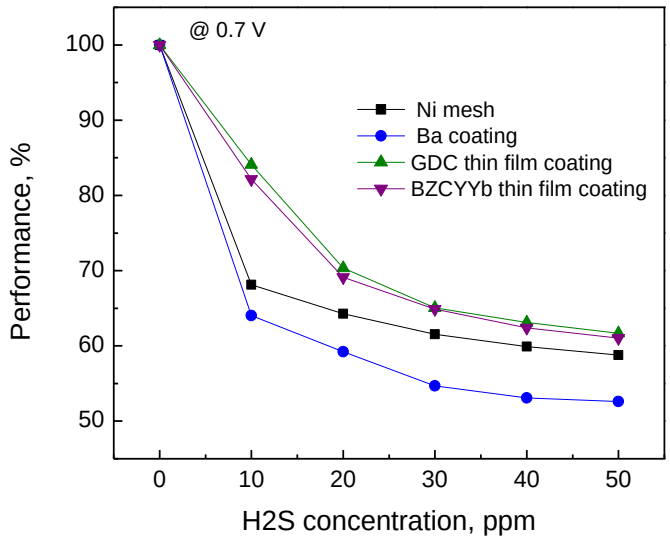

Figure 60: Impact of surface modification on susceptibility of H_2S poisoning.
Performance loss recorded on modelled cells with pattern electrode of Ni-YSZ, modified with BaO, GDC and BZCYYb, upon exposure to different concentration of H_2S. (Data courtesy of Mingfei Liu)

The electrolyte phase of the electrochemical interfaces also showed significant impact on the capability of sulfur tolerance. Before introducing H_2S into the system, all testing cells were held at terminal voltage of 0.7V under pure H_2 to establish a steady baseline in performance. Shown in Figure 61, Ni-YSZ cell has a much lower cell performance than Ni-BZCYYb cell, due to the lower ionic conductivity of YSZ at 767°C. After switching gas from clean hydrogen to hydrogen containing 0.5ppm H_2S, the Ni-YSZ cell suffered a 30% performance loss within 1 hr, while in the same testing period, the performance loss of the cells based on Ni-BZCYYb was insignificant. After switching back to clean hydrogen, the performance of the Ni-YSZ cell

recovered. The current-voltage curves revealed the origin of difference of sulfur tolerance. It is found that the OCV of the Ni-YSZ cell decreased from 1.00V to 0.96V, in addition to an increase in anodic polarization, resulting in the performance loss of ~30% at 0.7V. In contrast, the Ni-BZCYYb cell showed no significant change in OCV or polarization resistance when the gas was switched to the H_2S contaminated hydrogen, indicating superior resistance towards 0.5ppm H_2S.

The Ni-BZCYYb cell was further tested under 2-10 ppm levels of H_2S, as displayed in Figure 62. While under 2ppm and 5ppm H_2S, the Ni-BZCYYb electrodes showed no performance degradation, the cell eventually loss performance when 10ppm H_2S was introduced. It needs to be noted that the patterned electrode shown here represent a condition more favorable for sulfur poisoning, in which the nickel has a broad terrace that could be contaminated without the sulfur removal effect from the anodic current. Even through, the patterned electrode showed excellent tolerance up to 5ppm H_2S, meeting the need of most industry scale SOFCs.

The stable performances of the cells with Ni-BZCYYb patterned electrode when exposed to H_2 or contaminated with 2ppm H_2S suggest that the Ni-BZCYYb interface has intrinsic tolerance to sulfur poisoning. A plausible speculation ascribes the sulfur tolerance capability to the proton conductivity of BZCYYb. While the nickel surface are susceptible to sulfur deposition, blocking the transport of H_2 to the triple phase boundary, the presence of BZCYYb provides for an alternative site for hydrogen adsorption and subsequent reduction. In the aspect of hydrogen reduction, the Ni-BZCYYb interface provided a broadened triple phase boundary compared to Ni-YSZ interface. Since BZCYYb itself is not susceptible to sulfur deposition in the presence of ppm level of H_2S, the hydrogen reduction path would not be blocked, and the influence on cell performance is minimized.

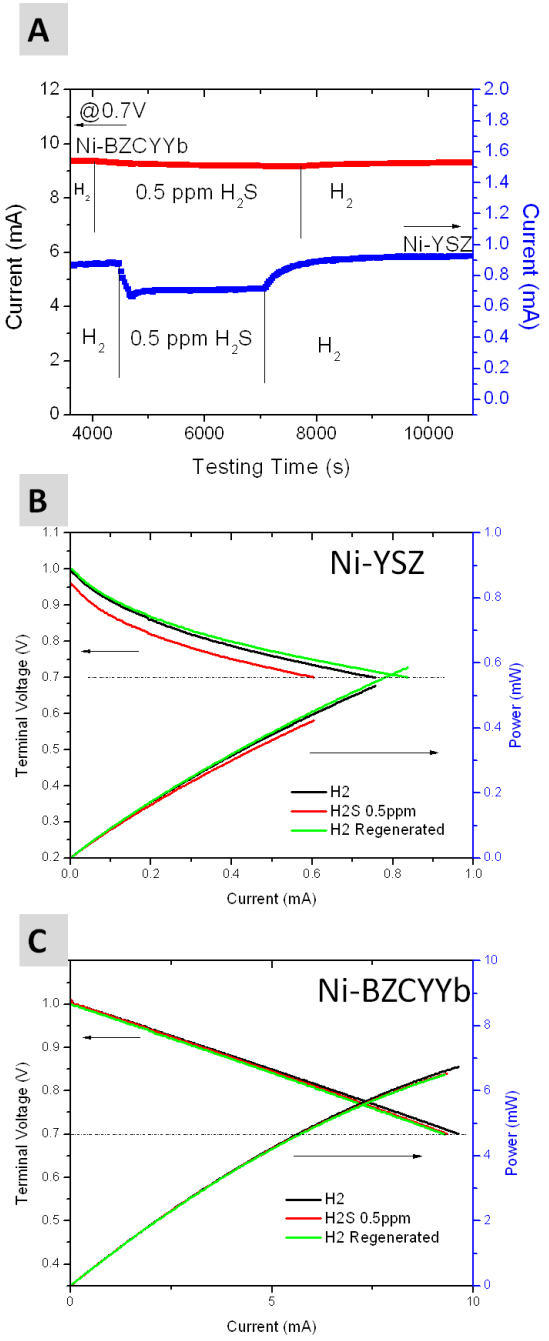

Figure 61: Impact of electrolyte phase on susceptibility of anode to sulfur poisoning (0.5 ppm H_2S).
(A) Performance variation under a constant terminal potential of 0.7V. (B) The I-V curves under indicated conditions of Ni-YSZ and (C) of Ni-BZCYYb.

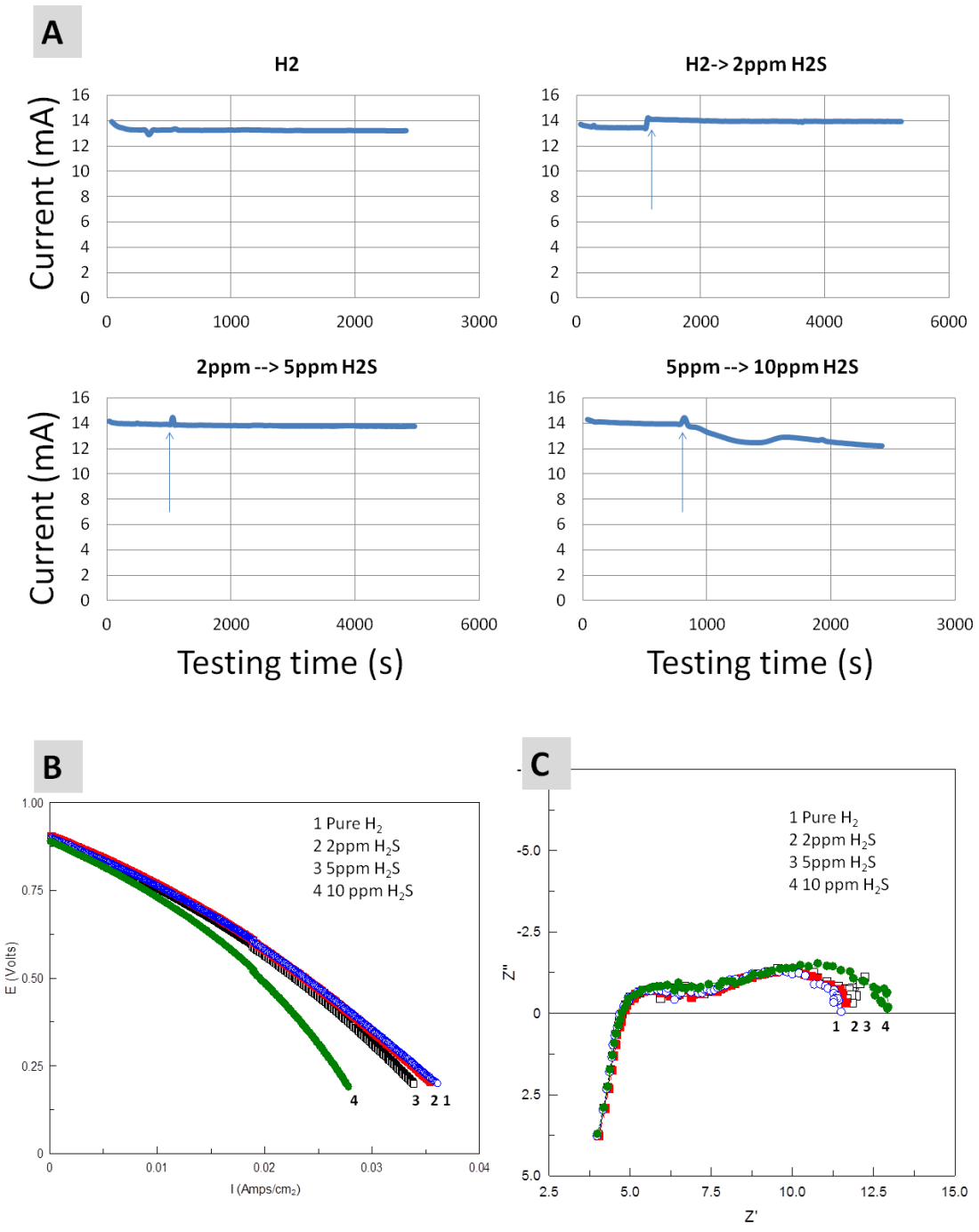

Figure 62: Impact of electrolyte phase on susceptibility of anode to sulfur poisoning (2-10 ppm H_2S).
(A) Electrochemical performance test under a constant terminal potential of 0.7V. (B) The corresponding discharging curves and (C) Impedance spectra

6.2. SERS Analysis of Sulfur Adsorption on Nickel Surface

Nickel-based SOFC anode operated with fuels containing ppm level of H_2S suffer immediate performance loss and also long term degradation.[26, 148-150] Adsorption of sulfur related species on the nickel surface is closely related to the degradation of performance, due to the blocking of surface active sites. [151] However, challenges exist in identifying and quantifying the sulfur depositions on nickel surface. At SOFC operating temperatures, sulfur is present in the form of adsorbed sulfur.[152] Once the cell is extracted from the reacting atmosphere, the sulfur atoms could quickly desorb from the surface through reaction with H_2. The formation of nickel sulfide is not favorable at operating temperatures as high as 750^0C. [27]

Previous Raman spectroscopy studies of S poisoning over Ni anode did not show spectral features related to the formation of sulfur or sulfide at operating temperatures. The adsorbed atomic sulfur may not generate enough Raman scattering upon the laser excitation. The analysis *ex situ*, however, may be complicated by the route through which the contaminated nickel foil cooled to room temperature. As reported by Cheng et al.,[153] when the nickel foil was cooled down slowly to room temperature in 100ppm H_2S, strong signal related to NiS and adsorbed S can be resolve. However, when the nickel foil was cooled to room temperature under H_2, or quenched in H_2S containing gas, the species related to S poisoning are absent. While quenching preserves the original nickel surface after sulfur exposure, the concentration of the contaminants might be too low for ordinary Raman analysis.

SERS dramatically enhanced the sensitivity of surface sulfur species after H_2S exposure, as shown in Figure 63. The Ni foil was exposed to 0.5ppm H_2S at 767^0C for 12 hrs, before quickly quench to RT (~300^0C/min) under the same H_2S containing condition. Prior to SERS

treatment, the Ni foil showed no peaks related to sulfur deposition. After Ag sputtering, the SERS phenomena revealed several Raman bands on the Ni foil, related to the presence of elemental sulfur, NiS and Ni_3S_4. The exact peak assignments are listed in Table 6.

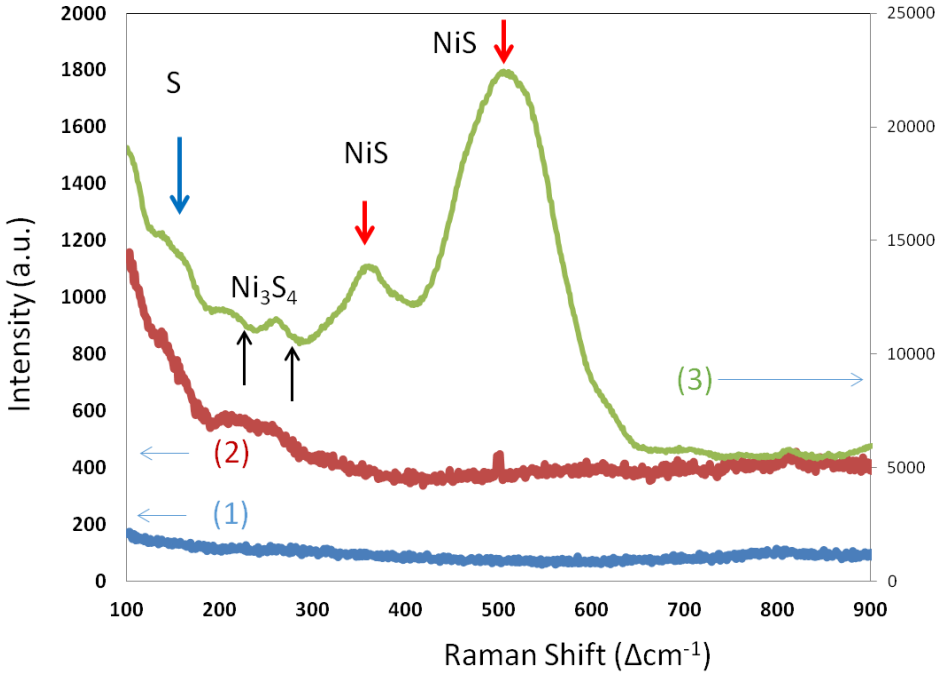

Figure 63: SERS identification of the speceis related to S poisoning on Ni foil after heat treatment in H_2S. (1) Ordinary Raman spectra of the H_2S poisoned Ni foil (quenched under H_2S containing atmosphere). (2) SERS spectra of the same sample. (3) The SERS spectra of the Ni foil annealed in pure H_2.

SERS analysis revealed the sulfur deposition on nickel surface in even lower level of H_2S exposure (0.01ppm, 0.1ppm and 0.5ppm) at 767^{0}C for 12hr, as presented in Figure 64. These three samples were purged with pure H_2 for 2 mins before quickly cooling to RT (~300^{0}C/min) under pure H_2 and then maintaining this atmosphere for an extra 2 mins. The Ag nanoparticles were then loaded onto the samples and SERS spectra were collected. Although the intensities of sulfur related species are much weaker in these scenarios than shown in Figure 8, the main peaks related to S deposition, mainly the elemental S, Ni_3S_4 and NiS are still observable. The quantity

of S is not clearly correlated with the H_2S level of exposure, possibly due to the fact that S preferentially deposits onto the Ni surface, and the change of H_2S level did not change the coverage significantly, which is also supported by the previous thermodynamic calculations. [154, 155]

Table 6: Assignment of the spectral features in SERS analysis of Ni foil after H_2S exposure

Ni_3S_2	200, 220, 302, 321, 350
NiS	250, 302, 350, 375, 390, 485, 510, 570, 670, 985
Ni_3S_4	207, 225, 288, 325, 342, 383, 475
NiS_2	306, 340, 386
NiO	210, 410, 540, 730, 900, 1090, 1480
S_2	154 221 475
Tested	150, 165, 205, 230, 260, 285, 360, 510, 650, 705, 820, 930, 1000, 1331, 1600

SERS also revealed that different Ni grains have differing amounts of sulfur deposition, as illustrated from the mapping of 520 cm^{-1} peak across the grain boundary shown in Figure 65. Within the grain, on the other hand, SERS showed consistent intensity, validating that the SERS providers assume good uniformity over the surface.

SERS provided evidence of the presence of trace amount of elemental sulfur, NiS and Ni_3S_4 on the nickel surface. Since nickel sulfide cannot form at high operating temperatures, [27] we postulated that these sulfide species were generated during the quenching and cooling process. This hypothesis is validated in the *in situ* SERS analysis presented below.

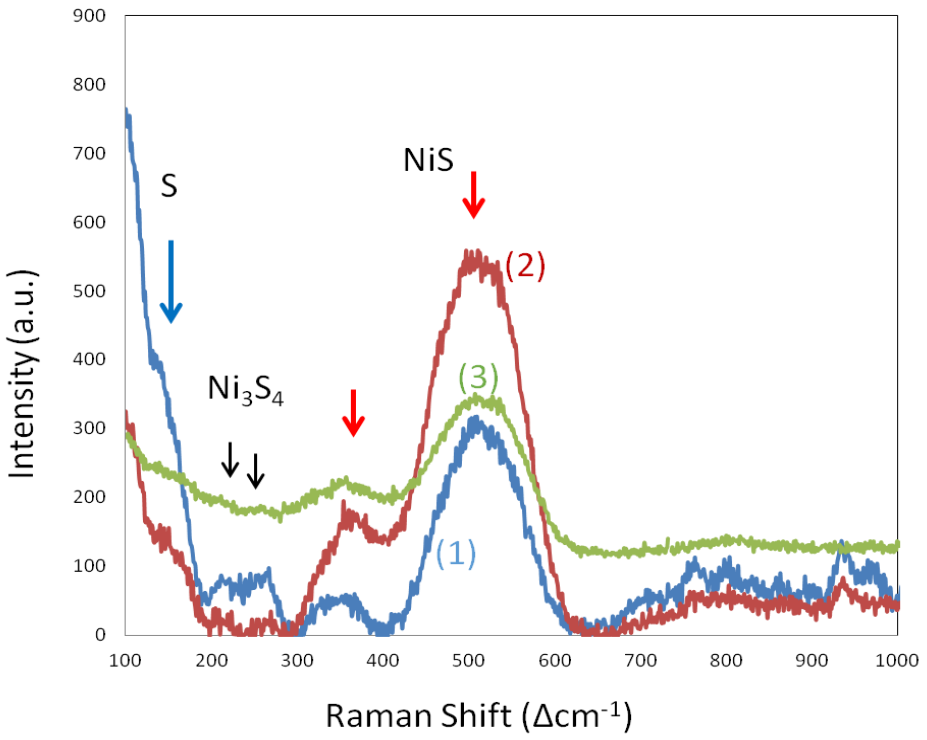

Figure 64: SERS analysis of Ni foil after exposure to different H_2S levels.
Ni foil exposed to different H_2S levels (0.01-0.5ppm) at 767^{0}C for 12hr and quenched under pure H_2. (1) Exposure to 0.01 ppm H_2S, (2) 0.1 ppm H_2S and (3) 0.5 ppm H_2S.

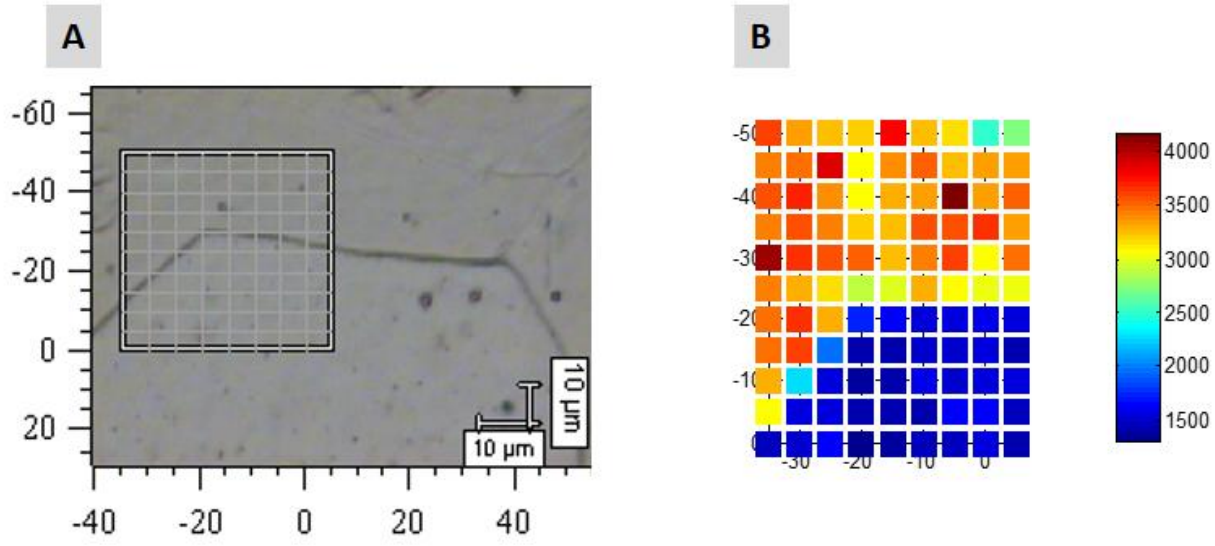

Figure 65: SERS analysis of Ni foil after H_2S exposure.
(A) Scanned regions indicated in optical microscope image. (B) The intensity map of 510 cm^{-1} peak of the scanned region. Ni foil exposed to 0.5ppm H_2S for 12 h and quenched under pure H_2.

Performing SERS at elevated temperatures using sputtered Ag nanoparticles is problematic due to agglomeration of the particles and loss of SERS capacity. To enable the high temperature SERS analysis of the surface of electrodes *in situ*, we developed core-shell structured Ag nanoparticleswhich enabled *in situ* study of sulfur adsorption on nickel surface at temperatures as high as 450^0C.[156]

Ag@SiO_2 nanoparticles dispersed in ethanol solution were introduced to a clean nickel foil by drop coating. The sample was then heated to 450^0C in air to remove all organic residues in the SERS suspension and then exposed to pure H_2. The fabrication of Ag@SiO_2 nanoparticles and enhancement factor calibration are described in Section **Error! Reference source not ound.**.

In situ SERS analysis was conducted under different atmospheres and temperatures, as displayed in Figure 66(A). Nickel was first exposed to 0.5ppm H_2S containing hydrogen, which yielded no signal related to sulfur adsorption. Even the overnight exposure to 0.5 ppm H_2S did not generate any distinguishable Raman feature related to sulfur poisoning. Afterwards, the nickel foil was quenched to room temperature under pure H_2. As the temperature dropped, a peak on 510 cm^{-1} evolved, indicating the formation of NiS.

This observation supported the previous speculation that sulfur adsorbed on the nickel surface is not completely removed with hydrogen purge. The remaining adsorbed sulfur is converted into NiS, Ni_3S_4 and S_2 as temperature quickly dropped. The pathway of the formation of sulfur related species is proposed in Figure 66(B). In accordance with this hypothesis, the observation of *ex situ* sulfur species in the quenching experiments can be directly correlated to the sulfur adsorption on the nickel surfaces at operating conditions.

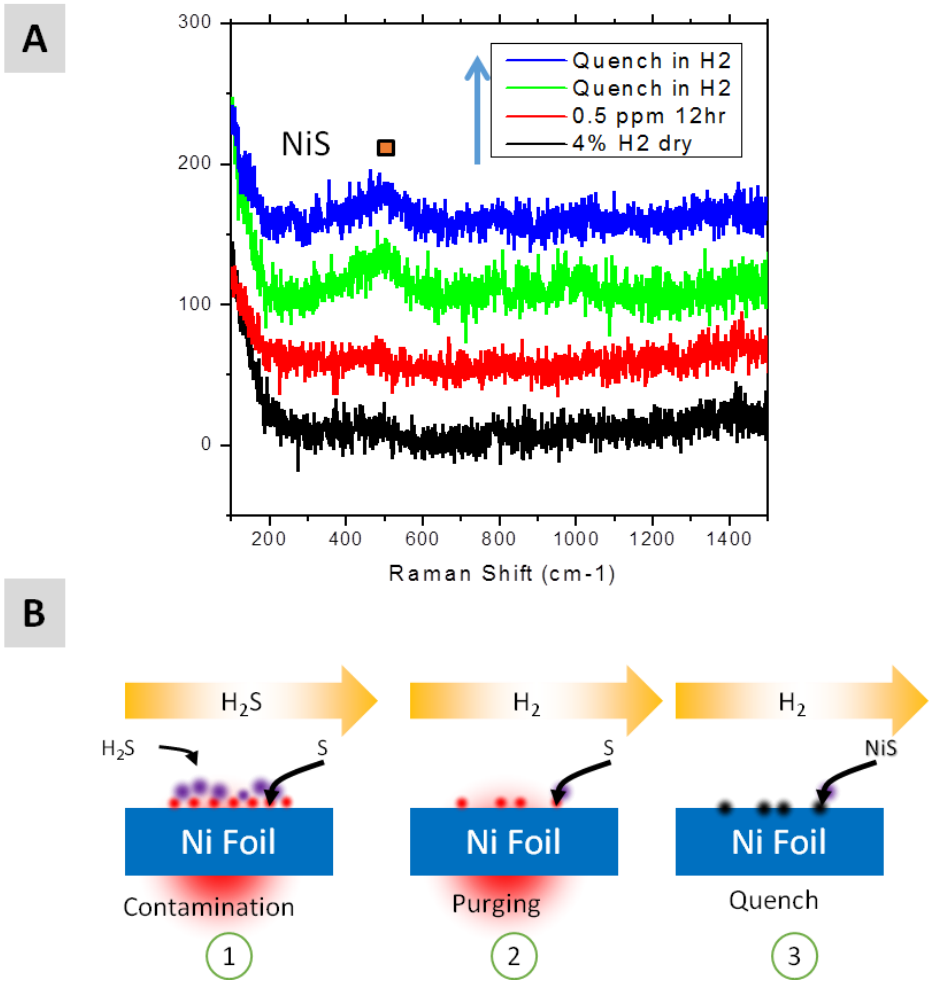

Figure 66: *In situ* SERS analysis of the Ni foil being exposed to H_2S.
(A) Raman spectra collected on nickel foil *in situ*, before and after exposure to 0.5ppm H_2S at 400°C, and after quenching while exposed to pure H_2. (B) The schematic showing the pathways of NiS, Ni_3S_4 and elemental sulfur formation.

6.3. Chapter Conclusions

Model cells with well defined Ni-electrolyte interfaces were investigated on their resistance to sulfur poisoning. Compare to Ni-YSZ cell, the Ni-BZCYYb cell exhibited tolerance to up to 5ppm H_2S. The Ni-BZCYYb TPB seems to be essential for the sulfur tolerance. Microscopic analysis showed that the Ni/YSZ interface seems to be particularly vulnerable to the attack of H_2S, resulting in deposition of nanoparticles on the Ni/YSZ boundary.

SERS enabled the detection of S contamination on the nickel surface, even after the exposure to extremely low level of H_2S. I*n situ* SERS analyses validated that the S adsorption at operating temperature turned into elemental sulfur, NiS and Ni_3S_4 when quenching the cells to room temperature.

Based on the key function of the triple phase boundary, some recommendations can be made to the fabrication and modification of the fuel cells. First, for the surface modification process to take full effect, the ultimate positions of the infiltrated catalyst need to be identified. Only when all the active TPB are protected, the sulfur tolerance can be achieved, as illustrated in Figure 67. In addition, except for surface infiltration, some other modification method should be considered. For example, heating the YSZ powders with BaO to introduce a very thin layer of $BaZrO_3$ on its surface, which could provide TPBs with inherent sulfur tolerance.

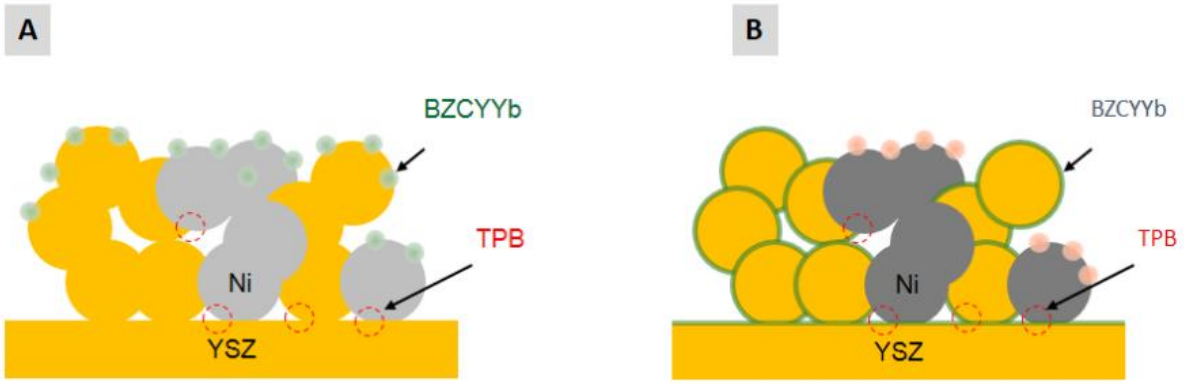

Figure 67: Importance of the locations of surface modification to the effect of sulfur tolerance.
(A) Non-uniformly distributed BZCYYb on Ni-YSZ offers limited S tolerance. (B) Fully enclosure of TPB by BZCYYb provides good protection.

CHAPTER 7: **OXYGEN REDUCTION ON LSCF CATHODE**

State-of-the-art SOFCs are operated at > 800^0C, which necessitates costly balance-of-plant materials and often results in degradation of key components over long term operation. Reducing SOFC operation temperature to intermediate range (500-750^0C) can provide considerable economic advantage on the SOFC technology. [20] However, SOFC performance decreases when temperature lowers, due to the reduced conductivity and electrochemical reaction kinetics. In particular, the oxygen reduction reaction (ORR) over the cathode surfaces is the bottleneck of power output at intermediate temperatures.[157] To develop new cathode materials or design novel cathode architecture that facilitates electrochemical oxygen reduction at intermediate temperatures remains a critical task for the development of IT-SOFCs.

To facilitate electrochemical reduction of oxygen, SOFC cathodes need to provide superior electronic conductivity, ionic conductivity and catalytic activity for oxygen exchange. $La_{1-x}Sr_xMnO_{3-\delta}$ (LSM) and $La_{0.6}Sr_{0.4}Co_{0.2}Fe_{0.8}O_{3-\delta}$ (LSCF) are two most commonly used cathode materials for SOFCs. Due to the flexibility in doping the perovskite-based cathode, a plethora of new cathode materials have been explored, and many of them, such as $Sm_{1-x}Sr_xCoO_3$ (SSC),[34] and $Ba_{0.5}Sr_{0.5}Co_{0.8}Fe_{0.2}O_{3-d}$ (BSCF),[35] providing significantly enhanced electrochemical performance at intermediate temperatures. However, integrating new cathode materials into the existing SOFC system usually results in stability concerns due to the unregistered chemical and mechanical compatibility with other SOFC components.

Surface modification of the conventional LSCF cathodes showed promises to enhance the cathode performance with little concern of degradation. Infiltrated surface catalysts, such as

doped ceria and $Sm_{1-x}Sr_xCoO_{3-\delta}$ (SSC) have demonstrated improvement in the oxygen reduction kinetics, [48, 49, 158] and the thin coating of manganate-based materials such as $La_{1-x}Sr_xMnO_{3-\delta}$ (LSM) and $Pr_{0.75}Sr_{0.2}MnO_{3-\delta}$ (PSM) showed enhanced long term stability in addition to performance enhancement.[159, 160] While the LSCF porous electrodes provided superior electronic and ionic conductivity, the surface modification catalysts help to improve the kinetics of oxygen exchange at LSCF surface. The synergy between the backbone and surface catalysts makes it possible to utilize ORR catalysts that may not have adequate conductivity as a stand-alone electrode material. In addition, the surface modification results in minimum impact on the physicochemical properties, microstructures and fabrication processes of the electrode backbone, and therefore avoided most compatibility issues.

In this study, we fabricated micro patterned electrodes with well defined geometry and tested them with micro-probe electrochemical impedance spectroscopy (EIS). The geometry dependence of the polarization resistances of the patterned electrodes was used to discriminate dominant paths for oxygen reduction, which is influenced by the type of cathode materials and electrode thicknesses. Change of intrinsic surface exchange kinetics of ORR was evaluated through application of surface catalysts (GDC, SSC and LSM) on LSCF patterned electrodes. The impact of catalyst loading amount and operation temperature on the ORR kinetics was further investigated.

7.1. Dominant Paths of Oxygen Reduction

Impedance spectra collected from the patterned electrodes with systematically varied sizes can distinguish different oxygen reduction paths. As shown in Figure 68, impedance

spectra were collected from the microelectrodes with well controlled sizes. A set of typical impedance spectra collected LSCF microelectrodes (100nm thick with various sizes) on a single electrolyte pellet tested under the 600^0C are shown in Figure 68B. The polarization resistances (R_p) of the patterned electrodes were extracted through equivalent circuit estimation, as detailed in Section 3.5.1 and Figure 29. By plotting Rp as a function of the electrode size (D) under logarithm scale, the data points fall into a line, the slope of which is recognized as the ORR path indicators (*n*). [113] If the oxygen reduction is rate-limited by a process happening on the TPB, Rp will be inversely proportional to the electrode size (D) and n=-1. On the other hand, if the ORR is controlled by a surface limited process, Rp will be inversely proportional to the area of the electrode (D^2), and n=-2. Typical scenarios for both rate-limiting modes are illustrated in Figure 68 (D, E). When the electrode has high ionic conductivity, the adsorbed oxygen ions can directly incorporate into the bulk of the electrode, and the oxygen reduction will be rate limited by a surface process. In contrast, if the electrode lacks sufficient conductivity for oxygen ions, only the triple phase boundary will be active for oxygen reduction, and the ORR will be controlled by TPB.

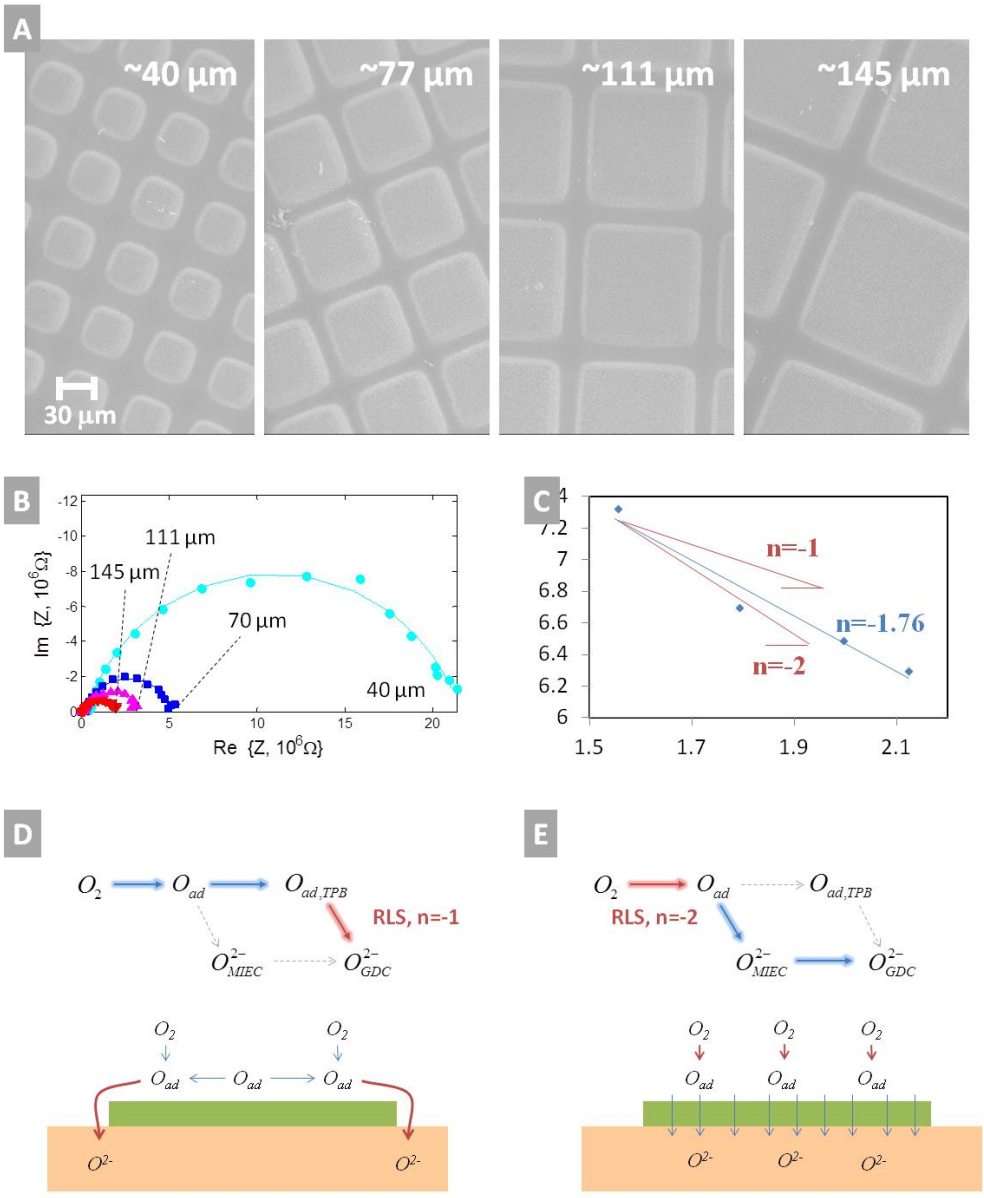

Figure 68: Investigation of the dominant ORR path through patterned electrodes with systematically varied sizes.
(A) SEM images of patterned electrodes of different sizes. (B) The impedance spectra of a typical set of LSCF electrodes (100nm thick) tested at 600^{0}C. (C) Plot of log(Rp/ohm) as a function of log (d/µm), with the slope defined as ORR path indicator (*n*). (D) Schematics of a typical TPB controlled ORR path (n=-1) and a typical surface controlled ORR path (n=-2).

LSM and LSCF patterned electrodes show different ORR paths. As displayed in Figure 69, the LSM and LSCF electrodes of a same thickness of 100nm were tested with the microprobe

impedance station to obtain their ORR path indicators (n) at different temperatures. Each value of *n* listed in Figure 69 (A) is generated by measuring impedance spectra of electrodes of four different sizes and plotting them with respect to electrode size, as demonstrated in Figure 69 (B, C). The values of path indicator (n) of LSM electrodes are close to -1, while those of LSCF are close -2. These observations suggest that the ORR path of LSCF is dominated by its surfaces, while that of LSM is dominated by the TPBs. The discrepancy is originated from the ionic conductivities of these two materials. High ionic conductivity of LSCF makes a facile path for the adsorbed oxygen ion to incorporate into the LSCF lattice and then incorporate into the electrolyte, while for LSM, due to its lower ionic conductivity, the oxygen ion exchange happens mainly on the triple phase boundary. [161] As a further proof of this mechanistic interpretation, the path indicators for both materials move closer to -2 as temperature rises, indicating stronger oxygen flux through surface controlled path, as a result of the increased ionic conductivity, as shown in (Figure 69A).

Besides the difference in material properties, the electrode thickness also shows significant impact in the dominant paths of oxygen reduction. As shown in Figure 70, the value of ORR path indicators (*n*) of LSCF electrodes deviated from -2 as the thickness increases. Since thicker LSCF electrodes impose higher resistance for oxygen ions to penetrate through the LSCF film and reach the GDC electrolyte, the TPB makes more contribution to the ORR process, shifting the path indicator closer to -1. The 50nm patterned electrodes showed surface dominant oxygen reduction paths for all tested temperatures from 500^0C to 650^0C, making an ideal platform for the study of intrinsic kinetics of oxygen exchange on the LSCF surfaces.

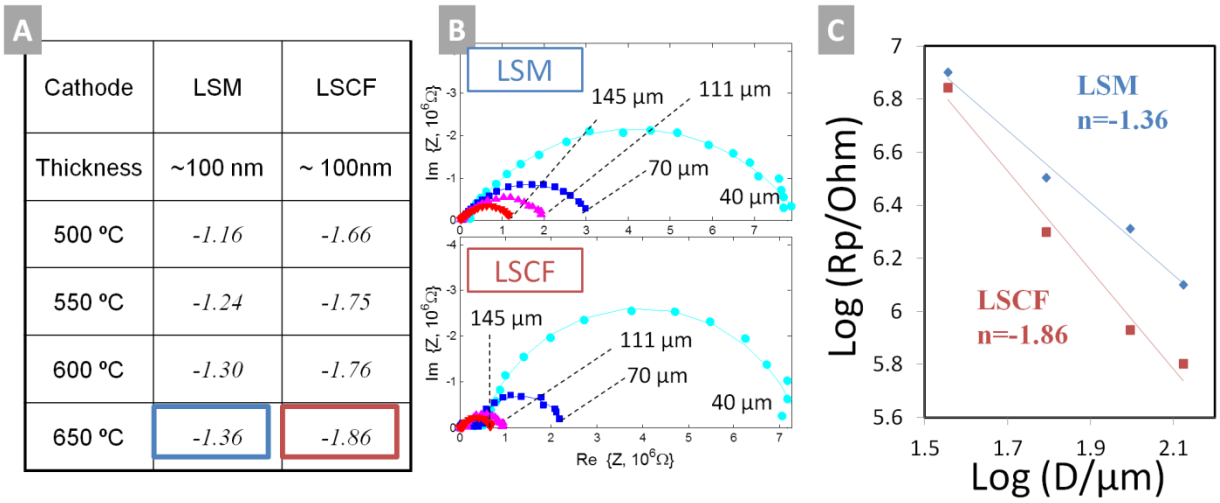

Cathode	LSM	LSCF
Thickness	~100 nm	~ 100nm
500 °C	*-1.16*	*-1.66*
550 °C	*-1.24*	*-1.75*
600 °C	*-1.30*	*-1.76*
650 °C	*-1.36*	*-1.86*

Figure 69: Estimation of dominant ORR paths on LSM and LSCF patterned electrodes.
(A) ORR path indicators (*n*) of LSM and LSCF patterned electrodes (with thickness of 100nm) under different testing temperatures. (B) Impedance spectra of LSM and LSCF of a set of different sizes (~40, 77, 111 and 145 µm) tested in the highlighted conditions. (C) Plot of log(Rp/ohm) as a function of log (D/ µm), with the slope defined as ORR path indicators (*n*). Comparison of Rp values between electrodes of different materials is not recommended since they are fabricated and tested on separate substrates.

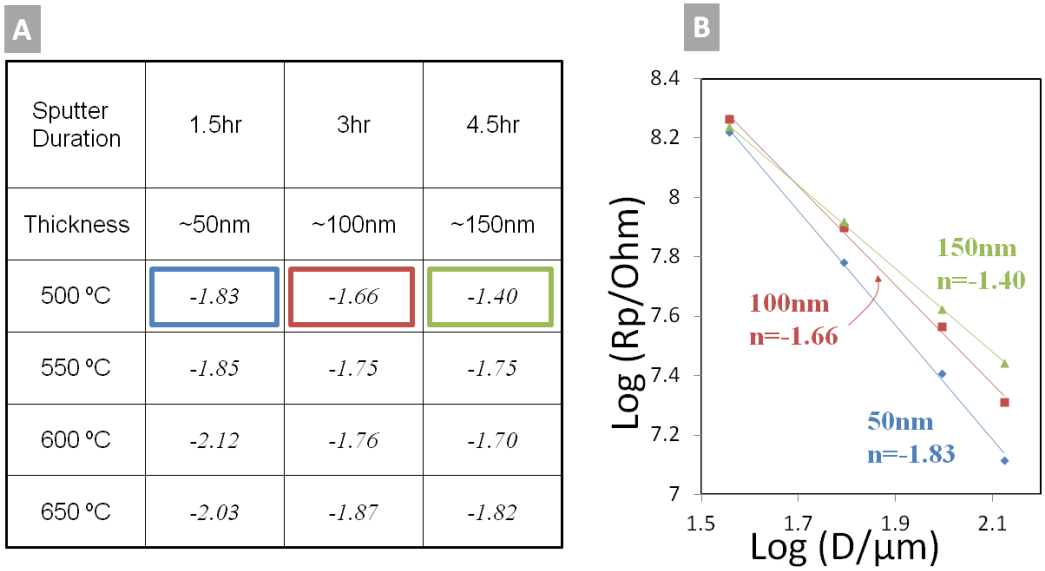

Sputter Duration	1.5hr	3hr	4.5hr
Thickness	~50nm	~100nm	~150nm
500 °C	*-1.83*	*-1.66*	*-1.40*
550 °C	*-1.85*	*-1.75*	*-1.75*
600 °C	*-2.12*	*-1.76*	*-1.70*
650 °C	*-2.03*	*-1.87*	*-1.82*

Figure 70: Estimation of the dominant oxygen reduction paths of LSCF patterned electrodes of different thicknesses.
(A) ORR path indicators (*n*) for LSCF patterned electrodes with different thicknesses. (B) Impedance spectra of LSCF electrodes plotted as a function of electrode size under logarithm scale, with the slope defined as ORR path indicator (*n*). Comparison of Rp values between electrodes of different thicknesses is not recommended since they are fabricated and tested on separate substrates.

7.2. Impact of Surface Modification

To enhance the oxygen exchange catalytic activity of LSCF cathode, different catalysts, including GDC, SSC, and LSM, were employed onto the 50nm thick LSCF pattern electrode to modify the LSCF electrode.. To evaluate the effect of different modification materials, two arrays of LSCF patterned electrodes, with and without modification, respectively, were fabricated on the same GDC substrate, as illustrated in Figure 71(A). Such side-by-side design excluded the difference from substrate preparation. Microelectrodes of both arrays are of the same sizes. Polarization resistances of the patterned electrodes with and without surface modification were measured by micro-probe EIS station at the same temperature. 3 electrodes on each array were tested while the spectra. Figure 71 (B-D) displays impedance spectra of the LSCF electrodes before and after surface modification with GDC, SSC and LSM, respectively. The GDC modification showed ~ 50% reduction in the R_p, suggesting significant improvement in the oxygen exchange capability on the electrode surface. The LSM modification increased the R_p by 10%. As previously reported, LSM modification improves the cathode performance only after activation with cathodic bias, while the initial polarization resistance under OCV is larger than that of the blank LSCF. [159] Although SSC has shown excellent performance as the standing alone cathode material,[162] the LSCF electrodes modified by SSC showed only slight improvement of ORR activity.

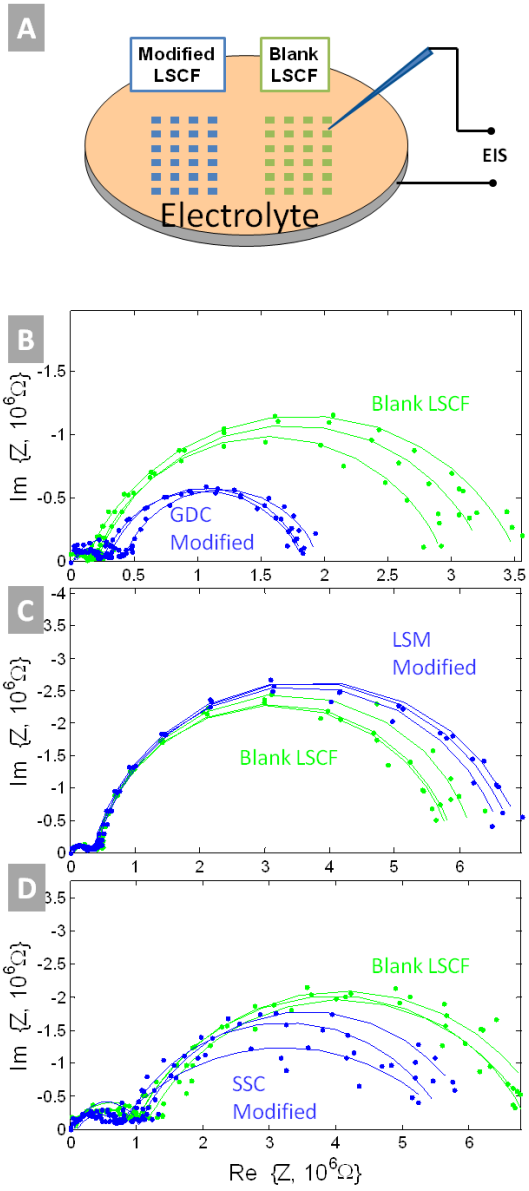

Figure 71: Impact of surface modification on the ORR activity of LSCF patterned electrodes.
(A) Schematic of modified and blank LSCF patterned electrodes fabricated on the same electrolyte substrate. (B) GDC modification of LSCF electrode (D=~77um) through sputtering deposition for 5 mins (C) LSM modification of LSCF electrode (D=~40um) through sputtering deposition for 5 mins (D) SSC modification of LSCF electrode (D=~77um) through sputtering deposition for 5 mins. Rp of blank LSCF electrodes between different samples are not comparable due to difference in substrate conditions and electrode sizes. All LSCF electrodes have thickness of 50nm and impedance spectroscopy conducted at ~650°C.

Under the testing condition, the bulk pathway of oxygen transfer through LSCF electrodes is open, making the adsorbed oxygen species on LSCF readily participate the electrochemical oxygen reduction. A good surface modification requires high adsorption of oxygen and facile diffusion of the adsorbed oxygen to the surface of LSCF. The LSM has high adsorption energy of oxygen, but due to its high diffusion barrier, the adsorbed oxygen cannot go to the LSCF surface. The SSC offers facile oxygen transport, but due to the low oxygen adsorption capability, it does not make significant improvement to the ORR process. In fact, among the perovskite-based mixed ionic and electronic conductors, higher driving force for oxygen adsorption usually accompanies higher energy barrier for oxygen diffusion.[163] CeO_2 surface with oxygen vacancies assumes strong adsorption of oxygen, [164] [165] and meanwhile, the bulk of doped ceria shows a much lower ionic conductivity. [166, 167]These properties of doped ceria corroborated the superior enhancement capability of GDC when it is placed on the surface of LSCF.

The effect of GDC modification to improve oxygen exchange activity on LSCF was further scrutinized to gain insight of mechanisms. LSCF electrodes with different GDC loading were compared by putting the GDC modified LSCF side-by-side pristine LSCF electrodes. Shown in Figure 72(A) are the SEM images of the surfaces of LSCF patterned electrodes after GDC deposition with different loading amounts. On the densely packed LSCF grains, GDC catalysts appear to be nanoparticles. As the deposition time increases, GDC covers more area of LSCF surface, until a full encapsulation is reached with 10 min sputtering. The effect of GDC deposition time was characterized by micro-probe EIS at 650^0C, as displayed in Figure 72(B). All modified electrodes showed improvement in electrochemical performance, while 5 min deposition appeared to be optimal. In addition, the enhancement of surface ORR activity by

GDC modification is more prominent at high temperatures. As shown in Figure 72 (C), the percentage of Rp decrease through GDC modification becomes less significant as the temperature decreases. The change of activation energy also suggested that GDC changed the surface ORR kinetics of LSCF.

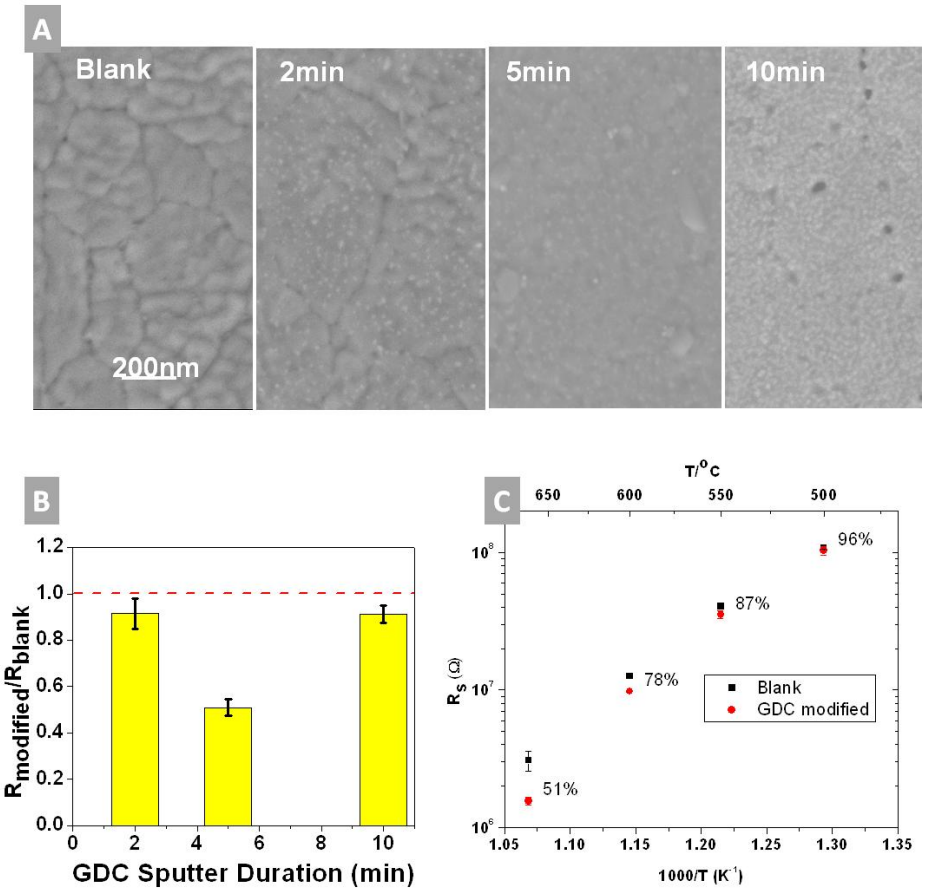

Figure 72: Impact of GDC modification on ORR rate of LSCF.
(A) Surface SEM images of LSCF electrodes before and after GDC modification through sputtering for different durations (B) Normalized polarization resistances of the LSCF patterned electrodes as a function of deposition amount of GDC modification (C) Polarization resistances of pristine and GDC modified LSCF patterned electrodes (with 5 min sputtering duration) at various temperatures.

The systematic study of GDC modification implies that GDC nanoparticles form hotspots for oxygen exchange through enhancement of oxygen adsorption and facile delievery to LSCF

surface as illustrated in Figure 72 (D). Since the rate limiting step of ORR on the LSCF patterned electrodes is the oxygen surface exchange, GDC catalyst readily facilitate this process, resulting in reduction of Rp. Such enhancement, are more prominent when oxygen exchange in GDC is activated, which occurs at higher temperatures. Appropriate loading of GDC is critical for the enhancement of oxygen reduction kinetics. Since doped ceria has limited electronic conductivity, continuous GDC coating would pose additional resistance for the electrochemical reduction of oxygen, offsetting the benefit of surface modification.

7.3. Chapter Conclusions

Patterned electrodes with controlled sizes and thickness are shown to be effective in discriminating the dominant paths of oxygen reduction. While the surface controlled ORR path is more prominent on LSCF electrodes, TPB controlled path dominates the LSM electrodes, mainly due to their differences in ionic conductivity. Higher testing temperatures and lower electrode thicknesses also activate more surface areas for oxygen reduction, moving the dominant path to the surface controlled mode. GDC, LSM and SSC modified LSCF electrodes were tested against the blank LSCF electrodes, and GDC showed the most prominent decrease of polarization resistance for a 50nm thick LSCF electrode. The systematic study of GDC modification by varying the deposition amount and the testing temperatures implied that GDC formed hotspots for oxygen reduction on LSCF surface. This study demonstrated an effective approach to study intrinsic surface properties of SOFC cathode materials, which could guide the rational choice of surface catalyst materials and knowledge-based design of novel microstructures to improve the performance of SOFC cathodes and other ORR catalysts.

CHAPTER 8: SURFACE DEGRADATION OF LSCF CATHODE

Long term stability is another challenge for the conventional cathode materials used in SOFC. In particular, LSCF electrode showed steady degradation over the long term operation.[55] The degradation of LSCF has been related to the exposure to CO_2, H_2O and Cr containing species, which forms contamination species that slows down the electrochemical processes. [168-171] In addition, cation segregation, e.g., La_2O_3, SrO, Co_3O_4 and Fe_2O_3, are also correlated with the cause of performance degradation. [170, 172] It is critical to identify the degradation modes of the LSCF electrode, so as to design appropriate coating or modification for its alleviation. However, characterization of the surface species and incipient phases related to LSCF degradation is non-trivial, due to the low concentration of these species.

In this chapter, surface enhanced Raman spectroscopy is utilized to unravel the secondary phases formed on LSCF cathode surface after long term degradation tests. With the enhanced sensitivity towards species present in trace amount, the identification of surface degradation phase is facilitated. In addition, the SERS technique allows for mapping of degradation species across the heterogeneous interfaces, providing insight of the critical locations where degradation occurs.

8.1. Analysis of Surface Modified LSCF Cathode

SERS technique can enhance the signal of the perovskite based cathode materials, which has inherent low intensity. The SERS application on cathode materials is displayed in Figure 73. The Raman spectra collected from both LSCF powders and LSM thin film were significantly

enhanced after SERS conditioning. It is worth noting that the normal Raman signal of both materials was very weak, because LSCF and LSM belong to the $R\bar{3}c$ and Pbmn space groups, respectively[173, 174], which represents near-cubic perovskite phases that has little Raman activity. As shown in Figure 73 (A), the normal Raman of prestine LSCF pellets showed three strong modes (180, 320 and 720 cm^{-1}) and three weak modes (540, 950 and 1130 cm^{-1}) within the inspection range. After applying Ag nanoparticles, all Raman modes were enhanced by ~100 times. The relative peak intensity changed, but no new peaks were observed. It suggests that the Ag nanoparticles effectively enhanced the Raman signal. Since Ag particles per se have no active Raman modes, it does not introduce any extra peaks to the Raman spectrum.

The surface specificity of SERS was demonstrated by the LSM thin film sputtered on YSZ substrate. As shown in Figure 73(B), the normal Raman spectrum shows both LSM and YSZ peaks, because signal was detected from underneath the film since the LSM film was only 100 nm thick. YSZ is much more Raman-active than LSM, so the YSZ peak was stronger than that of LSM even though the source of the signal was buried. After the silver nanoparticles were applied, the LSM peaks significantly grew in size, while the intensity of YSZ remained roughly the same. Therefore, the Ag treatment granted some level of surface specificity to the Raman analysis since only the signal from the thin film was visibly enhanced. This feature can provide a capability to detect phase evolution on the cathode surface with superior surface sensitivity, potentially contributing to studies on cathode degradation.

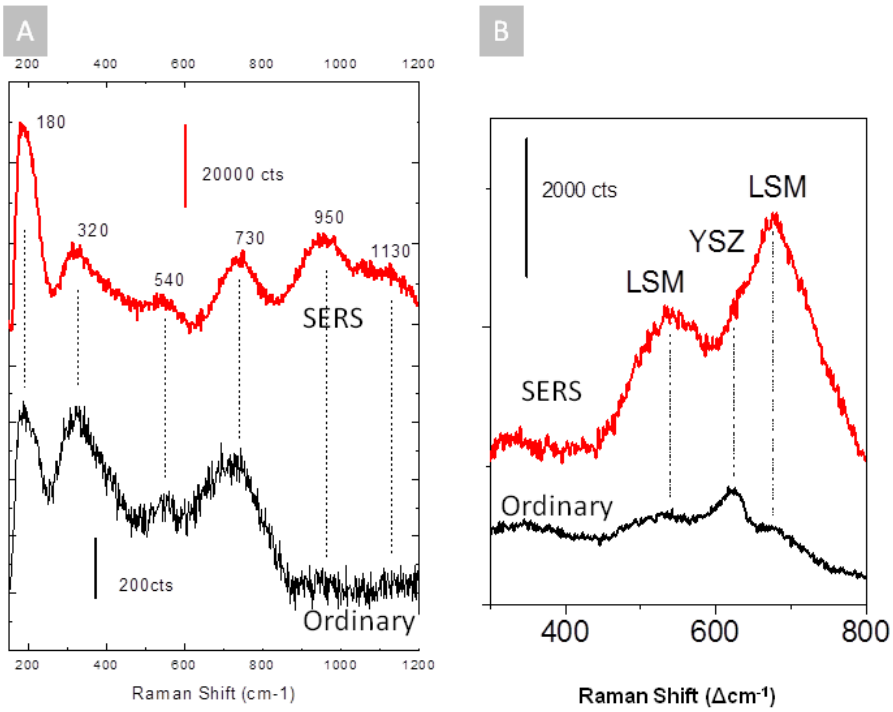

Figure 73: SERS capability for the analysis of cathode materials.
The normal Raman and SERS spectra collected from (A) Pressed LSCF powders, and (B) LSM film sputtered on a YSZ pellet. Argon laser emission lines at 514 nm were used for excitation of Raman signal in this study.

The unique sensitivity of SERS towards surface species allows for identification of surface modification.In order to enhance oxygen reduction activity and stability of LSCF porous electrode, other perovskites, such as Pr(Ni, Mn)O_3 (PNM), (L,aSr)MnO_3 (LSM) and $PrMnO_3$ (PM).[159, 160] As shown in Figure 74, the surface modification layer, despite the low concentration, manifested prominent spectral feature under SERS analysis. The LSCF alone, does not show strong stretching modes, since it belongs to R$\bar{3}$c structure, which has higher crystal symmetry. The bands around 550 cm^{-1} and 660 cm^{-1}, are assigned to the antisymmetric stretching (AS) and symmetric stretching (SS) modes, respectively, of Pbmn structure. The Pbmn structure, which has lower symmetry than R3c, is characteristic of the perovskites with Mn

occupying the B sites. The change of the AS mode, on the other hand, is influenced by the doping of the host lattice by other cations. [175]

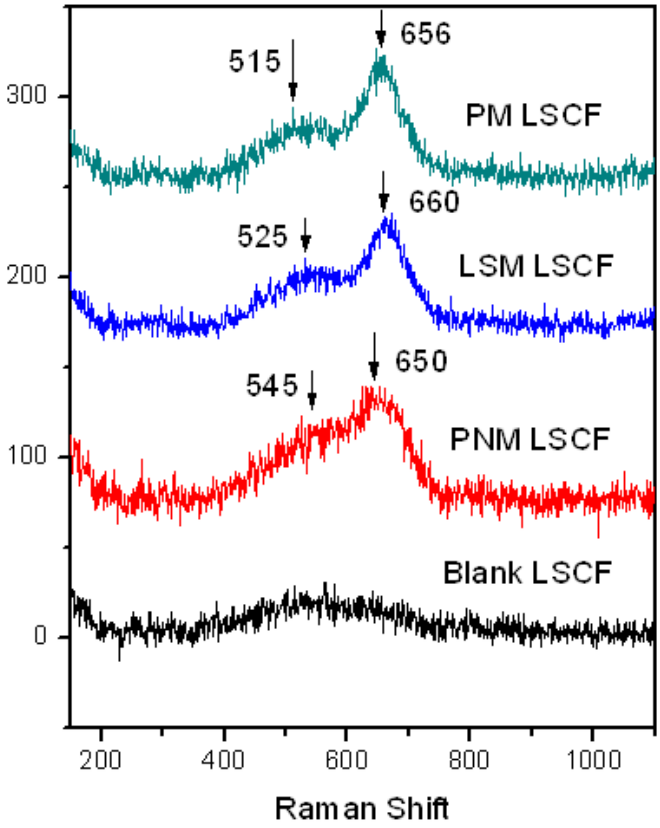

Figure 74: SERS analysis of cathode infiltration.
The surface enhanced Raman spectroscopy study of porous LSCF electrodes after surface modification with Pr(Ni, Mn)O_3 (PNM), (L,aSr)MnO_3 (LSM) and $PrMnO_3$ (PM). Argon laser emission lines at 514 nm were used for excitation of Raman signal in this study.

8.2. Analysis of LSCF Surface Degradation over Long Term Operation

The Raman signature introduced by lattice distortion also finds its utilization in characterization of LSCF cathode degradation. The LSCF powders were pressed into pellets, fired at 1080^0C for 10 hrs. The pellets were then annealed in a variety of atmospheres, including

pure Ar, 1% O_2, pure O_2, 1% CO_2 and 3% H_2O. To activate the LSCF pellets for SERS, the samples loaded on glass slides were deposited with a thin layer of silver nanoparticles (180 seconds at 8W).

The LSCF pellets annealed under moderate atmospheres were inspected by both Raman and SERS technique. The normal spectra (not presented) of the samples showed no notable difference. Presented in Figure 75 are the SERS enhanced spectra and their differential spectra with respect to the pristine LSCF sample. Even with the enhancement given by Ag nanoparticles, the difference in the Raman signals of the LSCF samples annealed under various atmospheres was not easily identifiable. To visualize the difference, the SERS spectrum of pristine LSCF sample was subtracted from all sample spectra. As displayed in Figure 75, the annealing in Ar, 1% O_2 and pure O_2 did not result in any identifiable change on the LSCF surface. However, the LSCF sample annealed in 1% CO_2 and 3% H_2O showed slight increase in the 500-600 cm^{-1} range. According to the previous studies, the emerging of Raman modes in this range indicates the formation of Pbmn phase. [175]

The observed formation of Pbmn phase can be related to the surface SrO segregation upon the exposure to H_2O and CO_2 containing atmospheres. Since SrO itself possess no active Raman mode, the segregation is identified indirectly. LSCF is based on LaFeO3 perovskite structure. At low Sr content, LaFeO3 assumes orthorhombic structure (Pbnm), while at high Sr content, it is transferred to rhombohedral structure ($R\bar{3}c$), according to the XRD analysis of the bulk samples by Tai et al.[176] The main peaks of LSCF (310, 540, 720 cm^{-1}) are associated with the r3c structure, since the prestine LSCF with and without SERS both possess these peaks. The emerging of small humps around 500-600 cm^{-1} both suggest that orthorhombic phases are

formed after annealing in H_2O and CO_2. The formation orthorhombic phase occurs in LSCF when Sr is removed from the perovskite lattice, which indicates SrO segregation. [177]

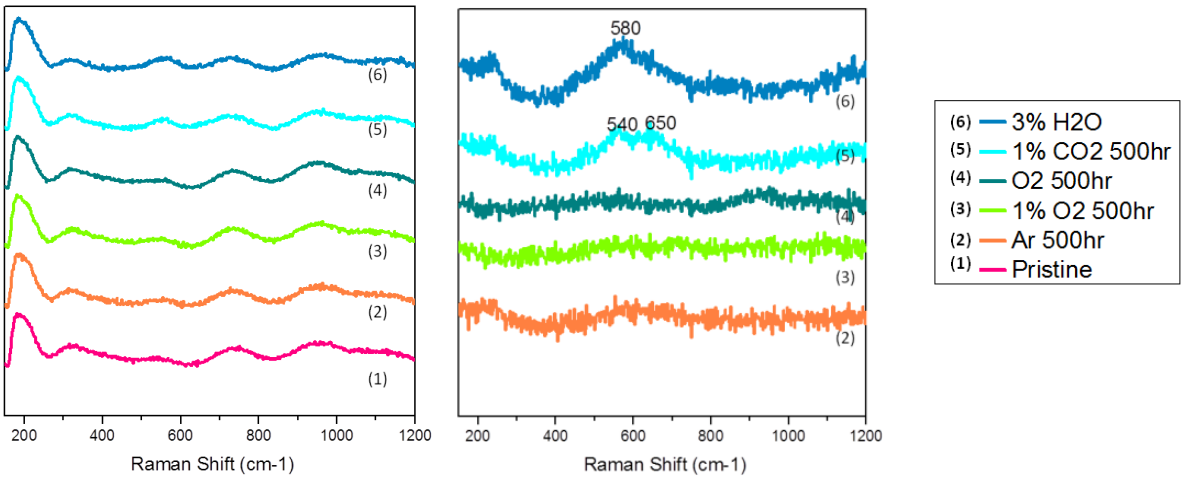

Figure 75: SERS analysis of the LSCF pellets undergone thermal treatments in different atmospheres. (A) SERS spectra and (B) Differential analysis of the SERS spectra with respect to the prestine condition.

8.3. Study of Cr Poisoning on LSCF Surface

SERS probes also find utility in detection of Cr poisoning on the LSCF electrodes which are present in trace amount. By putting Cr alloy in physical contact with LSCF porous electrode, strong Cr poisoning is observed, and the degree of poisoning scales with the concentration of steam, as presented in Figure 76. Different water concentrations: 3%, 5% and 10%, were used when the sample were heat treated under 750^0C for 66hrs. As the water concentration increased, an obvious growth of the signal intensity of SrCrO4 was also observed. The 3% H_2O + Cr treated sample yielded a CrO_4^{2-} peak of ~ 500 cts; the 5% H_2O + Cr sample showed ~2000 cts; the chromate in 10% H_2O + Cr sample amounts for ~4500 cts. As the SERS enhancement factor is uniform on different regions of the sample, and each SERS spectra line is the average of

signals collected from 10 spots, the intensities of SERS signal represent the quantity of CrO_4^{2-} species on the topmost layer of LSCF electrode.

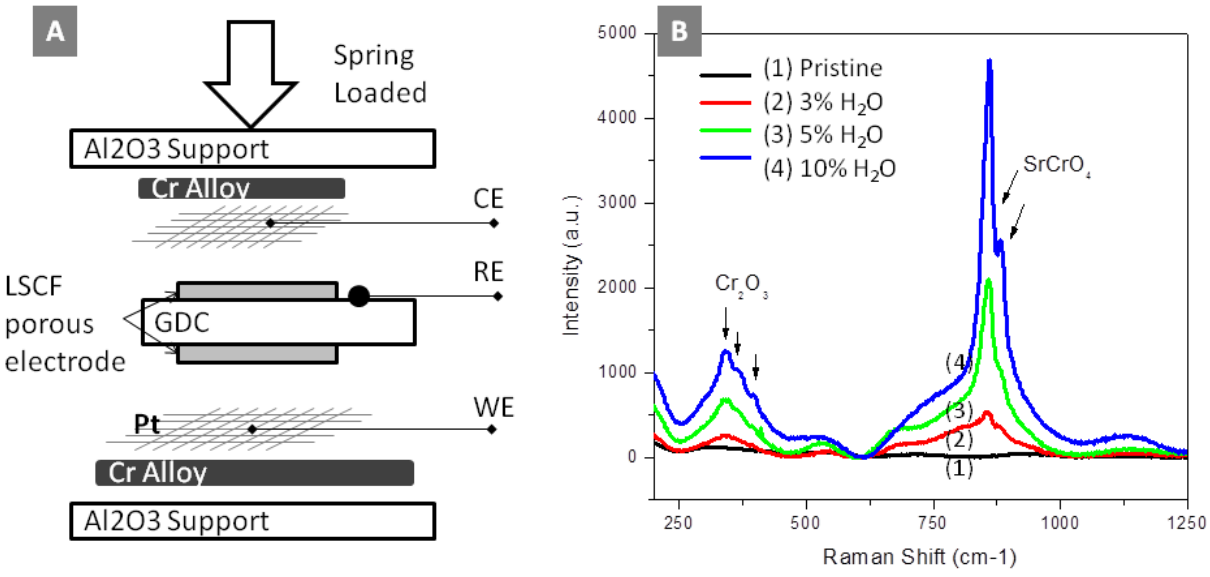

Figure 76: Impact of water concentration on Cr poisoning of LSCF porous electrodes.
(A) A scheme of the Cr poisoning test. (B) SERS analysis of the LSCF porous electrode in touch with the Cr alloy under atmospheres with different H_2O concentration.

Even without direct contact with Cr source, the LSCF porous electrode showed evidence of Cr deposition, through SERS analysis displayed in Figure 77. On the sample treated with dry air, the working electrode showed a significant peak at 860 cm^{-1} related to the formation of $CrO4^2$. The counter electrode on the same sample, showed only a slight signal at 840 cm^{-1}, which is also a CrO4 related band. The 1060 cm^{-1} peak, on the other hand, remains the similar size. On the WE of the sample treated with wet air, the Raman peak at 860 cm^{-1} is significantly stronger than that on the WE treated with dry air. While on the CE of the H_2O treated sample, the $CrO4^{2-}$ related peaks appear at 840 and 860 cm^{-1}, suggesting fine difference of chromate phases evolved on the surface.

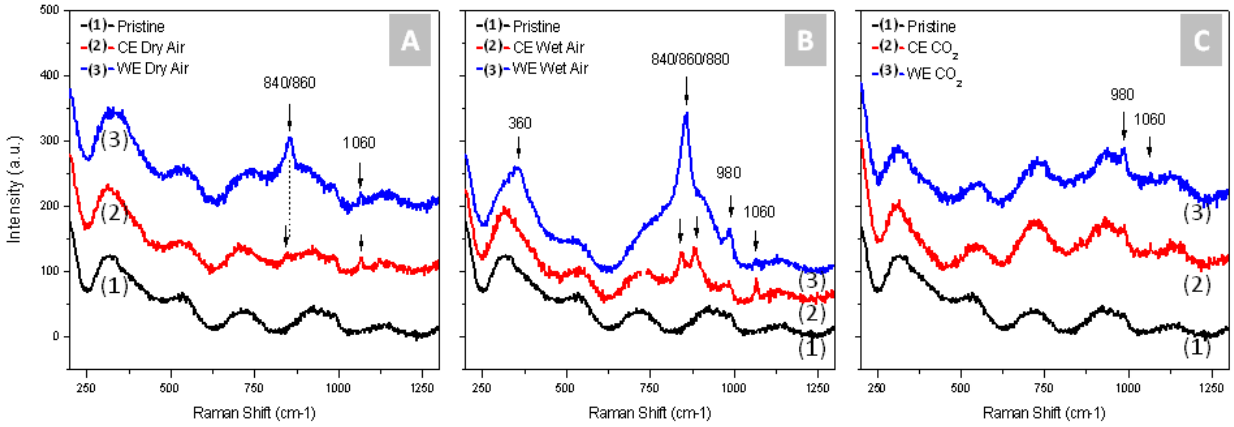

Figure 77: SERS spectra of the porous LSCF electrodes after long term operation without direct Cr source. Porous electrodes tested in dry air (A) and wet air (B) under polarizations. WE (working electrode) is biased with negative potential (cathodic bias), while CE (counter electrode) is biased with positive potential. ~10 data points were collected and taken average. The excitation laser was 514nm at a power of 15mW.

To rule out the possibility of artifacts from the spectral features observed in in Figure 77, contolled experiments were conducted. Displayed in Figure 78 are the Raman and SERS spectra of LSCF porous electrode in pristine condition and after polarization tests in wet air. Figure 78 (A) showed the two samples inspected by ordinary Raman with extra long collection times. The laser rastered 700 points across each of the sample surfaces, yielding a total collection time of 7000 s. The extended scan of ordinary Raman did not produce any distinguishable features between the two samples. SERS was introduced, with Ag sputtered on the samples with optimized amount (Figure 78 B) and with more Ag sputtered than required for optimal condition (Figure 78 C). Under both SERS conditions, the pristine sample showed no features other than the broad bands related to LSCF, suggesting that Ag sputtering is not introducing contamination to the sample surface. In contrast, on the wet air treated porous LSCF sample, the optimized SERS condition resulted in prominent signals associated with degradation products. While more

Ag deposition did not change the peak positions, it degraded the signal intensity. These results suggested that the signal observed with SERS analysis is not artifacts generated by Ag sputtering. More importantly, the advantage of SERS is unique, and cannot be replaced by extention of the collection time within a reasonable range.

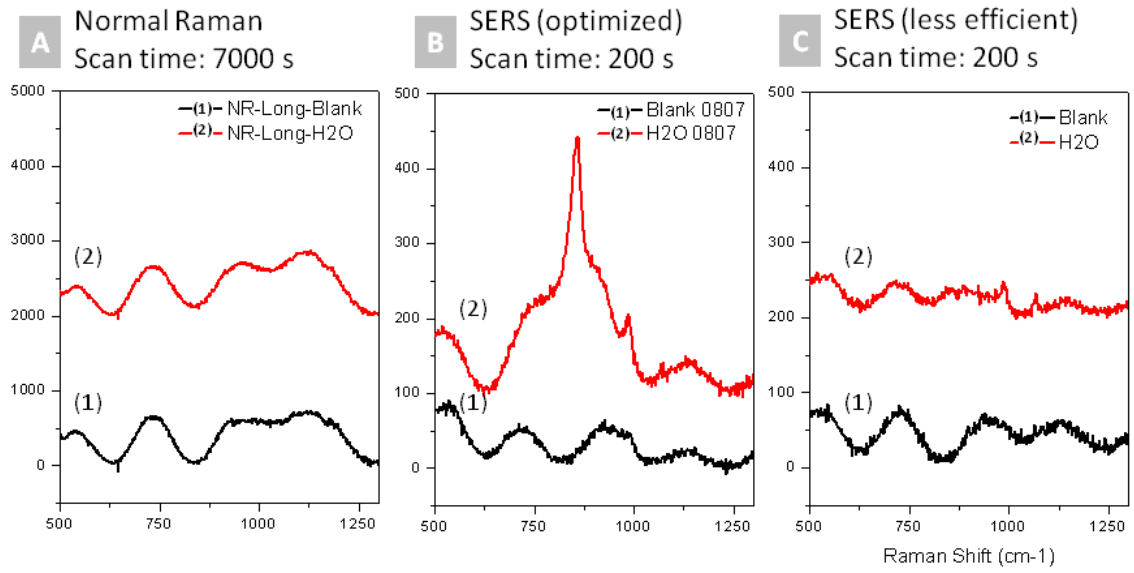

Figure 78: Ordinary Raman and SERS analysis of trace amount of Cr poisoning on porous LSCF.
LSCF electrodes in pristine condition and after polarization test in wet air with indirect source of Cr. (A) Normal Raman with a total collection time of 7000 secs. (B) SERS with more Ag sputtered than that required for optimal SERS. (C) SERS with optimized Ag sputtering parameters.

Severe Cr poisoning causes surface roughening, but when the degree is low, it may not be noticeable under SEM analysis. Impact of Cr poisoning on the morphology of LSCF porous electrodes was studied with SEM; in addition, the distribution of the contaminating elements was analyzed by electron dispersive X-ray (EDX). Shown in Figure 79 are the micrographs of LSCF porous electrodes tested in contact with Cr alloy foils, under different water concentrations at 750°C. Rough morphology was observed on the LSCF sample put in direct contact with Cr

sources, and the degree of roughening increases with the concentration of steam. The LSCF electrode tested in wet air showed no surface roughening at all, even though Cr deposition was identified by SERS.

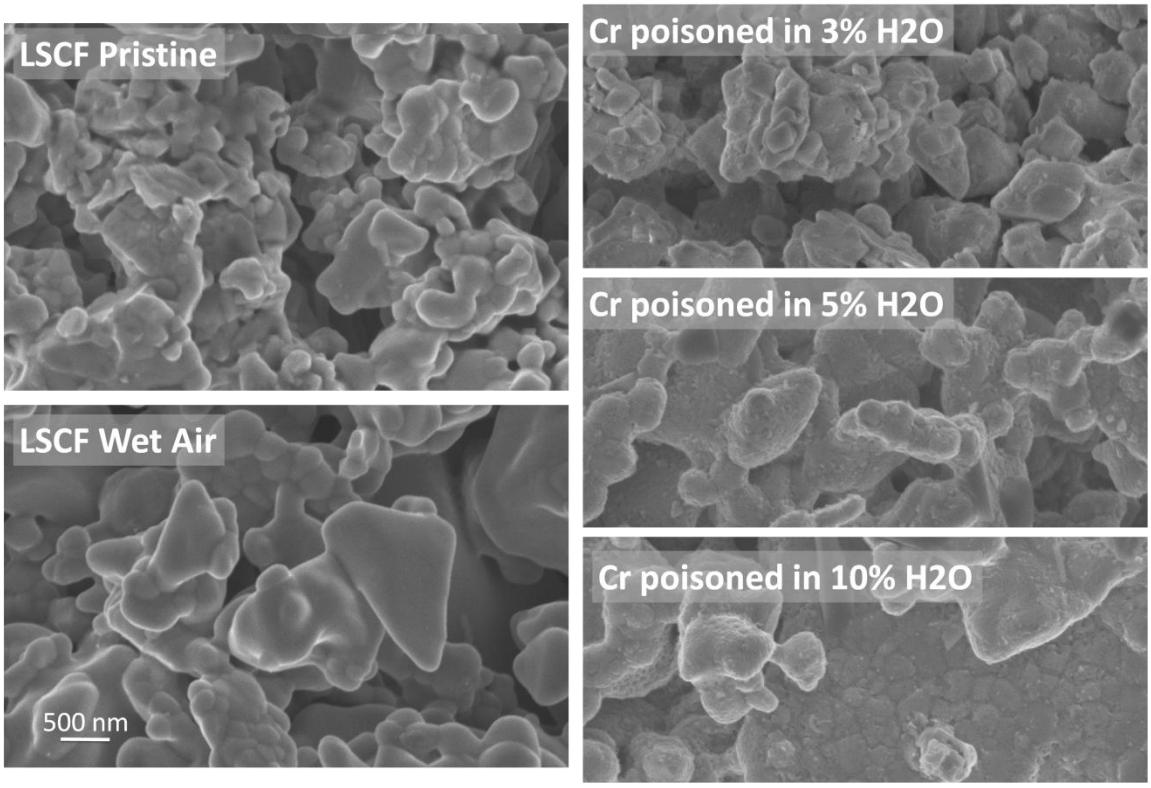

Figure 79: SEM Images of LSCF porous electrodes after testing under different gas atmospheres.

EDX do not offer comparable sensitivity towards Cr poisoning. EDX analysis validated the presence of Cr element on the LSCF surface, as displayed in Figure 80. The characteristic peaks at 5.41 keV and 5.94 keV can be assigned to the kα1 and kβ lines of the Cr element, respectively. Mapping of the Cr element on the sample tested under 10% H_2O, however, did not show significant correlation between the Cr amount and the surface morphology. It is likely that the Cr contamination formed the rough feature on the LSCF grains, which uniformed distributed across the top surface of the electrode. Quantitative analysis of the Cr concentration on the

LSCF samples poisoned at different H_2O concentration was also attempted with EDX analysis. However, the data showed poor correlation with the H_2O concentration. In realization of the limited capability of the EDX analysis for the mapping of trace amount of contaminating elements, we opted to SERS to secure the distribution of the Cr.

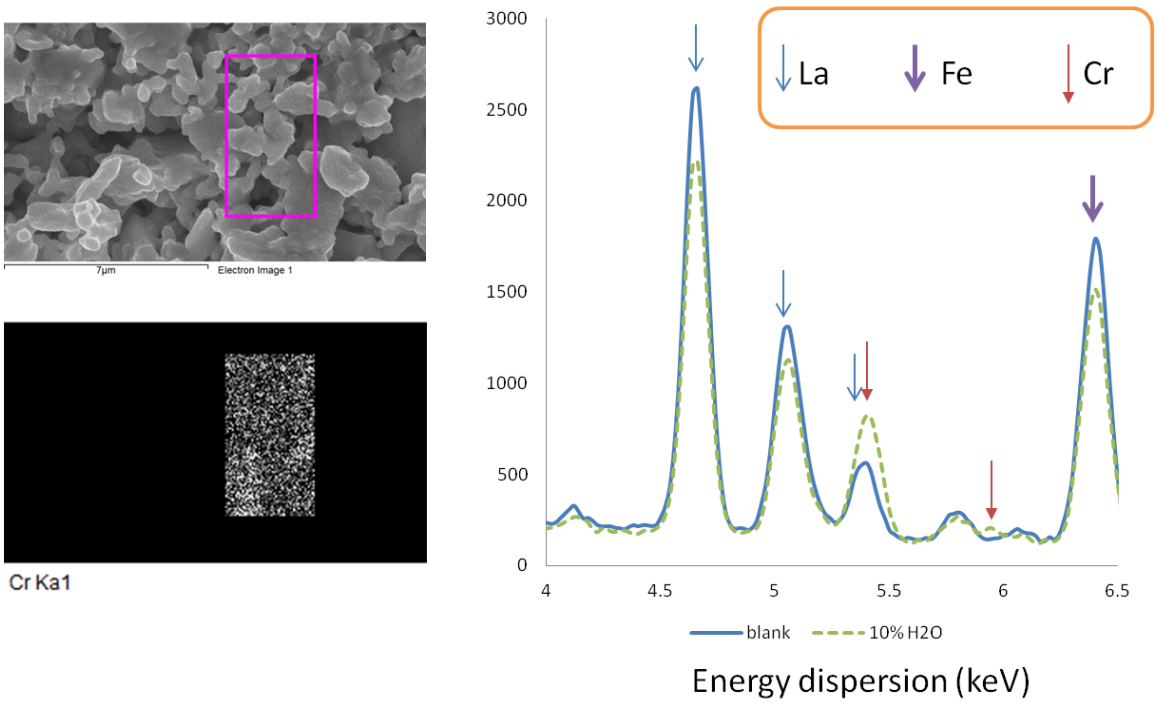

Figure 80: EDS analysis of LSCF porous electrode after Cr poisoning.
Porous LSCF electrodes tested under 10% H_2O containing air. (A) SEM micrograph with the mapping of Cr element on the top surface. (B) The EDS spectrum analysis of the scanned region.

SERS allowed for fast mapping of the locations of Cr deposition on the LSCF-GDC interface, providing insight into the impact of Cr poisoning on electrochemical performances. To validate this hypothesis, model cells with patterened LSCF electrodes were fabricated and tested in an in-situ Raman chamber at 550°C with 3% water carried in air, as shown in Figure 81. The in-situ Raman on the patterned LSCF electrodes showed no significant feature related to Cr

deposition. However, the evidence of Cr poisoning manifested after SERS agents are applied. SERS mapping was conducted over a region covering one LSCF electrode with electrical bias and one without. The intensities of the peaks related to GDC (465 cm^{-1}) and LSCF (670 cm^{-1}) are consistent with the locations of the patterned LSCF electrodes. The peak at 860 cm^{-1}, which corresponds to the deposition of $SrCrO_4$, concentrates on the LSCF-GDC interfaces. In contrary to our finding, previous research of Cr poisoning of SOFC cathodes indicated that $SrCrO_4$ formed on the surface of LSCF rather than at the LSCF-GDC boundary.[168, 178] This inconsistency demands further research. The electrical bias has no preferential effect on the formation of $SrCrO_4$, which agrees with the previous report.[168] The deposition of $SrCrO_4$ on the LSCF boundary offered a new insight into the Cr poisoning of the LSCF electrodes: $SrCrO_4$ could block the active sites for oxygen reduction on the triple phase boundary.

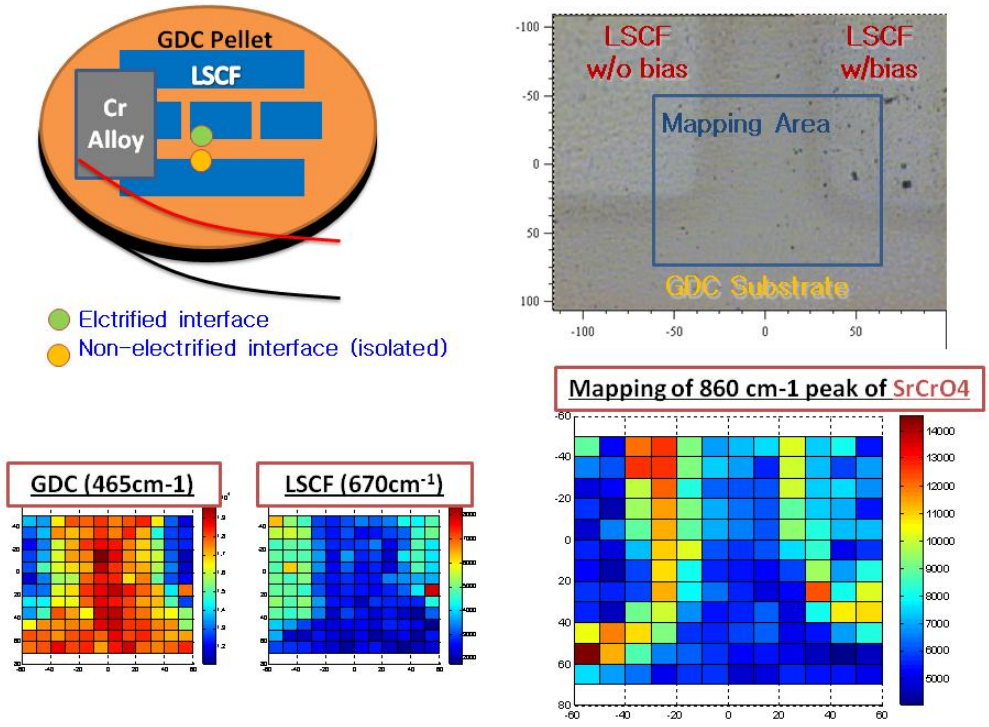

Figure 81: SERS mapping of the LSCF electrodes after Cr poisoning.
Model cells with patterned LSCF electrodes tested with Crofer 22 APU alloy at 600°C for 12 hrs with 3% H2O containing air.

In addition, the surface modification of LSCF porous electrode was found to provide resistance to Cr poisoning. In order to mitigate Cr poisoning, two compositions were explored as surface modifiers: $La_{0.8}Ca_{0.2}Ni_{0.4}Fe_{0.6}O_{3-\delta}$ (LCNF) and $La_{0.8}Ca_{0.2}FeO_{3-\delta}$ (LCF). Stoichiometric amounts of metal nitrates were dissolved in a mixture of deionized water and ethanol. Polyvinyl pyrrolidone (PVP) were added to the solution as a surfactant and a stoichiometric amount of glycine was added as a complexing agent and the fuel for subsequent self-combustion. 5 μL of the stock solution was deposited on the as-prepared LSCF surface or a porous cathode. After overnight drying in ambient air, the resulting coating was fi red at 900 ° C in air for 1 hour. [179]

The modified and blank LSCF porous electrode were tested with a Crofer 22 APU foil as interconnect. All cells were tested at 750°C, with 3% H_2O and 1% CO_2 fed along with air to the cathode. Shown in Figure 82 is cathodic overpotential of the blank LSCF and the catalyst infiltrated LSCF cathode as functions of testing time under conditions prone to cause Cr poisoning. The LSCF electrodes infiltrated with LCNF and LCF exhibits mitigated effect towards Cr poisoning.

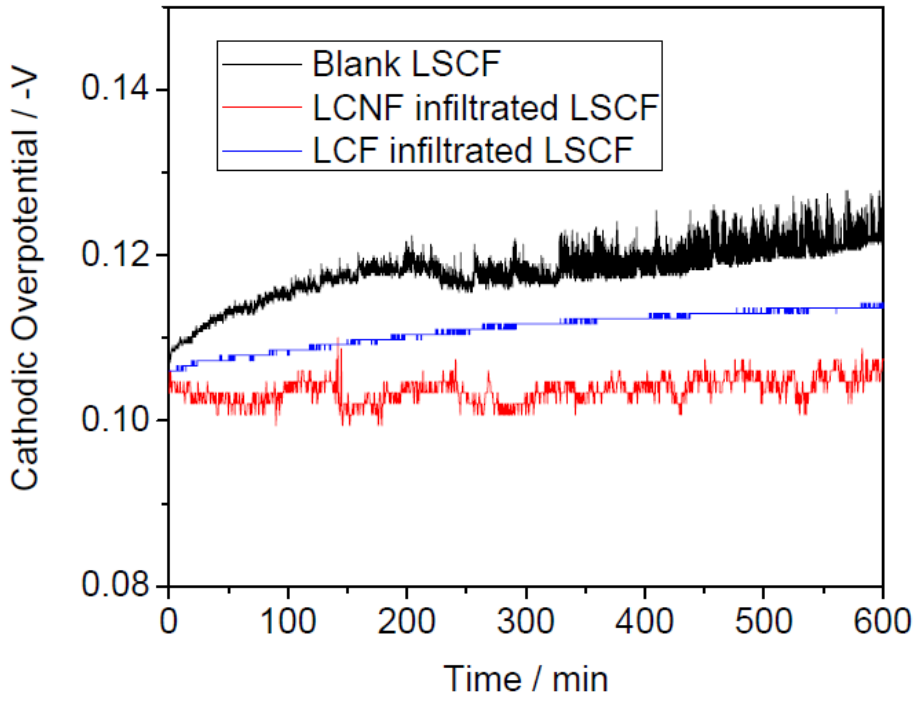

Figure 82: Electrochemical performance evaluation of Cr poisoning resistance through surface modification. Time dependence of cathodic overpotential of the blank LSCF and catalyst infiltrated LSCF cathodes contact with Cr-alloy at 750oC at a constant voltage of 0.25 V when air containing 3% H2O and 1% CO2 was fed to the cathode. (Courtsey of Dong Ding)

The mitigation of Cr poisoning by surface modifications was investigated with SERS. Displayed in Figure 83 are the averaged SERS spectra collected from porous LSCF with and without surface modifications after the accelerated Cr poisoning tests. All samples display

characteristic Raman features associated with $SrCrO_4$ (857 cm^{-1}) and Cr_2O_3 (350 cm^{-1}). The intensities of the $SrCrO_4$ bands decrease in the order of Blank > LCF > LCNF, suggesting less $SrCrO_4$ formation on the modified LSCF porous electrode surfaces. While the quantitative order of $SrCrO_4$ concentration is consistent with the electrochemical testing results that modified LSCF suffered less from Cr poisoning, the correlation is not conclusive.

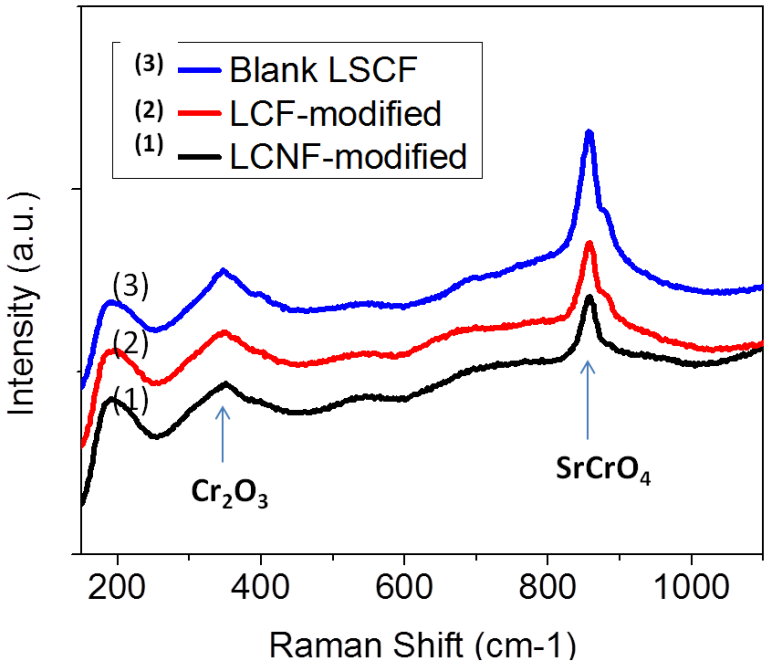

Figure 83: SERS analysis of Cr deposition on LSCF porous electrodes with and without modification. Spectra collected from the top surface of working electrodes (Blank LSCF, LCF Modified LSCF and LCNF modified LSCF) of the symmetric cell. Each spectrum is an average of the spectra collected from 27 random points on each electrode surface.

In order to gain more insight into the distribution Cr poisoning on different electrode surfaces, the $SrCrO_4$ peak intensities of all spectra were studied statistically. Given the large number (27) of spectra collected from each sample, the statistical analysis on the spectral features may provide information on the distribution of Cr poisoning species on the porous

electrodes. Figure 84(A) shows the cumulative percentage of sampled points plotted with respect to the $SrCrO_4$ peak intensities. Compared with the blank LSCF electrode, the LCNF and LCF modified electrodes showed higher percentage of sampled points with lower $SrCrO_4$ intensities. If the sampled points with less than 200 counts in SrCrO4 peak intensity are deemed "Cr Free", the percentage of the estimated "Cr Free" regions on the modified samples is about 5 times more than that on the blank LSCF electrode, as shown in Figure 84(B).

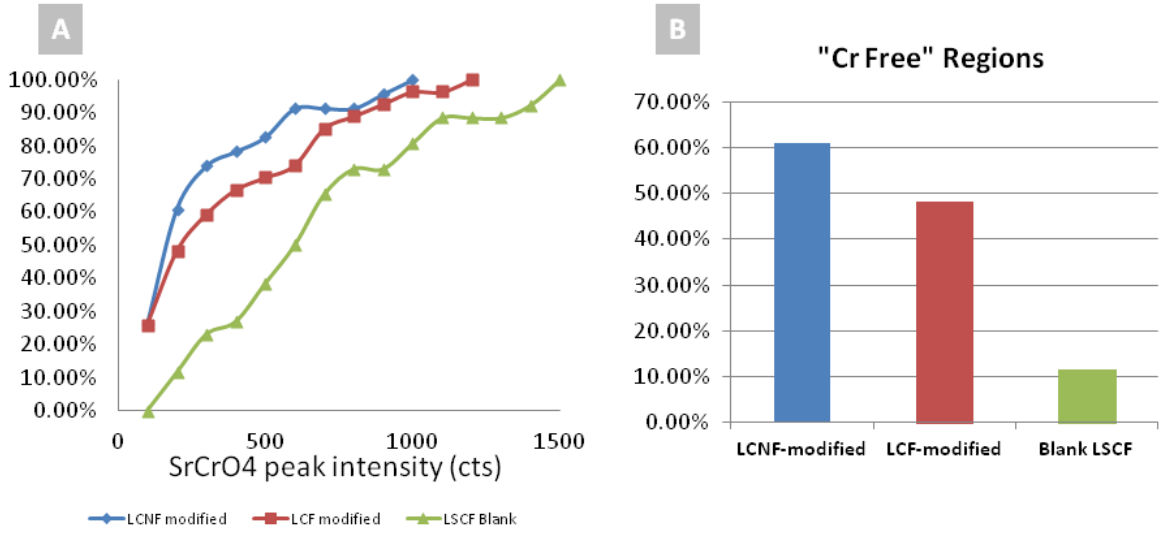

Figure 84: Statistical analysis of coverage of Cr related species on LSCF porous electrode with and without modifications.
(A) The cumulative percentage of sampled points as a function of SrCrO4 band ($857 cm^{-1}$) intensity. (B) The percentage of "Cr Free" regions where less than 200 counts were detected around the SrCrO4 peak.

Since SERS is a surface specific technique, any trace amount of Cr deposition will register high intensity of $SrCrO_4$ peaks in the Raman spectrum. Therefore, the analysis of the statistics of $SrCrO_4$ peak distribution could help determine the coverage of Cr poisoning species. From the statistical analysis, the LCNF and LCF modified LSCF porous electrodes were found to resist Cr deposition on a large portion of the surface. The existence of $SrCrO_4$ on certain

regions on the modified samples could be attributed to the non-uniform distribution of the LCNF and LCF coating, which could be improved through optimization in future studies.

8.4. Chapter Conclusions

The degradation of LSCF cathodes over long term operation are investigated through surface enhanced Raman spectroscopy (SERS). The capability to detect species present in trace amount, in virtue of the high sensitivity of SERS technique, facilitates the surface mapping and statistical analysis. The LSCF pellets annealed for 250 hrs all showed indirect evidence of SrO segregation. In particular, the presence of water seems to exacerbate this process, and promoted its reaction with CO_2 to form $SrCO_3$. Cr containing vapor easily contaminate the LSCF surface to form $SrCrO_4$, especially in the water steam containing atmosphere. Detailed analysis showed that the amount of Cr deposition increases as the concentration of water steam rises, and changes the surface morphology. Even in the situation that a direct Cr source is absent, Cr poisoning could occur due to the presence of minor Cr sources in the testing fixture. Species mapping with the assistance of SERS suggests that the GDC-LSCF interfaces are the hot spots for the formation of $SrCrO_4$. While the surface modification catalysts, e.g., LCF and LCNF, cannot fully prevent the development of $SrCrO_4$, they created regions that are largely Cr free, and thus resisted the degradation process.

CHAPTER 9: **CONCLUDING REMARKS**

9.1. Key Factors of Degradation and Activation of SOFC Electrode Materials

This thesis study focuses on probing the surface of solid oxide fuel cell electrodes, to gain insight into the reaction processes related to electrode functioning and degradation. The main advancements in mechanistic understanding can be summarized as follows:

Carbon deposition on the nickel-based anode initiates rapidly upon a small amount of propane exposure (~20mL) at 450^0C. Continuous exposure to propane increases the amount of carbon deposition steadily. The early stage carbon deposition can only be detected by SERS, but after 1000mL of propane exposure, the carbon grows on the nickel surface catastrophically and became significant under ordinary Raman spectroscopy.

Early stage carbon deposition can be effectively prevented by modification catalysts including CeO_2, GDC and BaO. When propane exposure is not too severe, the BaO modification prevented the formation of heavy patch of carbon, alleviating the coking degradation. While a uniform GDC coating could prevent carbon nucleation in the initial round of propane exposure, redox cycling of the nickel surface could breach such protection.

In situ Raman and SERS analysis show different carbon removal pathways between BaO and Ba-containing perovskites (BZY, BZCYYb). Water strongly adsorbs on BaO surface, forming a layer of $Ba(OH)_2$ that provides superior coking resistance, but BaO powders turns into $BaCO_3$ irreversibly in the presence of CO_2. The Ba-containing perovskites, on the other hand, have –OH groups that can be regenerated after propane exposure. In addition, a clear CO_2 driven carbon removal is also observed on the surface of BZCYYb.

Nickel-based anode is susceptible to sulfur poisoning, due to the adsorption of elemental sulfur on nickel surface. While the amount of sulfur adsorption is extremely small, the nickel foil quenched from operating temperatures developed trace amount of contamination phases of NiS_x and S_2, which are detectable by SERS. To prevent the sulfur poisoning on nickel-based anode, the surface modification of GDC and BZCYYb are found effective. The patterned electrode experiments also showed that the TPBs of Ni-BZCYYb yield stable performance in the presence of H_2S, suggesting that the nature of TPB is key to sulfur tolerance.

The oxygen reduction reactions on LSCF and LSM are studied by model cells with patterned microelectrodes with systematically varied sizes, and the dominant paths of ORR are revealed. The polarization resistance of LSCF micro electrodes can be accelerated through surface modification with GDC. The thin coating of GDC is present in the form of nanoparticles, providing extra spots for oxygen adsorption and hence reduced the polarization resistance of LSCF electrodes.

On the LSCF cathode surface, degradation occurs after long term operation. The presence of water seems to exacerbate the SrO segregation, and thus promotes the reaction with CO_2 to form $SrCO_3$, and the reaction with Cr containing vapors to form $SrCrO_4$. The detection of degradation species on LSCF relies critically on the SERS technique, which enhances the detection sensitivity towards Cr-related phases present in trace amount, and allows for surface mapping and statistical analysis.

In summary, the electrode functionality and degradation in the SOFC systems are often governed by the interaction between electrode materials, surface catalysts, operation atmospheres, and electrical biases. Careful tuning of material composition and microstructure of the

heterogeneous interfaces can enhance the synergy between different factors and thus improve the performance and stability of SOFCs.

The characterization methods developed in this study is essential in probing electrode surface species and incipient phases for mechanistic understanding. In particular, SERS enabled detection of chemical species present in trace amount; in situ and operando analysis revealed material properties under conditions close to SOFC operations; EFM probes the distribution of contamination species under nanometer scale; patterned electrodes with well defined geometries and interfaces makes possible of isolation of contributions from intrinsic surface and interface processes. These methods can also be deployed to the mechanistic studies of a wide variety of catalysts and electrochemical interfaces.

9.2. Limitations of the Characterization Methods

While the novel characterization methods presented in this thesis provided insights into SOFC electrode performance, further work is needed to improve the reliability of these analytical techniques for analysis of the SOFC electrodes.

9.2.1. Raman spectroscopy and SERS

Fluorescence is a perennial challenge for Raman spectroscopy. Since fluorescence process has higher cross-section than Raman scattering, the background interference it brings forth often eclipses the Raman spectral features of interest. It also impacts SERS analysis, since the LSPR of Ag nanoparticles also enhances the fluorescence process.

Several strategies can mitigate the influence of fluorescence background. The first strategy relies on the ps time-resolved spectrometer for fluorescence rejection. Raman scattering is a coherent process: the scattered photon is generated immediately when the probed molecule interacts with the excitation photon. In contrast, fluorescence is an incoherent process that involves the adsorption of excitation photon, relaxation of the excited molecule and the emission of fluorescent photon.[180] While Raman scattering occurs within 1ps upon excitation, fluorescence was generated in the time scale of ns, and therefore these two processes can be separated temporally with a pulsed excitation source and a picosecond gated detector. [181, 182]

Another strategy for reducing fluorescence is based on the fact that energy of Raman scattered photon is fixed to the energy of incident excitation photon, and that of the fluorescent photon is tied to the energy gap of the electronic excitation of the probed molecules. When the energy of the excitation laser changes, the wavenumbers shift of Raman bands do not change, although the intensities of bands may vary due to the resonance effect. Thus using excitation in the range where no absorption takes place usually eliminates fluorescence. Based on this principle, researchers also developed Shifted Excitation Raman Difference Spectroscopy (SERDS), which extracted the Raman bands by comparing the spectra collected with different excitation sources. [183, 184]

While the above two strategies requires significant modification of the spectrometer, post-processing of the spectra can also be used for fluorescence rejection.[144, 185] Since fluorescence band is usually broader than Raman spectrum, polynomial background fitting often provide a sufficient background cleaning. This thesis adopted the polynomial background fitting for the extraction of Raman spectral features. Unfortunately, some irregular fluorescence features cannot be removed and obscured the Raman features of interest.

Another limitation of Raman spectroscopy is the assignment of spectral features for unknown species. Since the vibration bands of the material surfaces cannot be precisely predicted, the assignment of spectral feature to certain phases is empirical in general. In addition, the existing database for Raman spectra is not as comprehensive as that of XRD. As a result, many peak assignments need to be done through comparison against the literature figures. To make the assignment of functional groups even more challenging, for the same functional group, the vibration band energy varies when the molecular bonding condition changes. Therefore, the clear identification of material surface phases and intermediate species during the catalytic reactions such as hydrocarbon reforming can be overwhelmingly complicated.

Surface enhanced Raman spectroscopy (SERS) experiments can generate artifacts if the SERS probes are not properly treated prior to the analysis. For example, the as deposited $Ag@SiO_2$ nanoparticles manifest contamination signals of the organic dispersant (e.g., PVP) used in the fabrication process. To minimize the organic residue, the core-shell nanoparticles need to be cleaned twice by centrifuging in ethanol. In addition, high temperature treatment is also necessary prior to the SERS experiment to decompose or evaporate the organic species. In addition, while the SiO_2 shell is inert to most catalytic reactions, the presence of SERS probe could change the performance of the model fuel cells, since the nanoprobes physically block some area from the access to reacting species. Therefore, the electrochemical testing results conducted in the presence of SERS probes may deviate from its original condition.

9.2.2. Electrostatic Force Microscopy

The EFM detects the contact potential difference between the AFM tip and the probed sample surface. However, the CPD is not the only component contributing to the magnitude of electrostatic forces. The morphology of the substrate also influence the EFM signal: the tip-

substrate interaction is stronger on concave surface while weaker on the convex surface. Therefore, to distinguish a surface phase from another, the EFM image at one bias level is not enough, and a complementary image taken at a bias level with opposite sign is necessary.

If different phases have similar surface potentials, however, EFM will have difficulty distinguishing them, since they will report the same CPD with the AFM tip. The difference of surface potential finds its origin in the material work function. However, the surface adsorbed dipoles, such as hydroxyl groups, could rearrange and flatten the surface potential difference. Therefore, the application of EFM on the detection of surface phases are limited to the situations in which the phase of interest and substrate have sufficient difference in surface potential and generate an unambiguous contrast in the EFM images.

9.2.3. Patterned Electrodes

In this thesis, three methods were utilized to create patterned electrodes and surface modifications, each having limitations.

The embedded mesh method has the advantage of creating a electrically connected network underneath the electrode surface, facilitate the current collection. This method, however, can only be used for limited types of materials of which the meshes are available. In addition, the mismatch of the thermal expansion coefficient between the metal meshes and ceramic substrates could develop cracks on the interface. Fortunately, for each strand of the metal mesh, the crack usually develops on only one side, and can be clearly seen under optical microscope and avoided. In addition, due to the uncontrollable polishing procedure that reveals the metal-electrolyte interface, the electrochemical performances of the mesh electrodes have poor reproducibility.

The sputtered patterned electrodes, in combination with the micro-probe EIS system, make possible of the mechanistic study based on the variation of electrode geometry. However, the atmosphere control of the micro-probe EIS study is challenging. Therefore, only cathode materials can be studied under the current system, since it does not require an enclosure for atmosphere control. Another potential source of artifact comes from the sheet resistance of the patterned electrode. Since the current collection on the patterned electrode is performed with a tungsten carbide tip at the center of each electrode pad, the edge of the electrode maybe inactive due to the limited electronic conductivity. A detailed analysis of the influence of sheet resistance on the polarization resistance of thin film electrodes has been reported elsewhere. [186]

Metal films of anode materials can be fabricated with photo-lithography method on the polished electrolyte surface. Unlike the patterns for micro-probe EIS study, the patterns are connected to each other, to make possible of current collection so it can be tested with a standard alumina tube with proper sealant. However, the metal patterned electrodes usually have wetting problem with the electrolyte substrates. When the film is too thin, the dewetting process can cause morphological change of the metal electrode; if the film gets too thick, however, the internal stress in the metal film may cause overall delaminating of the film. The common methods to enhance the adhesion, e.g., using Ti or Cr buffer layer, causes changes in electrochemical property and are therefore not suitable for the mechanistic study.

The block co-polymer method of catalyst patterning offers a unique alternative to create heterogeneous interfaces on nanometer scale. However, the stability of the nanoscale features after high temperature treatment may not be sufficient, causing agglomeration of the nanoparticles. In order to preserve the delicate features on the electrode surface, the heat treatment procedure needs to be restricted under certain temperatures.

9.3. Future Works

9.3.1. Combinatorial Study of Interfaces

Operando SERS has shown great promise in identifying critical surface species and intermediates related to the hydrocarbon reforming and carbon deposition on nickel surface. With the high surface sensitivity provided by SERS, time-resolved analysis can be performed on the surface electrochemical processes. The patterned electrode and catalyst patterning techniques could create multiple interfaces of interest on a single sample, facilitating the monitoring of reaction hot spots. As shown in Figure 85, 10 different electrochemical functional regions can be monitored on a model cell with patterned electrodes, defined by the substrates (electrode, electrolyte, TPB), the surface modification (modified and bare region), and the electrochemical connectivity (with and without bias). The spatial resolution provided by confocal Raman spectroscopy system makes possible of mapping critical species across interfaces, providing additional information of the electrochemical processes.

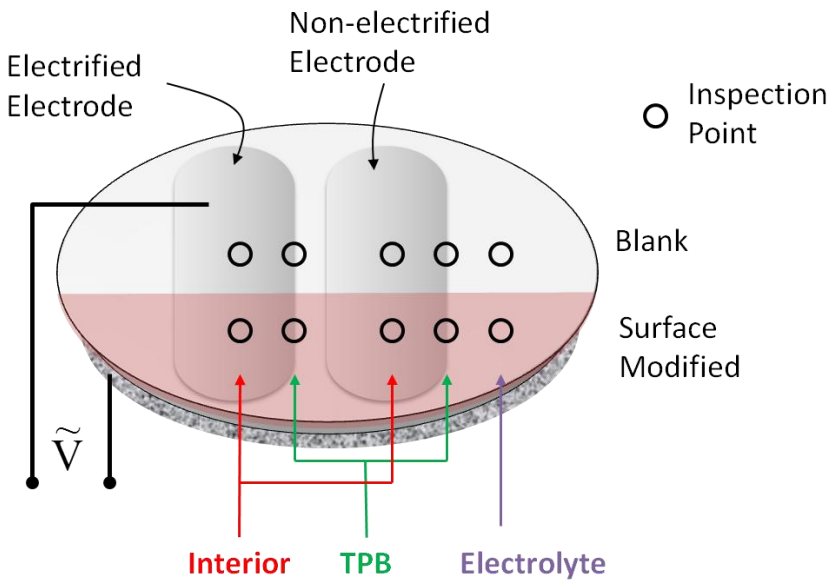

Figure 85: Critical surface and interface regions for *operando* study of electrode behavior.

9.3.2. *In situ* SERS with Embedded Probe Architecture

The SERS experiments conducted in this thesis, either *ex situ* or *in situ*, are based on the configuration of "external probes". The architecture of "embedded probes", in comparison, could provide higher enhancement factor, because the catalyst materials form uniform coatings on the surface of Ag nanoparticles, so more surface intermediate species are within the region of enhanced LSPR field. For example, the YSZ coated Ag nanoparticles can be used to study the oxygen reduction reaction on YSZ surfaces, and in addition, the loading of small amount of LSM or LSCF particles on the Ag@YSZ probes, can provide SERS for the study of ORR on the cathode-YSZ interfaces. Similar architecture can be used for the study of hydrocarbon reforming processes on the Ni-catalyst interfaces. By coating the Ag nanoparticle with Ni, followed by the deposition of nanosized catalysts such as doped ceria, the heterogeneous interface between nickel and CeO_2 can be probed. The embedded SERS probes can also be used to monitor the

chemical reactions during the material fabrication processes. Atomic layer deposition is an effective method to develop embedded probes, as demonstrated by Tian group and van Duyne group, who created thin film coatings of a variety of metals and ceramics on Ag nanoprobes. However, it is challenging to coat the Ag surface uniformly with other materials of interest, e.g., YSZ, GDC or BZCYYb, since the precursors of these metal oxides for ALD process are not all developed.

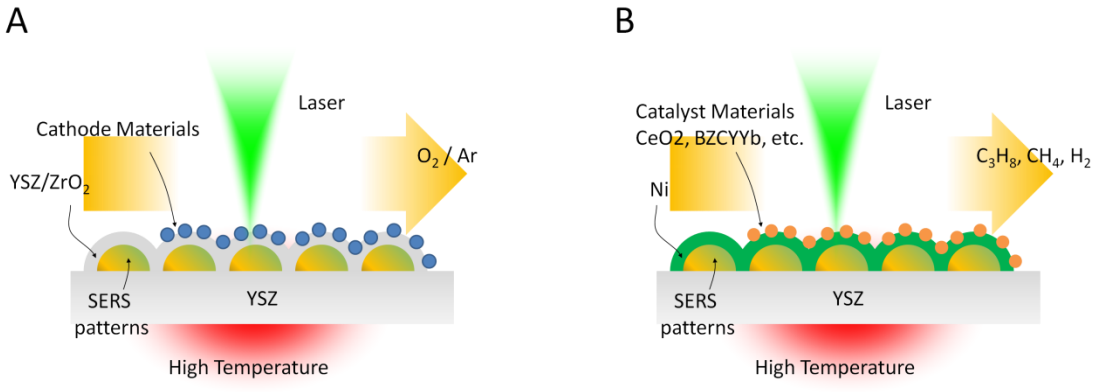

Figure 86: *In Situ* Raman spectroscopy based on "embedded probe" architecture.
(A) For the study of cathode-electrolyte interface. (B) For the study of catalyst-Ni interface.

REFERENCES

1. I. E. Agency, O. f. E. Co-operation and Development, *Resources to Reserves 2013: Oil, Gas and Coal Technologies for the Energy Markets of the Future*, OECD, 2013.
2. U. S. E. I. Administration, 2013.
3. T. Stocker, L. Alexander, M. Allen and I. P. o. C. C. W. G. I., *Climate Change 2013: The Physical Science Basis : Final Draft Underlying Scientific-technical Assessment : Working Group I Contribution to the IPCC Fifth Assessment Report*, WMO, IPCC Secretariat, 2013.
4. S. M. Haile, *Acta Materialia*, 2003, **51**, 5981-6000.
5. S. C. Singhal, *Solid State Ionics*, 2000, **135**, 305-313.
6. L. Yang, Y. Choi, W. Qin, H. Chen, K. Blinn, M. Liu, P. Liu, J. Bai, T. A. Tyson and M. Liu, *Nat Commun*, 2011, **2**, 357.
7. E. P. Murray, T. Tsai and S. A. Barnett, *Nature*, 1999, **400**, 649.
8. Z. L. Zhan and S. A. Barnett, *Solid State Ionics*, 2005, **176**, 871-879.
9. S. W. Zha, A. Moore, H. Abernathy and M. L. Liu, *J. Electrochem. Soc.*, 2004, **151**, A1128-A1133.
10. M. Liu, R. Peng, D. Dong, J. Gao, X. Liu and G. Meng, *J. Power Sources*, 2008, **185**, 188-192.
11. E. P. Murray, S. J. Harris, J. Liu and S. A. Barnett, *Electrochemical and Solid State Letters*, 2006, **9**, A292-A294.
12. M. F. Liu, Y. M. Choi, L. Yang, K. Blinn, W. T. Qin, P. Liu and M. L. Liu, *Nano Energy*, 2012, **1**, 448-455.
13. M. C. Williams, J. P. Strakey and W. A. Surdoval, *J. Power Sources*, 2005, **143**, 191-196.
14. C. Descamps, C. Bouallou and M. Kanniche, *Energy*, 2008, **33**, 874-881.
15. K. Ikeda, N. Hisatome, K. Nagata, D. Tsukamoto, Y. Kawaguchi, K. Kosaka, N. Matake, H. Sasatsu, Y. Takahashi and K. Konishi, *Ecs Transactions*, 2007, **7**, 39-43.
16. M. Day, S. L. Swartz and G. Arkenberg, *Ecs Transactions*, 2011, **35**, 385-391.
17. M. Badding, W. Bouton, J. Brown, L. Kester, C. W. Tanner and P. Tepesch, *Meeting Abstracts*, 2011, **MA2011-01**, 832.
18. ARPA-E, Department of Energy, Seattle, 2009.
19. J. Rifkin, *The Third Industrial Revolution: How Lateral Power Is Transforming Energy, the Economy, and the World*, Palgrave Macmillan, 2011.
20. B. C. H. Steele, *Solid State Ionics*, 2000, **134**, 3-20.
21. M. Krumpelt, T. R. Krause, J. D. Carter, J. P. Kopasz and S. Ahmed, *Catalysis Today*, 2002, **77**, 3-16.
22. S. Zha, A. Moore, H. Abernathy and M. Liu, *J. Electrochem. Soc.*, 2004, **151**, A1128-A1133.
23. A. Atkinson, S. Barnett, R. J. Gorte, J. T. S. Irvine, A. J. McEvoy, M. Mogensen, S. C. Singhal and J. Vohs, *Nature Materials*, 2004, **3**, 17.
24. Y. B. Lin, Z. L. Zhan, J. Liu and S. A. Barnett, *Solid State Ionics*, 2005, **176**, 1827-1835.
25. E. R. Ray, N. J. Maskalick and C. J. Spengler, *Contaminant effects in solid oxide fuel cells*, Westinghouse Sci. Technol. Cent.,Pittsburgh,PA,USA., 1991.
26. S. Zha, Z. Cheng and M. Liu, *J. Electrochem. Soc.*, 2007, **154**, B201-B206.
27. J.-H. Wang and M. Liu, *Electrochem. Commun.*, 2007, **9**, 2212-2217.
28. S. P. S. Badwal, R. Deller, K. Foger, Y. Ramprakash and J. P. Zhang, *Solid State Ionics*, 1997, **99**, 297-310.
29. S. P. Jiang, J. P. Zhang and X. G. Zheng, *Journal of the European Ceramic Society*, 2002, **22**, 361-373.
30. H. Kurokawa, K. Kawamura and T. Maruyama, *Solid State Ionics*, 2004, **168**, 13-21.

31. M. Finsterbusch, A. Lussier, J. A. Schaefer and Y. U. Idzerda, *Solid State Ionics*, 2012, **212**, 77-80.
32. W. A. Harrison, *Physical Review B*, 2011, **83**.
33. C. Xia, B. Rauch, J. Cochran, J. Lee and M. Liu, Recent Advances in Design and Fabrication of Low-Temperature SOFCs, Singapore, 2002.
34. C. Xia, W. Rauch, F. Chen and M. Liu, *Solid State Ionics*, 2002, **149**, 11-19.
35. Z. P. Shao and S. M. Haile, *Nature*, 2004, **431**, 170-173.
36. H. Kim, C. Lu, W. L. Worrell, J. M. Vohs and R. J. Gorte, *J. Electrochem. Soc.*, 2002, **149**, A247-A250.
37. S. W. Tao and J. T. S. Irvine, *Nature Materials*, 2003, **2**, 320-323.
38. Y. H. Huang, R. I. Dass, Z. L. Xing and J. B. Goodenough, *Science*, 2006, **312**, 254-257.
39. Z. Liu, L.-z. Cheng and M.-F. Han, *J. Power Sources*, 2011, **196**, 868-871.
40. S. B. Adler, *Chemical Reviews*, 2004, **104**, 4791-4843.
41. M. L. Yang, Y. A. Zhu, C. Fan, Z. J. Sui, D. Chen and X. G. Zhou, *Phys Chem Chem Phys*, 2011, **13**, 3257-3267.
42. H. Y. Liu, R. X. Yan, R. G. Zhang, B. J. Wang and K. C. Xie, *Journal of Natural Gas Chemistry*, 2011, **20**, 611-617.
43. D. L. Trimm, *Catalysis Today*, 1997, **37**, 233-238.
44. R. J. Gorte, J. M. Vohs and S. McIntosh, Recent developments on anodes for direct fuel utilization in SOFC, Monterey, CA., United States, 2004.
45. Z. Cheng, J.-H. Wang, Y. Choi, L. Yang, M. C. Lin and M. Liu, *Energy & Environmental Science*.
46. Z. Cheng and M. Liu, *Solid State Ionics*, 2007, **178**, 925-935.
47. Z. Cheng, H. Abernathy and M. L. Liu, *Journal of Physical Chemistry C*, 2007, **111**, 17997-18000.
48. L. F. Nie, M. F. Liu, Y. J. Zhang and M. L. Liu, *J. Power Sources*, 2010, **195**, 4704-4708.
49. X. Y. Lou, S. Z. Wang, Z. Liu, L. Yang and M. L. Liu, *Solid State Ionics*, 2009, **180**, 1285-1289.
50. M. E. Lynch, L. Yang, W. Qin, J.-J. Choi, M. Liu, K. Blinn and M. Liu, *Energy & Environmental Science*, **4**, 2249-2258.
51. J. H. Guo, C. Xie, K. T. Lee, N. Guo, J. T. Miller, M. J. Janik and C. S. Song, *Acs Catalysis*, 2011, **1**, 574-582.
52. L. Yang, S. Wang, K. Blinn, M. Liu, Z. Liu, Z. Cheng and M. Liu, *Science*, 2009, **326**, 126-129.
53. S. P. Jiang, *Journal of Solid State Electrochemistry*, 2006, **11**, 93-102.
54. S. P. Jiang, *J. Power Sources*, 2003, **124**, 390-402.
55. F. Tietz, V. A. C. Haanappel, A. Mai, J. Mertens and D. Stover, *J. Power Sources*, 2006, **156**, 20-22.
56. M. E. Lynch, D. Ding, W. M. Harris, J. J. Lombardo, G. J. Nelson, W. K. S. Chiu and M. L. Liu, *Nano Energy*, 2013, **2**, 105-115.
57. J. Janek, B. Luerssen, E. Mutoro, H. Fischer and S. Gunther, *Topics in Catalysis*, 2007, **44**, 399-407.
58. K. Nakamoto, *Infrared and Raman Spectra of Inorganic and Coordination Compounds Part A: Theory and Applications in Inorganic Chemistry*, John Wiley & Sons, Inc., New York, 1997.
59. V. G. Keramidas and W. B. White, *The Journal of Chemical Physics*, 1973, **59**, 1561-1562.
60. J. R. McBride, K. C. Hass, B. D. Poindexter and W. H. Weber, *Journal of Applied Physics*, 1994, **76**, 2435.
61. K. Ahn, D. S. Yoo, D. H. Prasad, H.-W. Lee, Y.-C. Chung and J.-H. Lee, *Chemistry of Materials*, 2012, **24**, 4261-4267.
62. C. Peng, Y. Wang, K. Jiang, B. Q. Bin, H. W. Liang, J. Feng and J. Meng, *J Alloy Compd*, 2003, **349**, 273-278.
63. W. Y. Hernandez, M. A. Centeno, F. Romero-Sarria and J. A. Odriozola, *Journal of Physical Chemistry C*, 2009, **113**, 5629-5635.

64. A. Mineshige, T. Taji, Y. Muroi, M. Kobune, S. Fujii, N. Nishi, M. Inaba and Z. Ogumi, *Solid State Ionics*, 2000, **135**, 481-485.
65. Y. M. Choi, H. Abernathy, H. T. Chen, M. C. Lin and M. Liu, *Chemphyschem*, 2006, **7**, 1957-1963.
66. H. W. Abernathy, E. Koep, C. Compson, Z. Cheng and M. L. Liu, *Journal of Physical Chemistry C*, 2008, **112**, 13299-13303.
67. K. S. Blinn, H. Abernathy, X. X. Li, M. F. Liu, L. A. Bottomley and M. L. Liu, *Energy & Environmental Science*, 2012, **5**, 7913-7917.
68. Z. Cheng, H. Abernathy and M. Liu, *Journal of Physical Chemistry C*, 2007, **111**, 17997-18000.
69. M. B. Pomfret, J. C. Owrutsky and R. A. Walker, *The journal of physical chemistry. B*, 2006, **110**, 17305-17308.
70. D. L. Jeanmaire and R. P. Van Duyne, *Journal of Electroanalytical Chemistry and Interfacial Electrochemistry*, 1977, **84**, 1-20.
71. M. G. Albrecht and J. A. Creighton, *Journal of the American Chemical Society*, 1977, **99**, 5215-5217.
72. N. E. Marotta, J. R. Barber, P. R. Dluhy and L. A. Bottomley, *Appl Spectrosc*, 2009, **63**, 1101-1106.
73. J. M. McLellan, A. Siekkinen, J. Y. Chen and Y. N. Xia, *Chemical Physics Letters*, 2006, **427**, 122-126.
74. L. Baia, M. Baia, J. Popp and S. Astilean, *The Journal of Physical Chemistry B*, 2006, **110**, 23982-23986.
75. D. Mortazavi, A. Z. Kouzani, A. Kaynak and W. Duan, *Progress in Electromagnetics Research-Pier*, 2012, **126**, 203-235.
76. K. A. Willets and R. P. Van Duyne, *Annu Rev Phys Chem*, 2007, **58**, 267-297.
77. M. Kerker, D.-S. Wang and H. Chew, *Appl. Opt.*, 1980, **19**, 4159-4174.
78. P. L. Stiles, J. A. Dieringer, N. C. Shah and R. R. Van Duyne, in *Annual Review of Analytical Chemistry*, 2008, vol. 1, pp. 601-626.
79. J. Zhao, J. A. Dieringer, X. Zhang, G. C. Schatz and R. P. Van Duyne, *Journal of Physical Chemistry C*, 2008, **112**, 19302-19310.
80. K. A. Willets and R. P. Van Duyne, in *Annu. Rev. Phys. Chem.*, 2007, vol. 58, pp. 267-297.
81. M. Moskovits, *Reviews of Modern Physics*, 1985, **57**, 783-826.
82. Z. Q. Tian, B. Ren, J. F. Li and Z. L. Yang, *Chem. Commun.*, 2007, 3514-3534.
83. J. Lee, S. Shim, B. Kim and H. S. Shin, *Chemistry-a European Journal*, **17**, 2381-2387.
84. F. Schedin, E. Lidorikis, A. Lombardo, V. G. Kravets, A. K. Geim, A. N. Grigorenko, K. S. Novoselov and A. C. Ferrari, *Acs Nano*, **4**, 5617-5626.
85. K. L. A. Chan and S. G. Kazarian, *Nanotechnology*, **22**, 5.
86. K. S. Blinn, H. W. Abernathy and M. Liu, in *Advances in Solid Oxide Fuel Cells V*, ed. N. P. S. P. Bansal, vol. 30, pp. 65-73.
87. X. Li, K. Blinn, Y. Fang, M. Liu, M. A. Mahmoud, S. Cheng, L. A. Bottomley, M. El-Sayed and M. Liu, *Physical Chemistry Chemical Physics*, 2012, **14**, 5919-5923.
88. K. R. Beavers, N. E. Marotta and L. A. Bottomley, *Chemistry of Materials*, 2010, **22**, 2184-2189.
89. A. V. Whitney, J. W. Elam, P. C. Stair and R. P. Van Duyne, *Journal of Physical Chemistry C*, 2007, **111**, 16827-16832.
90. J. F. Li, Y. F. Huang, Y. Ding, Z. L. Yang, S. B. Li, X. S. Zhou, F. R. Fan, W. Zhang, Z. Y. Zhou, Y. Wu de, B. Ren, Z. L. Wang and Z. Q. Tian, *Nature*, 2010, **464**, 392-395.
91. E. C. Le Ru, E. Blackie, M. Meyer and P. G. Etchegoin, *Journal of Physical Chemistry C*, 2007, **111**, 13794-13803.
92. R. P. Van Duyne, J. C. Hulteen and D. A. Treichel, *The Journal of Chemical Physics*, 1993, **99**, 2101-2115.
93. J. Nowotny, T. Bak and C. C. Sorrell, *Advances in Applied Ceramics*, 2005, **104**, 181-187.
94. S. Ladas, S. Bebelis and C. G. Vayenas, *Surface Science*, 1991, **251**, 1062-1068.

95. J. Lu, E. Delamarche, L. Eng, R. Bennewitz, E. Meyer and H. J. Guntherodt, *Langmuir*, 1999, **15**, 8184-8188.
96. S. V. Kalinin and D. A. Bonnell, *Physical Review B*, 2004, **70**.
97. W. H. J. Rensen, N. F. van Hulst, A. G. T. Ruiter and P. E. West, *Applied Physics Letters*, 1999, **75**, 1640-1642.
98. F. J. Giessibl, *Physical Review B*, 1997, **56**, 16010-16015.
99. L. Gross, F. Mohn, P. Liljeroth, J. Repp, F. J. Giessibl and G. Meyer, *Science*, 2009, **324**, 1428-1431.
100. X. Li, K. Blinn, Y. Fang, M. Liu, M. A. Mahmoud, S. Cheng, L. A. Bottomley, M. El-Sayed and M. Liu, *Physical Chemistry Chemical Physics*, **14**, 5919-5923.
101. R. M. Stockle, V. Deckert, C. Fokas and R. Zenobi, *Appl. Spectrosc.*, 2000, **54**, 1577-1583.
102. J. Park, J. Joo, S. G. Kwon, Y. Jang and T. Hyeon, *Angewandte Chemie-International Edition*, 2007, **46**, 4630-4660.
103. K. Dongjo, J. Sunho and M. Jooho, *Nanotechnology*, 2006, **17**, 4019.
104. K. S. Blinn, X. Li, M. Liu, L. A. Bottomley and M. Liu, *Journal of visualized experiments : JoVE*, 2012, e50161-e50161.
105. M. Nakamura, H. Yamada and S. Morita, Springer Berlin Heidelberg, 2007, pp. 43-51.
106. P. Girard, *Nanotechnology*, 2001, **12**, 485-490.
107. H. B. Michaelson, *Journal of Applied Physics*, 1977, **48**, 4729-4733.
108. A. N. Nazarov, S. O. Gordienko, P. M. Lytvyn, V. V. Strelchuk, A. S. Nikolenko, A. V. Vasin, A. V. Rusavsky, V. S. Lysenko and V. P. Popov, *physica status solidi (c)*, 2013, **10**, 1172-1175.
109. J. Fleig, F. S. Baumann, V. Brichzin, H. R. Kim, J. Jamnik, G. Cristiani, H. U. Habermeier and J. Maier, *Fuel Cells*, 2006, **6**, 284-292.
110. E. Koep, Ph.D. Dissertation, Georgia Institute of Technology, 2006.
111. J.-W. Lee, Z. Liu, L. Yang, H. Abernathy, S.-H. Choi, H.-E. Kim and M. Liu, *J. Power Sources*, 2009, **190**, 307-310.
112. E. Koep, D. S. Mebane, R. Das, C. Compson and M. L. Liu, *Electrochemical and Solid State Letters*, 2005, **8**, A592-A595.
113. F. S. Baumann, J. Fleig, H. U. Habermeier and J. Maier, *Solid State Ionics*, 2006, **177**, 1071-1081.
114. V. Brichzin, J. Fleig, H. U. Habermeier and J. Maier, *Electrochemical And Solid State Letters*, 2000, **3**, 403-406.
115. X. Li, J.-P. Lee, K. S. Blinn, D. Chen, S. Yoo, B. Kang, L. A. Bottomley, M. A. El-Sayed, S. Park and M. Liu, *Energy & Environmental Science*, 2014, **7**, 306-310.
116. W. H. Weber, K. C. Hass and J. R. McBride, *Physical Review B*, 1993, **48**, 178-185.
117. T. Itoh, K. Abe, K. Dokko, M. Mohamedi, I. Uchida and A. Kasuya, *J. Electrochem. Soc.*, 2004, **151**, A2042-A2046.
118. S.-G. Wang, D.-B. Cao, Y.-W. Li, J. Wang and H. Jiao, *Surface Science*, 2009, **603**, 2600-2606.
119. A. Gazsi, I. Ugrai and F. Solymosi, *Applied Catalysis a-General*, **391**, 360-366.
120. M. Shishkin and T. Ziegler, *Journal of Physical Chemistry C*, 2013, **117**, 7086-7096.
121. M. Shishkin and T. Ziegler, *The Journal of Physical Chemistry C*, 2009, **113**, 21667-21678.
122. D. H. Rank, E. R. Shull and D. W. E. Axford, *Journal of Chemical Physics*, 1950, **18**, 116-117.
123. M. Moskovits and D. P. Dilellla, *Chemical Physics Letters*, 1980, **73**, 500-505.
124. M. R. Fenske, W. G. Braun, R. V. Wiegand, D. Quiggle, R. H. McCormick and D. H. Rank, *Analytical Chemistry*, 1947, **19**, 700-765.
125. K. E. Sterin, V. T. Aleksani˘a˘n and G. N. Zhizhin, *Raman spectra of hydrocarbons*, Pergamon Press, 1980.
126. B. Schrader, *Infrared and Raman Spectroscopy*, Wiley, 2008.
127. L. Pele, J. Sebek, E. O. Potma and R. B. Gerber, *Chemical Physics Letters*, 2011, **515**, 7-12.
128. N. A. Atamas, A. M. Yaremko, T. Seeger, A. Leipertz, A. Bienko, Z. Latajka, H. Ratajczak and A. J. Barnes, *Journal of Molecular Structure*, 2004, **708**, 189-195.

129. D. Chrysostomou, C. French and F. Zaera, *Catalysis Letters*, 2000, **69**, 117-128.
130. C. H. Bartholomew, *Catalysis Reviews*, 1982, **24**, 67-112.
131. W. Y. Lee, J. Hanna and A. F. Ghoniem, *J. Electrochem. Soc.*, 2013, **160**, F94-F105.
132. K. Otsuka, Y. Murakami, Y. J. Wada, A. A. Said and A. Morikawa, *Journal of Catalysis*, 1990, **121**, 122-130.
133. T. V. M. Rao, G. Deo, J. M. Jehng and I. E. Wachs, *Langmuir*, 2004, **20**, 7159-7165.
134. D. L. Trimm, *Catalysis Today*, 1999, **49**, 3-10.
135. A. Siahvashi, D. Chesterfield and A. A. Adesina, *Chemical Engineering Science*, 2013, **93**, 313-325.
136. M. Asamoto, S. Miyake, K. Sugihara and H. Yahiro, *Electrochem. Commun.*, 2009, **11**, 1508-1511.
137. V. M. Gonzalez-Delacruz, F. Ternero, R. Pereniguez, A. Caballero and J. P. Holgado, *Applied Catalysis a-General*, **384**, 1-9.
138. J. J. Guo, H. Lou, L. Y. Mo and X. M. Zheng, *Journal of Molecular Catalysis a-Chemical*, **316**, 1-7.
139. A. V. Bandura, R. A. Evarestov and D. D. Kuruch, *Surface Science*, 2010, **604**, 1591-1597.
140. X. N. Li, Y. Zhang and K. J. Smith, *Applied Catalysis a-General*, 2004, **264**, 81-91.
141. V. R. Choudhary, A. M. Rajput and A. S. Mamman, *Journal of Catalysis*, 1998, **178**, 576-585.
142. K. Sutthiumporn and S. Kawi, *International Journal of Hydrogen Energy*, **36**, 14435-14446.
143. Y. Lykhach, T. Staudt, M. P. A. Lorenz, R. Streber, A. Bayer, H.-P. Steinrueck and J. Libuda, *Chemphyschem*, **11**, 1496-1504.
144. C. A. Lieber and A. Mahadevan-Jansen, *Appl. Spectrosc.*, 2003, **57**, 1363-1367.
145. J. Szanyi, K. Mudiyanselage and C. W. Yi, *Langmuir*, 2009, **25**, 10820-10828.
146. E. C. Corbos, X. Courtois, N. Bion, P. Marecot and D. Duprez, *Applied Catalysis B-Environmental*, 2007, **76**, 357-367.
147. J. J. Lander, *Journal of the American Chemical Society*, 1951, **73**, 5794-5797.
148. Z. Cheng, J. H. Wang, Y. M. Choi, L. Yang, M. C. Lin and M. L. Liu, *Energy & Environmental Science*, 2011, **4**, 4380-4409.
149. E. Brightman, D. G. Ivey, D. J. L. Brett and N. P. Brandon, *J. Power Sources*, 2011, **196**, 7182-7187.
150. M. Y. Gong, X. B. Liu, J. Trembly and C. Johnson, *J. Power Sources*, 2007, **168**, 289-298.
151. P. Lohsoontorn, D. J. L. Brett and N. P. Brandon, *J. Power Sources*, 2008, **175**, 60-67.
152. K. Lee, C. S. Song and M. J. Janik, *Langmuir*, 2012, **28**, 5660-5668.
153. Z. Cheng and M. Liu, *Solid State Ionics*, 2007, **178**, 925-935.
154. S. W. Zha, Z. Cheng and M. L. Liu, *J. Electrochem. Soc.*, 2007, **154**, B201-B206.
155. J. B. Hansen, *Electrochemical and Solid State Letters*, 2008, **11**, B178-B180.
156. X. Li, J.-P. Lee, K. S. Blinn, D. Chen, S. Yoo, B. Kang, L. A. Bottomley, M. A. El-Sayed, S. Park and M. Liu, *Energy & Environmental Science*, 2014.
157. C. Sun, R. Hui and J. Roller, *Journal of Solid State Electrochemistry*, **14**, 1125-1144.
158. M. F. Liu, D. Ding, K. Blinn, X. X. Li, L. F. Nie and M. Liu, *International Journal of Hydrogen Energy*, 2012, **37**, 8613-8620.
159. M. E. Lynch, L. Yang, W. T. Qin, J. J. Choi, M. F. Liu, K. Blinn and M. L. Liu, *Energy & Environmental Science*, 2011, **4**, 2249-2258.
160. D. Ding, M. Liu, Z. Liu, X. Li, K. Blinn, X. Zhu and M. Liu, *Advanced Energy Materials*, 2013, **3**, 1149-1154.
161. M. L. Liu, *J. Electrochem. Soc.*, 1998, **145**, 142-154.
162. C. R. Xia and M. L. Liu, *Advanced Materials*, 2002, **14**, 521-+.
163. Y. Choi, M. C. Lin and M. Liu, *J. Power Sources*, 2010, **195**, 1441-1445.
164. M. Huang and S. Fabris, *Physical Review B*, 2007, **75**, 081404.
165. J. Paier, C. Penschke and J. Sauer, *Chemical Reviews*, 2013, **113**, 3949-3985.

166. P. P. Dholabhai, J. B. Adams, P. Crozier and R. Sharma, *The Journal of Chemical Physics*, 2010, **132**, -.
167. Y. Choi, M. E. Lynch, M. C. Lin and M. Liu, *Journal of Physical Chemistry C*, 2009, **113**, 7290-7297.
168. S. P. Jiang and Y. Zhen, *Solid State Ionics*, 2008, **179**, 1459-1464.
169. S. P. Simner, M. D. Anderson, M. H. Engelhard and J. W. Stevenson, *Electrochemical and Solid State Letters*, 2006, **9**, A478-A481.
170. S. J. Benson, D. Waller and J. A. Kilner, *J. Electrochem. Soc.*, 1999, **146**, 1305-1309.
171. S.-N. Lee, A. Atkinson and J. A. Kilner, *J. Electrochem. Soc.*, 2013, **160**, F629-F635.
172. E. Bucher and W. Sitte, *Solid State Ionics*, 2011, **192**, 480-482.
173. L. W. Tai, M. M. Nasrallah, H. U. Anderson, D. M. Sparlin and S. R. Sehlin, *Solid State Ionics*, 1995, **76**, 273-283.
174. J. F. Mitchell, D. N. Argyriou, C. D. Potter, D. G. Hinks, J. D. Jorgensen and S. D. Bader, *Physical Review B*, 1996, **54**, 6172-6183.
175. L. Martin-Carron, A. de AndrÃ©s, M. J. MartÃnez-Lope, M. T. Casais and J. A. Alonso, *Physical Review B*, 2002, **66**, 174303.
176. L. W. Tai, M. M. Nasrallah, H. U. Anderson, D. M. Sparlin and S. R. Sehlin, *Solid State Ionics*, 1995, **76**, 273-283.
177. B. P. Barbero, J. A. Gamboa and L. E. Cadus, *Applied Catalysis B-Environmental*, 2006, **65**, 21-30.
178. E. Konysheva, H. Penkalla, E. Wessel, J. Mertens, U. Seeling, L. Singheiser and K. Hilpert, *J. Electrochem. Soc.*, 2006, **153**, A765-A773.
179. D. Ding, M. F. Liu, Z. B. Liu, X. X. Li, K. Blinn, X. B. Zhu and M. L. Liu, *Advanced Energy Materials*, 2013, **3**, 1149-1154.
180. D. A. Weitz, S. Garoff, J. I. Gersten and A. Nitzan, *The Journal of Chemical Physics*, 1983, **78**, 5324-5338.
181. N. Everall, T. Hahn, P. Matousek, A. W. Parker and M. Towrie, *Appl. Spectrosc.*, 2001, **55**, 1701-1708.
182. P. Matousek, M. Towrie, C. Ma, W. M. Kwok, D. Phillips, W. T. Toner and A. W. Parker, *Journal of Raman Spectroscopy*, 2001, **32**, 983-988.
183. S. T. McCain, R. M. Willett and D. J. Brady, *Optics Express*, 2008, **16**, 10975-10991.
184. Q. Li, K. R. Wang, S. X. Wang and Ieee, *A New Approach for Fluorescence Subtraction in Raman Spectroscopy*.
185. H. Ruan and L. K. Dai, *Asian Journal of Chemistry*, **23**, 5229-5234.
186. M. E. Lynch and M. Liu, *J. Power Sources*, 2010, **195**, 5155-5166.